

Alma Mater Studiorum - Università di Bologna

DOTTORATO DI RICERCA IN NANOSCIENZE PER
LA MEDICINA E PER L'AMBIENTE

Ciclo 33

Settore Concorsuale: 03/C2 - CHIMICA INDUSTRIALE

Settore Scientifico Disciplinare: CHIM/04 - CHIMICA INDUSTRIALE

OPEN-CELL METALLIC FOAMS FOR THE ELECTROCHEMICAL CONVERSION OF
BIOMASS-DERIVED COMPOUNDS

Presentata da: Giancosimo Sanghez De Luna

Coordinatore Dottorato

Dario Braga

Supervisore

Giuseppe Fornasari

Co-supervisore

Rita Mazzoni

Patricia Benito Martin

Esame finale anno 2021

RINGRAZIAMENTI

Vorrei ringraziare tutte le persone che hanno contribuito a questo lavoro e mi sono state vicine in questi tre anni. Innanzitutto, vorrei ringraziare chi mi ha guidato, supportato e sopportato nel mio lavoro, a cominciare dal Prof. Giuseppe Fornasari, conosciuto già ai tempi della laurea triennale e che mi ha “accompagnato” fino a qui, continuando anche a poche ore dalla consegna con le ultime revisioni di questo lavoro.

Un sentito ringraziamento a Patricia che mi ha guidato sapientemente, fin dall’inizio di questa esperienza, nell’affrontare un argomento totalmente nuovo e complesso come l’elettrocatalisi e l’elettrochimica in generale. Ci sono stati momenti di difficoltà, ma grazie al suo supporto credo che sia stato realizzato un ottimo lavoro di ricerca.

Ovviamente non posso non ringraziare tutto il gruppo del laboratorio “sviluppo processi”, con i Prof. Vaccari, Albonetti, Cavani, il Dott. Tabanelli e tutti i dottorandi e assegnisti che di anno in anno si sono succeduti. Un gruppo fantastico sia dentro che fuori dal laboratorio, ragazzi sempre pronti a dare una mano nei momenti di difficoltà. Ringrazio anche tutti i ragazzi, tesisti triennali e magistrali, che hanno condiviso parte di questa esperienza con me e che mi hanno aiutato a crescere professionalmente e come persona.

Sicuramente, un importante contributo a questo lavoro è stato dato dalla Dott.ssa Francesca Ospitali e, negli ultimi mesi, dai Dott. Fabrizio Tarterini, Franco Corticelli a Andrea Migliori. Che mi hanno aiutato nella caratterizzazione dei catalizzatori, con ore e ore settimanali di analisi SEM / EDS, TEM e Raman.

Ho avuto modo di lavorare con la Prof.ssa Symelis Hernandez e il Dott. Adriano Sacco, del DICAM del Politecnico di Torino. Da loro ho imparato molto sull’EIS e sull’elettrochimica in generale, oltre ad aver dato un contributo molto importante a questo lavoro.

Uscendo fuori da CHIMIND è doveroso dedicare un pensiero ai miei amici e colleghi “nanoscienziati”: Fabio, Alberto, Lucia, Liviana, Laura. Persone stupende, con cui ho condiviso poco dal punto di vista lavorativo, ma mi hanno arricchito tantissimo dal lato umano, spero che queste amicizie non si esauriscano con la fine di questo percorso.

Inoltre, devo ringraziare la mia famiglia, che mi appoggia e supporta nelle mie scelte da sempre e a cui devo tanto. Ringrazio inoltre Giulia, che mi cammina accanto ormai da sei anni e che spero voglia farlo ancora a lungo, così come la “nuova famiglia” marchigiana che mi ha accolto come un figlio.

Infine, non posso dimenticare i miei amici di sempre Daniele, Mattia e Andrea e poi Sergio, Alice e tutti gli altri. Purtroppo la vita e il lavoro ci hanno portati lontani per il momento, ma so che posso contare sempre su di voi.

Grazie ancora a tutti. Questi anni sono stati intensi, pieni di alti e bassi, ed in particolare quest'ultimo per via del Covid, ma grazie a tutti voi li ricorderò sempre con affetto e soddisfazione.

Giancosimo

ABSTRACT

The development of an integrated bio-based economy requires the use of so-called "power-to-X" technologies for the exploitation of electricity for the production of chemicals and fuels, to replace the current processes based on fossil raw materials. In this scenario, the concept of an integrated electro-biorefinery makes it possible to interface the production, storage and use of electricity obtained from renewable sources to produce bio-based chemicals, where these also become useful as energy carriers or for the storage of energy surplus (such as H₂).

The electrochemical conversion is a fully sustainable way for the production of added-value products that allows to operate under mild conditions, using water as source of hydrogen/oxygen generated in-situ and avoiding the use of high H₂/O₂ pressures or strong reducing/oxidant agents.

For this purpose, the aim of this work is to investigate the electrocatalytic conversion of 5-hydroxymethylfurfural and D-glucose using 3D electrocatalysts based on metallic open-cell foams, which allow to increase the surface area and improve electron and mass transfer.

The first part of the work is focused on the electrochemical hydrogenation (or reduction), in alkaline media, of 5-(hydroxymethyl)furfural (HMF) to 2,5-bis(hydroxymethyl)furan (BHMF), a precursor for polymers production, using nanostructured Ag, deposited by galvanic displacement (GD) or electrodeposition (ED) on Cu foam. The catalysts are composed by AgCu bimetallic nanoparticles (ED) or dendrites (GD); compared to the bare Ag and Cu bulk foams both Ag/Cu catalysts showed an enhanced electroactive surface area, as well as charge and mass transfer. These features enhanced the catalytic activity.

In diluted 0.02 M HMF solutions, Ag/Cu samples selectively produce BHMF with high HMF conversion and faradic efficiency (FE). The large surface area enhances the productivity, compared to their 2D counterparts. Furthermore, at more HMF concentrated solutions (0.05 – 0.10 M) the increase in the surface area does not provide an improvement in the efficiency, and a gradually decrease of selectivity is observed. The performance of the electrodes is stable during the catalytic tests but changes on surfaces occurred with Cu-enrichment of bimetallic particles.

In the second part, Ni foam-based catalysts were investigated for the selective electrochemical oxidation of D-glucose, in basic media, toward gluconic acid (GO) and glucaric acid (GA), used in food, pharmaceutical and chemical industries. Firstly, the performance of calcined foams, Ni-hydroxide/Ni and Ni particle/Ni catalysts was investigated, then the best catalyst, obtained by thermal activation of the Ni foam, was chosen to investigate how the reaction conditions influence the reaction mechanism.

The conversion of glucose and also the GO and GA selectivities increase with the charge passed, while the production of arabinose and 2KDG (2-keto-D-gluconic acid) are approximately stable over time. The formation of by-products from C-C cleavage/retro-aldol process is instead maximum at low accumulated charge and decreases with the charge passed. The presence of fructose obtained from glucose isomerization strongly contributes to the formation of low molecular weight products.

The glucose/NaOH ratio influences the activity towards Oxygen Evolution Reaction (OER) and the GO selectivity; too high values suppress the OER, while too low values favour the formation of low molecular weight products. The best performances have been obtained for glucose/NaOH ratio between 0.5 and 0.1. The variation of the potential causes similar effects, indeed as the potential increases the GO selectivity is enhanced. It should be noted that higher GA selectivity is observed with the use of less anodic potentials (0.6 – 0.7V vs SCE), confirmed by catalytic test performed in gluconate. Nevertheless, the maximum selectivity reached of 30-35% indicates the low activity of the catalyst for the production of GA.

The catalyst is stable during the catalytic cycles, the same conversions and GO selectivity were obtained. The post reaction characterization confirms that some changes of catalyst occurred that need further investigation to be clarified.

Index

1. Introduction	1
1.1. The Biorefinery	1
1.1.1. Coupling Biorefinery and Renewable Energy Production: The Electro-biorefinery.....	5
1.2. Electrochemical processes for the production of renewable high-added value products.....	7
1.3. Use of 3D Porous Supports and Nano-structuration to Enhance the Catalytic Activity.....	13
2. Characterization Techniques	16
2.1. Scanning Electron Microscopy – Energy Dispersive Spectroscopy	16
2.2. Field Emission Scanning Electron Microscopy – Energy Dispersive Spectroscopy	16
2.3. Transmission Electron Microscopy.....	16
2.4. X-Ray Diffraction.....	16
2.5. Micro-Raman Spectroscopy	16
2.6. Inductively Coupled Plasma – Atomic Emission Spectroscopy	17
2.7. X-Ray Photoelectron Spectroscopy.....	17
2.8. Electrical Resistivity Tomography	17
3. Electrochemical valorisation of 5-(hydroxymethyl)furfural (HMF).....	19
3.1. Electrochemical oxidation.....	19
3.2. Electrochemical hydrogenation.....	20
3.2.1. Electrochemical hydrogenation of 5-hydroxymethylfurfural	22
3.2.2. Ag nanostructured on Cu foams for the selective electrochemical hydrogenation of HMF to BHMF	25
3.3. Experimental section	26
3.3.1. Materials and chemicals.....	26
3.3.2. Synthesis of electrocatalysts	26
3.3.3. Electrochemical measurements.....	27
3.3.4. Products Analyses	29
3.4. The role of three-dimensional support and nanostructuring of AgCu bimetallic particles .	30
3.4.1. Characterization of Ag/Cu foams and foils electrocatalysts.....	30
3.4.2. Electrochemical Characterization	40
3.4.3. Electrochemical hydrogenation of low concentrated HMF solutions.....	43
3.4.3.1. Electrochemical characterization of electrocatalysts.....	43
3.4.3.2. Electrolysis of a 0.02M HMF solutions.....	46
3.4.3.3. Stability tests in 0.02M HMF solutions.....	48
3.4.4. Selective Hydrogenation of concentrated HMF solutions	49

3.4.5.	Influence of the Area-catalyst/Volume-reaction ratio	52
3.4.6.	Identification of By-products	53
3.4.7.	Effect of reaction time.....	57
3.4.8.	Characterization of electrocatalysts after electrochemical tests	58
3.5.	Conclusions	62
4.	Glucose as Platform Molecule	64
4.1.	Electrochemical Conversion of Glucose	65
4.2.	Glucose Oxidation Reaction.....	67
4.2.1.	Non-enzymatic Glucose Sensors	67
4.2.2.	Direct Glucose Fuel Cells (DGFCs)	68
4.2.3.	Selective Electrochemical Oxidation to Gluconic and Glucaric Acids	68
4.3.	Experimental Section	73
4.3.1.	Materials and Chemicals	73
4.3.2.	Synthesis of Electrocatalysts.....	73
4.3.3.	Electrochemical Measurements	74
4.3.4.	Products Analyses	75
4.4.	Study of the Selective Electrochemical Conversion of Glucose solutions with Ni foam-based electrocatalysts	77
4.4.1.	Characterization of Ni-based Electrocatalysts	77
4.4.2.	Electrochemical Characterization of electrocatalysts	81
4.4.3.	Electrochemical Conversion of 50 mM Glucose in NaOH 0.1M electrolyte	84
4.4.4.	Effect of charge passed	88
4.4.5.	Effect of glucose concentration.....	90
4.4.6.	Effect of the Glucose/NaOH ratio.....	93
4.4.7.	Influence of Fructose Electrolysis in Glucose Oxidation	96
4.4.8.	Effect of applied potential in glucose 0.50 M solutions with NaOH 0.1 M	98
4.4.8.1.	Effect of the Potential on the Selective Electro-oxidation of Gluconic Acid to Glucaric Acid	100
4.4.8.2.	Effect of Gluconic Acid Concentration	103
4.4.9.	Stability Test for glucose electro-oxidation over NiC500-1h foam.....	104
4.4.10.	Electrochemical Characterization of used catalysts.....	105
4.4.11.	Characterization of used Ni-based Electrocatalysts.....	107
4.5.	Conclusions	109
5.	Conclusion Remarks and Outlook.....	111

1. Introduction

Nowadays a large fraction of energy and materials are obtained from fossil fuels, mainly from oil refinery. Due the environmental problems, related to greenhouse gases emissions, and the depletion of fossil raw materials, significant efforts have been made to research renewable and sustainable sources for energy and materials production. Electricity and heat can be provided by several renewable energy alternatives (wind, sun, water, and geothermal), whereas the only renewable C-containing source, available on the Earth, is biomass.¹ In this context, biomass could play a crucial role for the manufacture of valuable chemicals and fuels, and to decrease CO₂ emissions caused by fossil fuel.

Biomass is a common, economic and democratic source, largely widespread in the world. It is renewable and has a neutral carbon balance; indeed, its growth involves the use of carbon from atmosphere, as CO₂, collecting energy from the Sun and converting it into chemical energy. The worldwide annual production of biomass is equal to ca. 10¹¹ tonnes (2014), which is divided into ca. 60% terrestrial and 40% aquatic. Only 3% of this is cultivated, harvested and used (in food and non-food applications). It consists of ca. 75% carbohydrates and 20% lignin, with the remaining 5% comprising triglycerides (fats and oils), proteins and terpenes.²

There are a lot of biomass varieties such as lignocellulosic biomass, herbaceous and agricultural biomass, aquatic biomass, animal and human biomass wastes, and their origin defines its composition. Thanks to its chemical complexity, biomass is a potential substitute of oil refinery by the implementation of an *integrated biorefinery* in which fuels, commodity chemicals, platform molecules and novel materials will be produced. An additional benefit could be derived from the substitution of existing products by bio-derived alternatives, with reduced environmental footprints, as biofuels and biocompatible and biodegradable plastics.²

1.1. The Biorefinery

A biorefinery is a facility that optimizes the integrated production of heat, power, fuels, materials, chemicals, feed and food from biomass, maximizing the value derived from biomass.^{1,3} It can be defined as: “the sustainable processing of biomass into a spectrum of marketable products and energy”. This concept includes a wide range of technologies able to separate biomass feedstock into its building blocks (carbohydrates, proteins, fats, etc.), which can be converted to value-added products (chemicals/materials) and energy (biofuels, power, heat).¹ Biorefinery is the analogous to today’s petroleum refinery, which produces multiple fuels and products from petroleum. However, the structure of biorefinery is totally different and represents a change from the traditional paradigm

of oil refinery, based on the large exploitation of natural non-renewables resources and the large wastes production, instead biorefineries moves towards integrated systems in which all resources are used.⁴

Crude oil is a raw material composed by a mixture of different organic hydrocarbon compounds, low in oxygen content with some sulphur, nitrogen and other elements (as heavy metals) present in smaller quantities. The crude oil is initially subjected to the removal of water and impurities, followed by distillation into different fractions as gas, light and heavy gasoline, kerosene, diesel, lubricating oils, bitumen. These fractions are subsequently sent to specific processing and refining chains (eg. reforming, cracking, etc.) for further processing. The intermediate product obtained can be chemically modified, to introduce heteroatoms (O, N, S) and to obtain various building block, as ethylene, propylene, BTX, and many others, used for the production of added values chemicals (Figure 1.1).^{4,5}

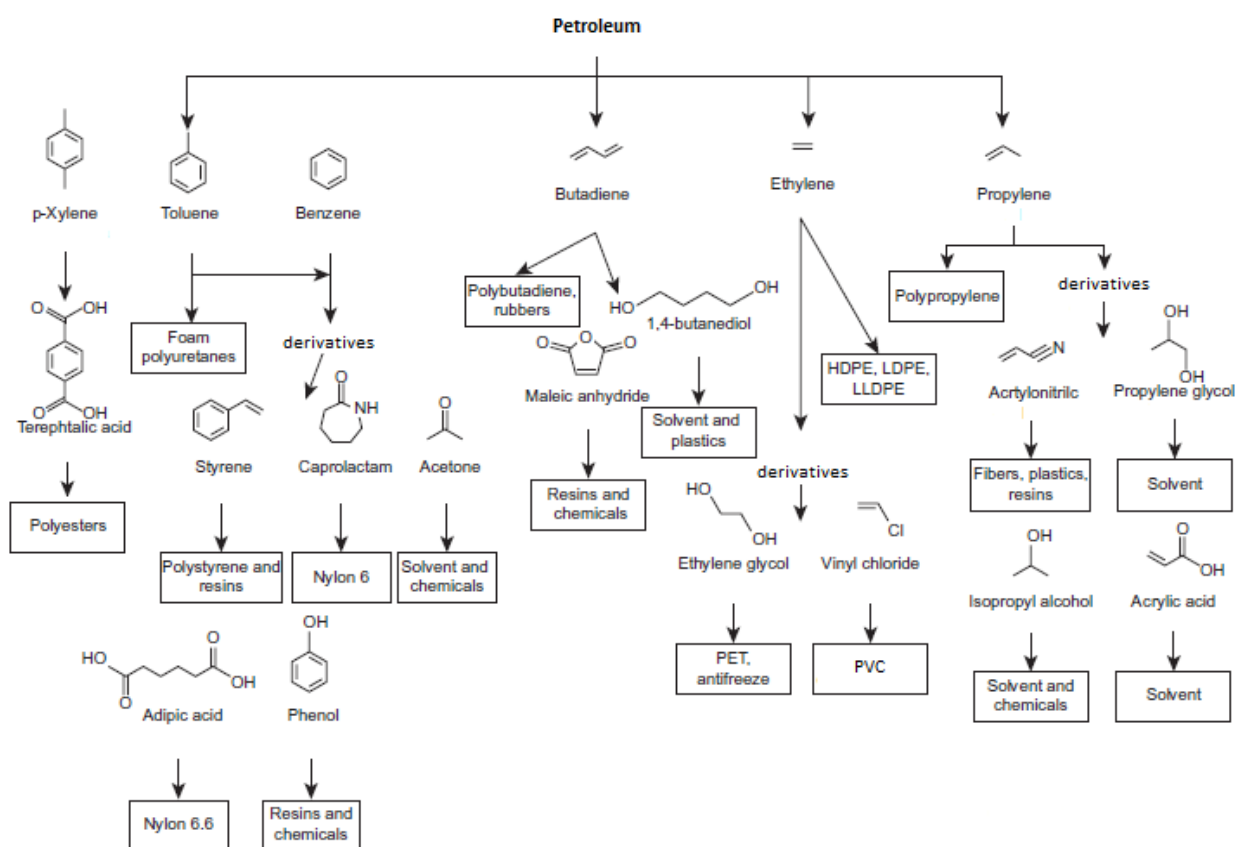


Figure 1.1. Products from oil refinery: building blocks and chemicals derived from their transformation. Adapted from de Jong, et al. “Biorefinery Concepts in Comparison to Petrochemical Refineries” (3–33), in *Industrial Biorefineries and White Biotechnology*, Elsevier B.V., 2015.

Conversely, biomass is not homogeneous and contains a considerable amount of water, in fact initial processing may be required to eliminate water and increase the energy density, to reduce transport, handling and storage costs. The elemental composition of biomass is rich in heteroatoms, in particular

oxygen, depending on its origin, and frequently requires deoxygenation processes. This variety in composition is both an advantage, because biorefineries can produce more classes of products than petroleum refineries, and also a disadvantage, because a larger and different range of processing technologies is needed to separate and give value to the various biomass components. There are many different building blocks that can be obtained from biomass, such as Glucose, Fructose, Xylose and Fatty acids, obtained by a combination of chemicals and bio-chemicals transformations and useful for the production of various platform molecules (Figure 1.2).^{4,5}

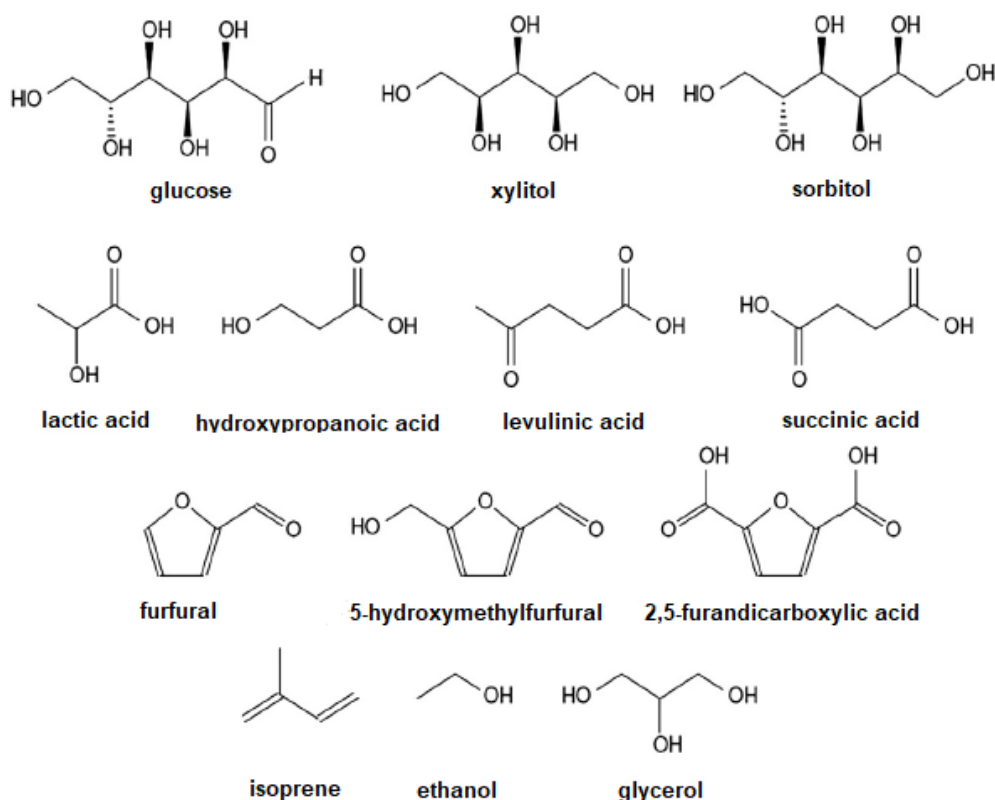


Figure 1.2. Platform molecules produced from biomass. Adapted from de Jong, et al. “Biorefinery Concepts in Comparison to Petrochemical Refineries” (3–33), in *Industrial Biorefineries and White Biotechnology*, Elsevier B.V., 2015.

Nowadays, it might be still very attractive to integrate biomass processing in traditional refineries as a way to upgrade and convert conventional refineries. Examples include the production of “green biodiesel” in Porto Marghera and Gela biorefinery (Petrobras/H-BIO, UOP with ENI) produced by hydrogenation of plant oils using hydrogen made by the refinery.^{5,6}

However, the inhomogeneity and seasonality problems of biomass can be solved by developing biorefineries as dispersed industrial complexes, unlike oil-refinery, with a whole range of different-sized plants, able to revitalize rural areas⁵. The construction of industrial plants in the optimal location is related with the available biomass (e.g. quantity, accessibility, weather conditions, etc.). For

example, the estimated crop residues in EU could support around 850 plants, which are expected to produce annually about 150×10^{10} MJ of bioenergy. Anyway, integrated biorefinery can be made from the side streams derived from different industrial processes (e.g. juice processing, breweries, wineries, sugar production from sugar beet, pulp and paper industry, etc.)⁷.

In this context, several bio-industries can combine their material flows in order to reach a complete utilization of all biomass components, giving rise to integrated bio-industrial systems. In addition, the distribution of feedstock in world may contribute to reduce national dependence on imported fossil fuels⁵. To achieve the development of this industrial model, economic and environmental benefits must be gained. Usually, the main promoting factor, and also the main challenge, for the future development of biorefineries system is considered the efficient and cost effective production of biofuels, whereas the coproduced biomaterials and biochemicals are additional economic benefits⁴. In any case, the development of several technologies, able to allow the efficient separation and treatment of different bio-based raw materials, is needed.

On the base of the feedstocks used, the conversion processes, the status of the technology and the output, biorefineries can be classified as:⁸

- *Phase I Biorefinery*: Only one feedstock material can be processed, with a fixed processing capability, producing a single primary product. Examples: biodiesel from vegetable oil, and ethanol from corn grain;
- *Phase II Biorefinery*: similar to a Phase I, but it is capable of producing various products. Examples: various chemicals from starch and multiple carbohydrate derivatives and bioethanol from cereal grains.
- *Phase III Biorefinery*: it is an advanced biorefinery and can utilize various types of feedstocks and processing technologies to produce multiple types of products. There are four classes of Phase III Biorefinery systems: whole-crop biorefinery, green biorefinery, lignocellulosic biorefinery, and two platform concept biorefinery.

In the wide range of the products, we can identify two macro groups: fuels/energy and commodities (bulk or fine chemicals). Thus, depending on the preferential product, biorefineries can be distinguished in “product-driven” and “energy-driven”. The former primarily generate biobased products (biomaterials, chemicals, feed, etc.), and residues are used to produce biofuel, heat and power (for internal use or sale); in the latter the biomass is primarily used for the production of secondary energy carriers (biofuels, power, and/or heat). Both primary products and energy-driven processes are considered as true biorefinery approaches provided that the final goal is the sustainable processing of biomass.⁴

Sustainability is considered as the main driver for the establishment of biorefineries; all biorefineries should be assessed for the entire value chain on their environmental, economic, and social sustainability covering the whole life cycle. According to the origin of feedstock used, biomass, and consequently biorefinery, can be classified as 1st, 2nd and 3rd generation.⁹ First generation biomass are dedicated food crops resources, as maize, sugar beets, rapeseed, peanuts, edible oil seeds; Second generation biomass include non-food materials, such as agricultural residues, forest, waste-based, wood and energy crops. Lastly, algae and microalgae have been referred as third generation biomass. The use of first generation biomass is not a sustainable option in the longer term, because it competes, directly or indirectly, with food industry and arable land allocation.^{2,9,10} Instead, second and third generation biomass represent the key feedstocks for a biorefinery; they are not suitable for human consumption and are not in competition with food industry, moreover they have a relatively low price and are available in high quantities.^{2,10,11}

Today, bioethanol and biodiesel represent the first generation biofuels, produced from readily processable bioresources as sucrose, starch, and plant oils from grains. Recently, research attention has shifted toward the next-generation biofuels, derived from second and third generation feedstock.¹² Among the potential large-scale industrial biorefineries, the LCF (lignocellulosic feedstock) biorefinery will most probably be pushed through with the highest success.¹³ Lignocellulosic biomass clearly represents a sustainable and low-cost resource that can be converted into fuels and chemicals on a large scale, having a meaningful impact on petroleum use. They are also attractive because enable the development of products with new functionalities and molecules that would otherwise be either less accessible or inaccessible via fossil-based routes. Moreover, they respond to the market pull that is resulting from consumer and retailer demand.^{13,14}

1.1.1. Coupling Biorefinery and Renewable Energy Production: The Electro-biorefinery

A further aspect to consider, for the development of a total sustainable and fossil-free pathways for fuels and chemicals production, is heat and power generation into the industrial processes.

Currently, chemical processes operate thermo-chemically under stationary conditions, and the production of chemicals has a significant economy of scale. In contrast, biorefineries are limited by local availability and transport of biomass.

At the same time, the electrical power production is under switching from fossil raw materials to renewable sources as solar, wind, hydroelectric, etc. This leads to global gradually increasing shares of renewable energies on the overall electric energy production.

In this context, electrochemical processes for the transformation of biomass feedstock represent a viable means to account for the change in energy supply, and biorefinery could become a facility for renewable electricity storage, named as *Electro-biorefinery* (Figure 1.3), to improve the efficiency of electricity generation processes. This is a potential solution for the fluctuating availability of renewable resources for electrical power production and temporary downtimes of solar or wind plants.^{15,16} The technologies that use electricity-driven reactions are defined as **power-to-X technologies**, where the “X” is ”heat”, “fuels” or “chemicals”.^{16,17} Most prominently, Power-to-Hydrogen is the process that uses electrolysis to split water into hydrogen and oxygen. H₂ is a carrier for electric power storage and supply;^{16,18} it can be stored, transported as a liquid or a gas and can be combusted or used in fuel cells, to generate heat and electricity for mobility applications or industrial uses.¹⁸ Furthermore, it is also a key element for the production of value added products such as methanol, formic acid, formaldehyde.¹⁷ Hydrogen can be produced, by water electrolysis, during times of excess renewable electricity and it can be converted back to electricity to provide power when the renewable source is unavailable, helping stabilise the utility grid.¹⁸

Among other important chemicals, hydrogen peroxide can be derived from the oxygen reduction reaction (ORR); carbon dioxide, captured from the atmosphere or directly from point sources, could become a feedstock for fuels, commodities and fine chemicals via preliminary electroreduction; nitrogen can be electroreduced to ammonia for the sustainably and locally production of fertilizers, at the required concentration.¹⁹

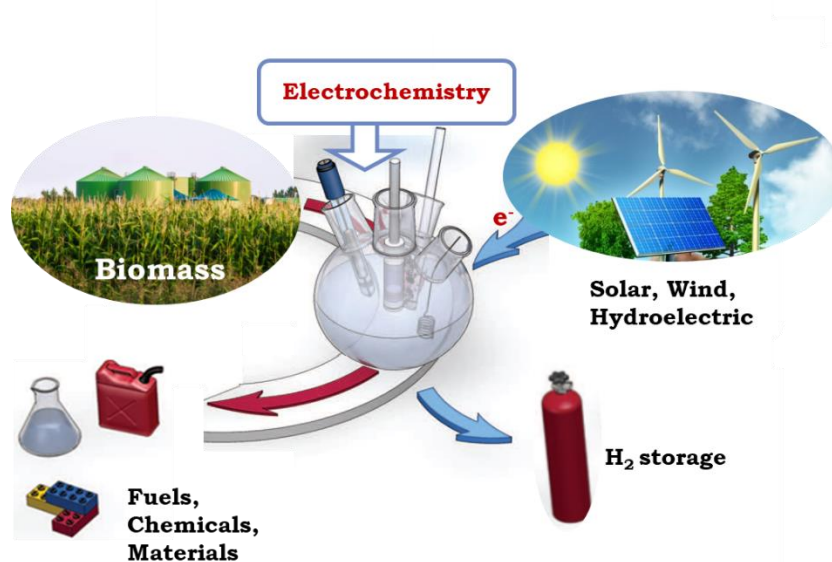


Figure 1.3 Example of a sustainable scenario involving electrochemical processes for the production of fuels, energy carrier and commodities. Adapted from “Combining theory and experiment in electrocatalysis: Insights into materials design”, Seh et al., Science, 355, 2017.

When it comes to Power-to-Chemicals as well as Power-to-Fuels, commodities directly produced from electricity are currently very limited. A well-known process is the production of chlorine and caustic soda with chlor-alkali electrolysis, with a production of $77 \cdot 10^6$ t/y; this is one of the largest chemical processes worldwide and dates back over 100 years, originating from the electrolysis of brine using mercury (Hg) as electrode. Also, the electrochemical production of aluminium is one of the most successful examples of how electrochemical process can reduce the cost of commodities; alumina, produced from bauxite, is reduced electrolytically to aluminium in the Hall–Héroult process. Finally, the electrosynthesis of adiponitrile, a key intermediate for Nylon 6,6 production, from acrylonitrile in the most successful organic electrosynthesis process; the production of this molecule is obtained by the Baizer-process with a volume of ca $400 \cdot 10^6$ t/y.^{16,17,20}

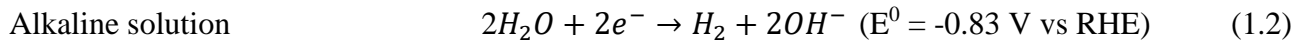
Nevertheless, recently, several examples of electrochemicals transformations of biomass-derived platform chemicals were investigated, as the oxidation and reduction of biomass-derived raw material and platform molecules. The selectivity control of these processes is the main challenge. Therefore, the electrode design besides the selection of the suitable electrolyte systems and process concepts is generating growing interest.¹⁵ There are several advantages of electrocatalytic processes over other conventional methods in biomass conversion:²¹

- H₂O used as solvent and as proton/oxygen source, instead of H₂/O₂ gas;
- Low operating temperatures and pressures;
- Precise control of the reaction rate and selectivity by applying a constant potential or current;
- Simultaneous production of oxidation and hydrogenation products in a continuous membrane reactor.

1.2. Electrochemical processes for the production of renewable high-added value products

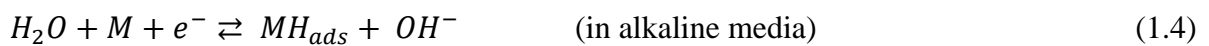
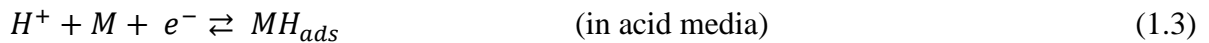
Like conventional catalytic processes, electrocatalytic processes also include electro-oxidation and electro-reduction reactions for the production of chemicals and commodities. As example, one of the most “simply” and attractive process to produce hydrogen as fuel or as reactant, together with oxygen, for chemical industry is water splitting. However, its practical application is limited by the unfavourable thermodynamics, hence, the use of electrocatalysts is needed, to overcome the large overpotential (η) of the process which cause a low efficiency and high energy consumption. The process is composed of two half reactions: *Hydrogen Evolution Reaction (HER)* and *Oxygen Evolution Reaction (OER)*.²²

The **Hydrogen Evolution Reaction** is a two-electron transfer reaction, with one catalytic intermediate, H_{ads} , and may occur through either the Volmer-Heyrovsky or the Volmer-Tafel mechanism as showed in Figure 1.4. Depending on the pH of the electrolyte, HER can be described as the following equations (1.1, 1.2):^{22,23}

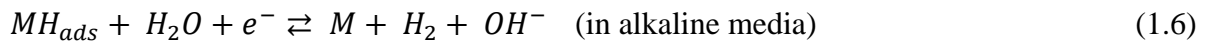
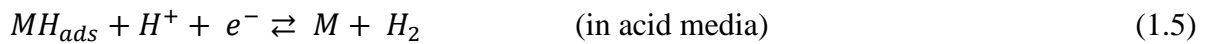


The process start with the adsorption of a proton on an active site of the catalyst surface (Volmer step - 1.3, 1.4), followed by the evolution of molecular gas H_2 ; the production of the hydrogen molecule can take place by a second proton/electron transfer (Heyrovsky step - 1.5, 1.6) or through the recombination of two adsorbed protons (Tafel step - 1.7).^{22,24} This last step depends on the amount of H_{ads} on the catalyst surface: with low coverage the process proceeds with Heyrovsky step, otherwise the Tafel pathway is preferentially followed.²⁴

a) Volmer step



b) Heyrovsky step



c) Tafel step



with MH_{ads} that is the proton chemically adsorbed on an active site of the catalysts (M).

However, the HER in alkaline media is less favoured than in acidic media, because of the reversible adsorption of H atom formed from the dissociation of water.²²

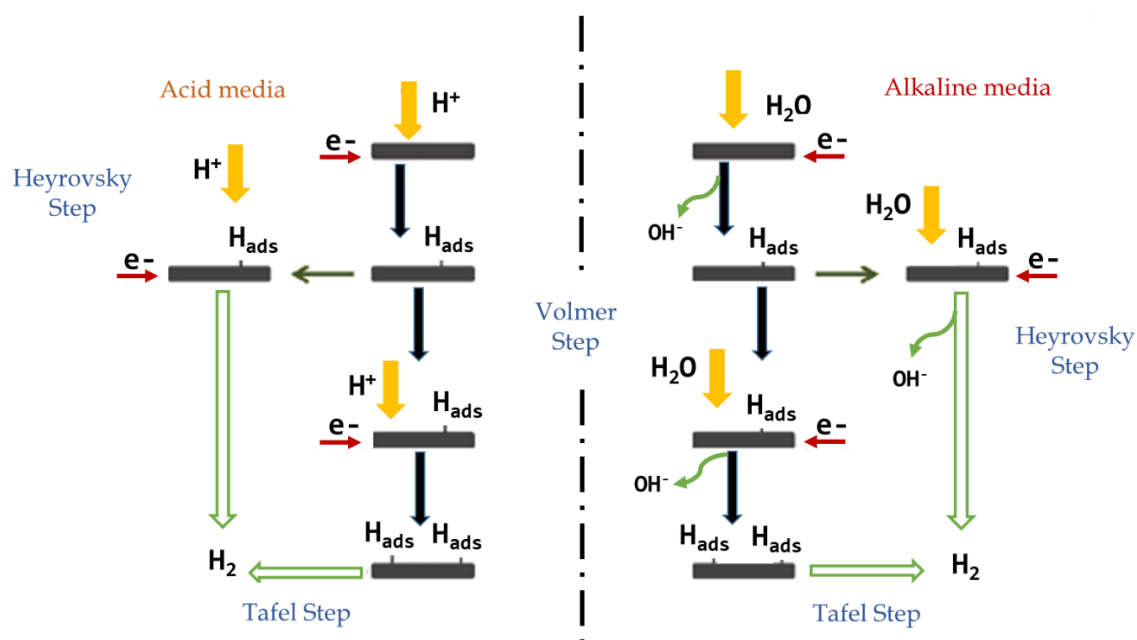
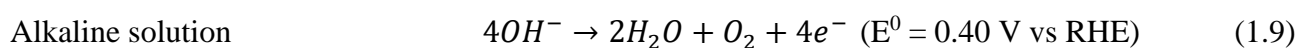
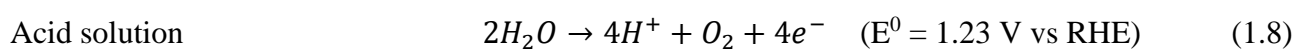


Figure 1.4: Reaction pathway proposed for HER in acid and alkaline media. Adapted from “A review of the electrocatalysts on hydrogen evolution reaction with an emphasis on Fe, Co and Ni-based phosphides”, Ge et al., J. Mater. Sci. 55, 14081–14104, 2020.

The free energy of hydrogen adsorption (ΔG_H) is commonly used to theoretically evaluate the HER activities of catalytic materials.²² Pt group noble-metals, with a ΔG_H value of approximately zero, are the most active single-metal catalyst, but their scarcity and high cost limiting their application; as a result, precious-metal-free electrocatalysts are intensively studied as alternatives.^{24–26}

Thanks to the catalytic activity of Ni, Fe and Cu elements, they can be used as electrocatalysts for HER or as support materials for noble and non-noble active phases.²⁵ A Pt/Ni electrocatalyst, using nickel foam as electrode support, was reported as active catalyst for HER;²⁷ moreover, also transition metals oxides and their derivatives as MoO_2 , WO_2 , Ni–NiO/ Cr_2O_3 , Co/ Co_3O_4 , etc. as well as their sulphides, phosphides and selenides, showed excellent catalytic activities for HER, combined with their abundance, low cost and high stability.^{19,24,25}

In contrast to HER, **Oxygen Evolution Reaction** is a multi-step proton-coupled electron transfer (Figure 1.5), with a relative slow kinetics and high activation energies. This is the rate-limiting step in water splitting and significantly impedes the commercial viability of industrial hydrogen production. The process can be described as the equations (1.8, 1.9) at different pH:^{25,28}



As discussed for HER, also OER pathways depend on the pH of electrolyte. Many mechanisms have been proposed, for acidic or alkaline electrolytes; nevertheless, most of the proposed mechanisms include the same intermediates (MOH and MO), with the main difference concerning the final step for oxygen evolution. As shown in Figure 1.5, there are two different approaches to form oxygen from a MO intermediate: the first one involves the direct combination of 2MO to produce O₂(g) (yellow route), while in the second one a MOOH intermediate is formed (green line) and subsequently decomposed to O₂(g).

Due the kinetic problems and the high overpotential of OER, the development of an efficient electrocatalyst is mandatory, to reduce the overpotential, accelerate the reaction rate and enhance the energy conversion efficiency.²⁵ As usual, noble metals, and particularly Ru and Ir oxides, are very active catalysts in acid and base media. However, to substitute noble metal, first-row transition metal-based catalysts with their oxides and hydroxides has been recently investigated, although their activity is inevitably limited by their low conductivity.^{25,28}

For instance, NiFe, NiCo, CoFe, etc., layered double hydroxides (LDHs) and Ni, Co, Fe perovskite doped with different amounts of alkaline-earth and/or rare-earth metals (as Ba, Sr, La, etc.), providing surprising OER catalytic performances. Also spinel compounds are good electric conductors and very stable in alkaline solution under high anodic potential. Spinel oxides for OER are iron-based (ferrite) and cobalt-based compounds with other transition/alkaline metals dopants such as Mn, Ni, Cu, Zn and Li. Layer structure type oxides, including transition metal oxides and hydroxides, exhibit high electrocatalytic activity for OER. Finally, transition metal chalcogenides, phosphides and nitrides, originally used for HER, have been investigated thanks to their excellent electro-conductivity (fast charge transfer ability) and chemical resistance in strong acid/alkaline electrolyte.^{25,28}

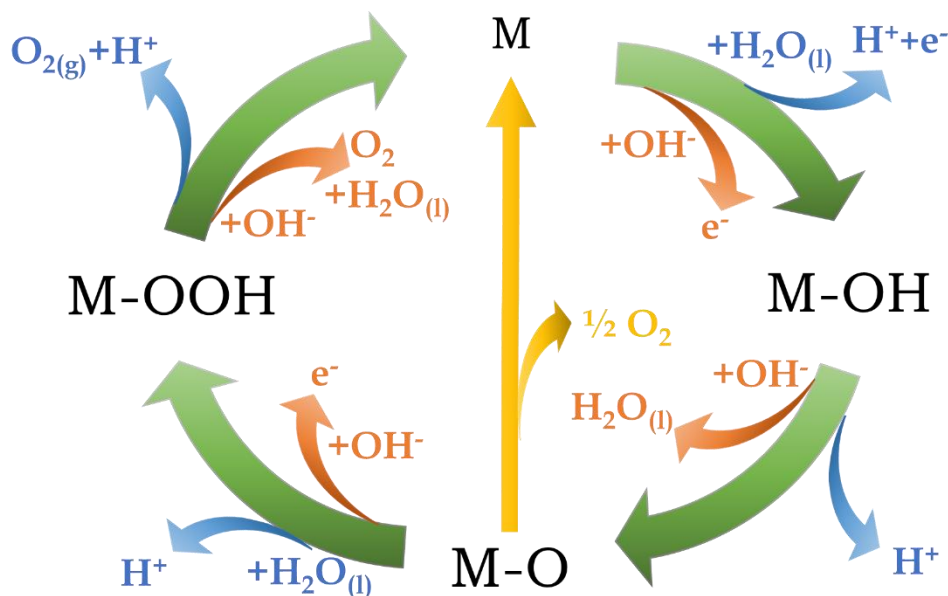


Figure 1.5. Reaction pathway proposed for OER in acid and alkaline media. Adapted from “Electrocatalysis for the oxygen evolution reaction: Recent development and future perspectives”, Suen et al., Chem. Soc. Rev. 46, 337–365, 2017.

Beyond these aforementioned reactions, there are a lot of other important energy conversion reactions involving the electroreduction or oxidation of different substrates as CO₂, 5-hydroxymethylfurfural, levulinic acid, glucose and carbohydrates for the production of value-added products, using renewable energy as an input. Moreover, electrochemistry is a promising way for the depolymerization of recalcitrant compounds such as lignin.¹⁵

The direct electrochemical reduction of CO₂ represents a powerful method to recycle and transform anthropogenic CO₂ emission into feedstock chemicals and fuels.²⁹ Electrochemical reduction of CO₂ can be achieved at ambient conditions, which minimizes environmental impact and safety hazards.³⁰ Many possible products can be obtained from carbon dioxide reduction, such as CO, formate, formaldehyde, methane, methanol, and C₂+ hydrocarbons and oxygenates, which require a large number of protons and electrons transferred.^{25,29} Anyway, the nature of the electrocatalysts determine the main product, indeed they are typically grouped by favoured majority product as example formate (tin, lead, mercury), carbon monoxide (silver, gold, zinc), methane and hydrocarbon (copper).^{29,30} It should be noted that ethylene and, in particular, CO represent products of significantly added value, can be employed in conventional chemical process for the generation of commodities.²⁹ Currently, the studies in CO₂ reduction catalysts are focused towards the increasing of energy efficiency and decreasing the overpotential of the process; increasing the stability and durability of the catalysts; enhance the selectivity of a specific product.³⁰

Considerable efforts have been made on studying electro-valorisation of biomass-derived intermediates and platform molecules.^{21,31,32} For instance, glycerol, a C3 polyol that is the main by-product derived from biodiesel production, with a production of million tonnes/y, can be electrochemically converted in several value-added building blocks, such as hydroxypyruvate, dihydroxyacetone, glycerate, glyceraldehyde, tartronate, etc. Different degree of oxidation can be achieved using noble-metals catalyst as Pt, Au, and Pd in acid or alkaline media varying the applied potential.³²

Carbohydrates, such as C5 and C6 sugars and in particular glucose, are extremely abundant in nature, and can be used as renewable feedstock for fuels and chemicals²⁹. Glucose is a versatile platform molecule; its electro-oxidation is an interesting and challenging route for the production of glucaric acid, an added-value intermediate for the synthesis of adipic acid, performed with noble^{33,34} and non-noble metals,^{35,36} in alkaline media in room conditions. Instead, sorbitol is the most important electrochemical reduction product of glucose, and it is used in many industrial field as food, cosmetic and pharmaceutical; for instance, sorbitol is a building block for the synthesis of vitamin C. The electroreduction of glucose can be performed directly with a Pb cathode or indirectly by using a Raney-Ni cathode.²⁹

On the other hand, carbohydrates can be chemically converted to produce many others bio-based intermediate and chemicals. Furfural and 5-hydroxymethylfurfural have potential as alternative commodity chemicals to fossil-fuel-based platform chemicals, they can be electrochemically oxidized and hydrogenated/reduced to obtain many different products, e.g. furoic acid, furfuryl alcohol, 2-methylfuran, 2,5-furandicarboxylic acid, 2,5-dimethylfuran, 2,5-bis(hydroxymethyl)furan and even 2,5-hexanedione, used as solvents, as intermediates in pharmaceutical and polymer industry (precursors or additives) or as fuels. The selectivity of the process is strongly dependent not only on the nature of the catalysts employed, but also on the pH and the potential used.²¹

Also, levulinic acid is an important precursor for liquid biofuel and chemicals, produced from glucose. The electroreduction of levulinic acid towards valeric acid or γ -valerolactone was investigated in aqueous acidic solutions, at room temperature. Valeric acid could be further transformed by Kolbe electrolysis in an aqueous or organic solvent to n-octane.³⁷

Moreover, besides cellulose and hemicellulose, lignin is one of the most abundant bio-polymer in nature. The importance of lignin valorisation concerns its polyphenolic structure, which represent a potential sustainable and renewable raw material for aromatic chemicals. Particularly, Vanillin is an aromatic added-value fine chemical used in pharmaceutical, cosmetic and food industry, it can be obtained by electro-oxidative depolymerisation of lignin in mild condition and alkaline media.^{38,39}

1.3. Use of 3D Porous Supports and Nano-structuration to Enhance the Catalytic Activity

The efficiency and the selectivity of an electro-catalytic process depends not only on the reaction conditions (potential, pH, electrolyte, temperature) but also on the type (composition and shape) of the catalyst.^{25,30,40}

To improve the activity of an electrocatalyst, two strategies can be followed:¹⁹

- increasing the number of active sites on a given electrode, by increasing the active phase loaded or improving the structure of the catalyst (exposed active sites);
- increasing the intrinsic activity of each active site.

Nevertheless, there are physical limits to how much catalyst material can be loaded onto an electrode without affecting other important processes, such as charge and mass transport. On the other hand, increasing the intrinsic activity enhances the electrode performance and mitigates transport issues due to high catalyst loads; moreover, the decrease of the active phase loaded also reduces the catalyst costs.¹⁹

Several methods have been developed to improve the activity of the electrodes, i.e. engineering porous nanostructures, doping the active phase with metals or non-metal elements, and designing three dimensional (3D) electrodes.²⁵

Compared with 2D supports, the 3D porous structure enlarges the surface area, increases the number of catalytic active sites and shortens mass and ion diffusion length; this allow to greatly improves the activity of the electrocatalyst, which can be directly employed as a working electrode, by forming free-standing films.⁴¹ Various effective means have been developed to fabricate porous nanostructures, such as the sacrificial template method, thermal decomposition of precursor materials, thermal carbonization of metalorganic–framework grown on current collectors, etc. These methods allow the formation of macro- (>50 nm) and meso-pores (2–50 nm) into the 3D structures.²⁵

Three dimensional macroporous foams, such as Ni foam, Cu foam, carbon and graphene foam, etc., can be directly used as catalyst or as support, or current collectors, to grow or load active phases.²⁵

In particular, in 3D metal foams the macroporous structure enhances the catalytic activity and the conductive and continuous three-dimensional framework enables an excellent mechanical strength and a fast electron-transfer.^{25,41}

Besides the advantages of employing the 3D macroporous structure, the designing of micro- and nano-structured catalysts is also an efficient strategy to increase the surface area; indeed, nano-structuration not only improves the number of active sites per geometric area but also facilitates the

diffusion of ions, electrolyte and generated gas. Hence, nanostructured electrocatalysts may enhance the reaction rate or lower the onset potential.^{26,42}

For instance, Nickel metal foam exhibits the best electrocatalytic activity for water splitting reaction among non-noble materials. Moreover, foams can be decorated with micro-/nanoscale noble metal particles^{27,43} produced by electrodeposition. Combining a rational nanostructure and porous morphology not only increases the number of active sites and reduces the catalyst amount (and its cost) but also contributes to decrease the overpotential related to resistances of ions, gas diffusion and charge transfer.²⁶ Again, foams structure facilitates the homogeneous distribution of electrodeposited noble metal particles, and the direct growth of active materials on foam surface also enhances the catalyst–substrate contact, for an efficient electron transport during reaction^{41,42}

Galvanic displacement and electrodeposition are two simple and cheap techniques for the nanostructuring of several shape of supports, with different metallic particles morphologies.

Galvanic displacement is an electro-less deposition method based on a electrochemical redox reaction (1.10) in which both anodic and cathodic processes occur, simultaneously and spontaneously on a substrate, when a “less-noble” metal substrate (S) comes into contact with a more noble metal cation (M), where the nobility of metals depends of their standard redox potential (Table 1.1). In this case, it is thermodynamically favourable the reduction of noble metal cation, which is deposited on the solid metal surface, to the detriment of non-noble metals that is oxidised.^{44,45}



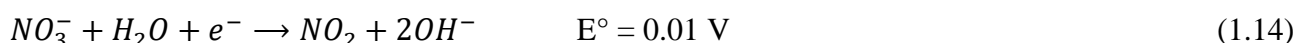
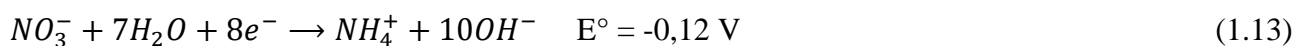
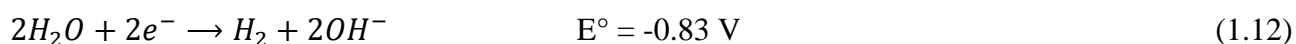
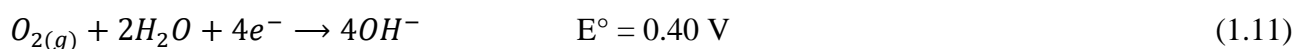
Electrochemical Deposition (or **Electrodeposition**) is an efficient and convenient method for synthesizing metal nanostructures in high yields.⁴⁵ This technique occurs by applying and controlling either the electrode potential or the current density of the electrochemical cell; it involves the use of a two- or three-electrode electrochemical system, with the electrolyte, containing the metal precursors, as conducting medium.⁴⁶ This method allows the growth of the nanostructures in one step, directly on the final support, improving the electron pathway within the substrate; it is used to fabricate thin films or layers composed of nanoparticles or nanocrystals as well as nanowires and nanorods^{46,47} depending of several parameters as the reaction time, applied potential and the addition of suitable surfactants.⁴⁵

Table 1.1 Standard redox potential of different transition metals

<i>Reaction</i>	<i>E⁰ (V vs RHE)</i>
$\text{Au}^{3+} + 3e^{-} \rightleftharpoons \text{Au}$	1.498
$\text{Pt}^{2+} + 2e^{-} \rightleftharpoons \text{Pt}$	1.180
$\text{Pd}^{2+} + 2e^{-} \rightleftharpoons \text{Pd}$	0.951
$\text{Ag}^{+} + e^{-} \rightleftharpoons \text{Ag}$	0.800
$\text{Ru}^{2+} + 2e^{-} \rightleftharpoons \text{Ru}$	0.455
$\text{Cu}^{2+} + 2e^{-} \rightleftharpoons \text{Cu}$	0.340
$\text{Ni}^{2+} + 2e^{-} \rightleftharpoons \text{Ni}$	-0.257

In addition, the **Electro-base generation** method is a suitable, cheap and green method, to quickly and directly precipitate oxides, hydroxides, LDHs, etc onto different shaped metal substrates.⁴⁸⁻⁵²

The process involves the electro-generation of a base (OH^{-}) as a consequence of the application of a cathodic potential pulse, this cause a local increasing of the pH close to the electrode/electrolyte interface. The increase of the pH is caused by the reduction of water (eq. 1.11 - 1.12) and metal precursor species. As example, in presence of nitrates by the eq. 1.13 – 1.14.^{49,53}



These processes compete with the metal ion reduction reaction and the process with the most positive E° value would be preferred. Usually, the (1.13) and (1.14) have a more positive E° than the most metal ion (except for those of Cu^{2+} , Ag^{+} , and Bi^{3+}). As a result metal deposition does not take place, due the formation and deposition of hydroxide specie.⁵³

2. Characterization Techniques

2.1. Scanning Electron Microscopy – Energy Dispersive Spectroscopy

The morphology of the electrodes surface was examined by Scanning electron microscopy/energy dispersive spectroscopy (SEM/EDS) using an EP EVO 50 Series Instrument (EVO ZEISS) equipped with an INCA X-act Penta FET Precision EDS microanalysis and INCA Microanalysis Suite Software (Oxford Instruments Analytical). The accelerating voltage was 20 kV and the spectra were collected in duration 60 s.

2.2. Field Emission Scanning Electron Microscopy – Energy Dispersive Spectroscopy

In order to investigate the surface of nanostructured catalysts with higher definition, a field emission scanning electron microscopy/energy dispersive spectroscopy (FE-SEM/EDS) was employed. The instrument was a ZEISS Leo 1530 equipped with an INCA EDS microanalysis and INCA Microanalysis Suite Software (Oxford Instruments Analytical). The accelerating voltage was 10 kV and the EDS spectra were collected during a period of 60 s.

2.3. Transmission Electron Microscopy

Transmission electron microscopy characterization was carried out by a TEM/STEM FEI TECNAI F20 microscope, equipped with an EDS analyzer. The coating was removed by scratching the foam surface and then suspended in ethanol under ultrasounds for 2 h. The suspension was subsequently deposited on a holey carbon film supported by an Au grid and dried at 100°C, before doing the measurement at 200 keV. Particle size distribution was processed considering around 300 particles.

2.4. X-Ray Diffraction

The X-ray diffraction (XRD) analysis was carried out using a PANalytical X'Pert diffractometer equipped with a copper anode ($\lambda_{\text{mean}}=0.15418\text{nm}$) and a fast X'Celerator detector. Wide-angle diffractogram was collected over 2θ range from 3 to 80° with a step size of 0.067° and counting time per step 60.95 s.

2.5. Micro-Raman Spectroscopy

Micro-Raman spectra were recorded with a Renishaw Raman Invia spectrometer configured with a Leica DMLM microscope using Ar⁺ laser source ($\lambda=514.5\text{nm}$, $P_{\text{out}}=30\text{mW}$ considering the decrease

in power due to the plasma filter). In each measurement, the laser power was set by 10% of the source and the signal was accumulated by 4 individual spectra with an acquisition time of 10 s.

2.6. Inductively Coupled Plasma – Atomic Emission Spectroscopy

Inductively Coupled plasma atomic emission spectroscopy (ICP-AES) analyses were performed using an Agilent Technologies 4210MP-AES instrument. The Ag amount loaded on the electrocatalysts was calculated by the difference between Ag content in the solution before and after deposition. These solutions were diluted to fall within the range of the calibration curve (0 - 15 ppm), which was built starting from an Ag standard 1000 ppm in 5% HNO₃. The emissions at 328.1 nm for Ag and 324.7 nm for Cu were evaluated. Moreover, the analysis of the solutions after HMF electrolysis and Ag deposition was carried out to identify (but not quantify) Ag and Cu leached during electrochemical measurements.

2.7. X-Ray Photoelectron Spectroscopy

X-ray photoelectron spectroscopy (XPS) analysis was performed at the ISISS beamline of BESSY II in Berlin (Germany). In this facility, the photons are sourced from a bending magnet (D41) and a plane grating monochromator (PGM) yielding an energy range from 80 eV to 2000 eV (soft X-ray range), a flux of 6×10^{10} photons/s with 0.1 A ring current using a 111 μm slit and a 80 μm x 200 μm beamspot size. The spectra were fitted using CasaXPS software.

2.8. Electrical Resistivity Tomography

The probe for electrical resistance tomography (ERT) consists of sixteen circular measurement electrodes, made of stainless steel with diameter equal to 2 mm, set on a pipe with an inner diameter equal to 20 mm. The tested electrode was immersed in a solution of demineralized water and NaCl. The NaCl concentration was equal to 0.09 M. The local conductivity was measured with the ITS 2000 ERT instrumentation (Industrial Tomography Systems Ltd), connecting the electrodes to the Data Acquisition System (DAS) by coaxial cables. The measurements were based on the so-called circular adjacent strategy, in which electric current injected from adjacent electrodes pair at a time and the voltage difference is measured from the remaining pairs of electrodes. The procedure is repeated for all the independent pairs of electrodes. As for the reconstruction method for obtaining the conductivity maps from the electric potential measurements, the linearized (non-iterative) modified sensitivity back projection (MSBP) algorithm was selected, as implemented in the ITS System p2+V8 software. The local conductivity on the measurement plane was obtained on a mesh of 1 mm x 1 mm. The number of local measurements inside a circular tomogram, n , was equal to 316, thus. The

amplitude and the frequency of the injected current were set at 15 mA and 9600 Hz respectively, after preliminary calibration tests. For each set of acquisitions, 600 total instantaneous measurements were collected, at a frequency of 0.92 frames per second. In the following, the dimensionless local conductivity, X_i , that is computed as the ratio between the local conductivity, γ_i , measured with the tested electrode set between the measurement electrodes and a reference conductivity γ_i^{ref} , measured before the introduction of the tested electrode between the measurement electrodes will be analysed. Values greater than the unity mean that the conductivity of the medium has been increased because of the presence of the tested electrode. The tests were conducted at ambient conditions (25°C, 1 Atm).

3. Electrochemical valorisation of 5-(hydroxymethyl)furfural (HMF)

5-(hydroxymethyl)furfural, or HMF, is a versatile biomass-derived building block obtained from hydrolysis of hexose sugars (as glucose and fructose) and their derivatives polysaccharides (cellulose, hemicellulose, starch, inulin, etc.).⁵⁴ HMF is a member of the class of furans composed by a formyl group, directly attached to a furan ring at position 2, and a hydroxymethyl substituent (primary alcohol) at positions 5. Thanks to these peculiarities, HMF has a great potential to become a bio-based alternative to fossil-fuel-based platform molecules, through electrochemical oxidation, dehydration and hydrogenation, for the production of furanic derivatives and non-derivatives (Figure 3.1), with high potential in fuel, fine chemicals and polymer applications.^{21,55}

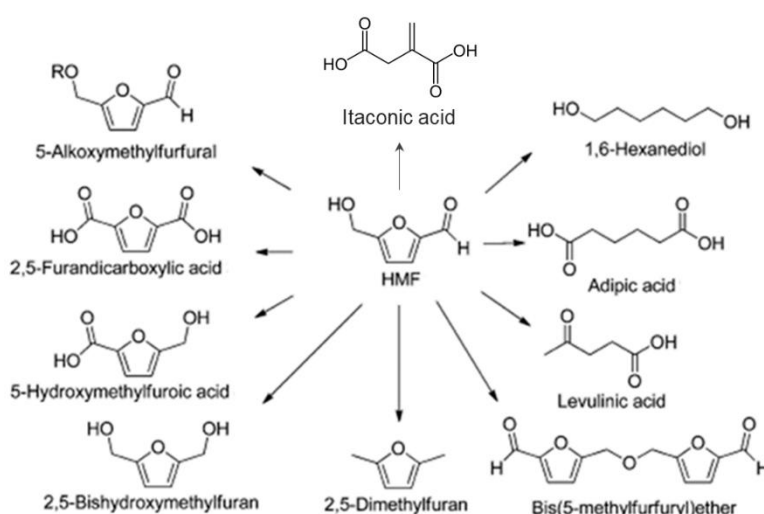


Figure 3.1. Commodity chemicals produced by HMF reductive or oxidative conversion.

3.1. Electrochemical oxidation

From the oxidation of formyl and/or hydroxyl groups, several value-added chemicals such as 5-hydroxymethyl-2-furan carboxylic acid (HMFCFA), 2-formyl-5-furan carboxylic acid (FFCA), 2,5-furan dicarboxylic acid (FDCA), 2,5-diformyl furan (DFF) can be obtained.^{21,32} However, the studies are mainly focused on FDCA synthesis,^{21,56} a monomer for the production of polyethylene furanoate (PEF), which is entirely obtainable from renewable raw materials and also possesses better thermal, mechanical and barrier properties compared to petroleum-based polyethylene terephthalate (PET).^{55,56}

Noble metal catalysts as Au, Pd, Pt and Pd–Au alloys are used for the electrochemical oxidation of HMF;^{21,32} Au is very efficient for the oxidation of the aldehyde group and it is more efficient than Pd.²¹ On Au/C catalysts, the major product is HMFCFA (98% selectivity) at potentials from 0.6 to 0.9 V vs RHE, a higher potential (1.2 V) is required for further hydroxyl oxidation to FFCA (5% selectivity) and FDCA (14% selectivity). With Pd/C catalysts a higher FDCA selectivity was

achieved, but the major products are FFCA (64%) at 0.6 V and HFCA (70%) at 0.9 V.³² Probably, the process follows two competitive pathways including DFF (at lower potentials) and HMFCFA (at higher potentials) as intermediates (Figure 3.2).³² The use of bimetallic catalysts resulted in FDCA formation at low potentials in comparison to monometallic catalysts. Pd–Au alloy nanoparticles supported on carbon black, showed the highest FDCA selectivity at 0.9 V (83%) after 1 h of reaction in alkaline medium and flow reactor, at 25°C.³² The product distribution depends on the electrode potential and Pd/Au ratio at the surface.²¹

Pt electrode in 0.3 M NaClO₄ + NaOH (pH 10) achieved a conversion of 70% of HMF and a DFF yield of 18%. Also a biphasic system (water–dichloromethane) can be used to extract the product from aqueous phase; a 100% DFF selectivity was obtained with a Pt anode.²¹

In addition, non-precious metals, as Ni, were used to significantly decrease the price of electrocatalysts. Nickel oxide hydroxide in 1 M NaOH, by applying a current density of 16 mA/cm², produced FDCA with 71% yield and 100% selectivity.³²

Therefore, DFF or FDCA can be selectively obtained from the electrochemical oxidation of HMF and the product is strongly dependent on the electrode employed. Pt is a suitable catalyst for oxidizing hydroxymethyl groups to aldehydes, instead Au is a good electrocatalyst for the oxidation of aldehyde to carboxylic acid. Pd and Ni are active for both hydroxymethyl and aldehyde oxidation, since the use of both metals yields significant amounts of FDCA, which have similar oxidation potentials for both groups. Moreover, not only the electrode but also the electrolyte and the pH have a strong influence on the reaction. Nevertheless, it must be considered that HMF is unstable at high pH (pH 13) and rapidly degrades into humin type products in the absence of catalyst.²¹

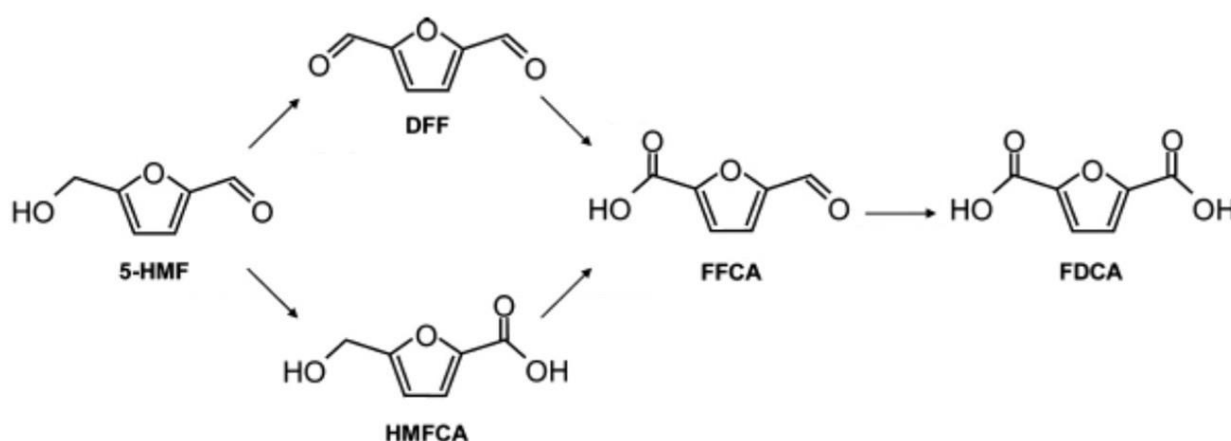


Figure 3.2. Proposed reaction pathways for HMF electro-oxidation to FDCA.

3.2. Electrochemical hydrogenation

Electrochemical hydrogenation (ECH) or reduction is an economical and sustainable route for the selective conversion of several raw materials in a wide range of chemicals and fuels, employing

hydrogen directly extracted from electrolytes (i.e. water, H^+ and OH^-), avoiding the requirement of a hydrogen gas supply.^{32,55} It also constitutes a path for the storage of renewable electric energy.

The reaction mechanism of ECH is analogous to heterogeneous thermo-catalytic hydrogenation, though the main difference concerns the adsorbed hydrogen species, which are electrochemically generated in situ, on the catalyst surface, by Volmer reaction through proton or water reduction. As a consequence, kinetic barriers for H_2 dissociation do not have to be overcome, facilitating hydrogenation process at mild condition.^{57,58}

The electrochemical conversion of benzaldehyde to benzyl alcohol is a model reaction used to investigate the influence of reaction conditions and catalyst on mechanism.^{59,60} The ECH of aldehyde group, in aqueous media, produce alcohols or alkyls by the hydrogenation of $C=O$ with two or four H_{ads} , respectively; nevertheless, the hydrogenation of the organic compound can also occur via a proton coupled electron transfer (PCET).^{58,60,61} This is an “outer-sphere” process and does not require strong interactions between reactants and the electrode surface.⁵⁸ The process involves a single electron/proton transfer between the carbonyl group and the catalyst, with the generation of a radical intermediate ($C\bullet-OH$), afterwards it can both dimerize, through $C-C$ coupling with a second radical, or can be further converted by another H^+/e^- pair, with the formation of the alcohol product.⁵⁸ The selectivity is largely determined by the relative overpotentials required to generate H_{ads} and $C\bullet-OH$.^{58,60}

The reactivity of the aldehydes is affected by the structure of the molecule. Sanyal et al. demonstrated that the presence of the aldehyde group in benzaldehyde forbids the η^6 adsorption on catalyst surface, compared to non-substituted benzene, due the steric hindrance of aldehyde groups that needed to form the coplanar η^6 adsorbed states, and, consequently, the hydrogenation of the aromatic ring was hindered. Similarly, investigating the electrocatalytic hydrogenation of benzaldehyde (aromatic aldehyde), acetophenone (aromatic ketone) and furfural (pseudoaromatic aldehyde), they found that the aromaticity plays an important role in the reactivity of the formyl group: in fact furfural exhibits lower reactivity than benzaldehyde and acetophenone while butyraldehyde (an aliphatic aldehyde) was unreactive under the same conditions.⁶⁰

Besides, the occurrence of the competitive HER decreases the efficiency of the process; therefore, catalysts with lower HER activity/selectivity are needed (i.e. increase the HER overpotential).^{32,55}

It is well known that the Pt group metals show a low overpotential for the HER, thus this process takes place simultaneously with ECH. Conversely, non-noble metals as Fe, Ni, Cu, Ag, Pb, etc. are good catalysts for ECH, thanks their medium/high HER overpotential.³²

3.2.1. Electrochemical hydrogenation of 5-hydroxymethylfurfural

The main HMF hydrogenation targets are 2,5-bis(hydroxymethyl)tetrahydrofuran (BHMTTHF), 2,5-dimethylfuran (DMF) and 2,5-bis(hydroxymethyl)furan (BHMF). BHMF and BHMTTHF find applications as building block in polymer synthesis and DMF and also BHMTTHF have a potential as transportation fuel.^{21,62,63} Particularly, BHMF is a promising and suitable building block for several polymer production (e.g. polyester, polyurethane foams, resins, etc.) but it is also an intermediate for the synthesis of fibers, drugs and crown ethers.^{63,64}

The electrocatalytic hydrogenation of HMF was investigated by Kwon et al. in neutral (0.1 M Na₂SO₄)⁶⁵ and acidic (0.5 M H₂SO₄)⁶⁶ media, on different metal electrodes.

In neutral conditions the electrodes can be distinguished as:

- Metals mainly hydrogenating the formyl group, forming 2,5-bis(hydroxymethyl)furan (BHMF) (Fe, Ni, Ag, Zn, Cd, and In);
- Metals forming BHMF and hydrogenolysis products, as 2,5-dimethylfuran (DMF), 5-methylfurfuryl alcohol (MFA), etc. depending on the applied potential (Pd, Al, Bi, and Pb);
- Metals forming mainly hydrogenolysis products (Co, Au, Cu, Sn, and Sb).

The presence of glucose in HMF solution enhances the formation of BHMF and suppresses the hydrogenolysis of HMF in 0.1 M Na₂SO₄ solution.⁶⁵

Whereas, in acidic solution the metal catalysts are divided in:²¹

- Metals mainly forming BHMF (Fe, Ni, Cu, and Pb);
- Metals forming BHMF and 2,5 dimethyl-2,3-dihydrofuran (DMDHF), depending on the applied potentials (Co, Ag, Au, Cd, Sb, and Bi)
- Metals forming mainly DMDHF (Pd, Pt, Al, Zn, In, and Sb).

Hence, depending on the pH the reaction pathways (Figure 3.3) and, consequently, the products generated follow hydrogenation or hydrogenolysis route, employing different metal-based electrocatalysts.³²

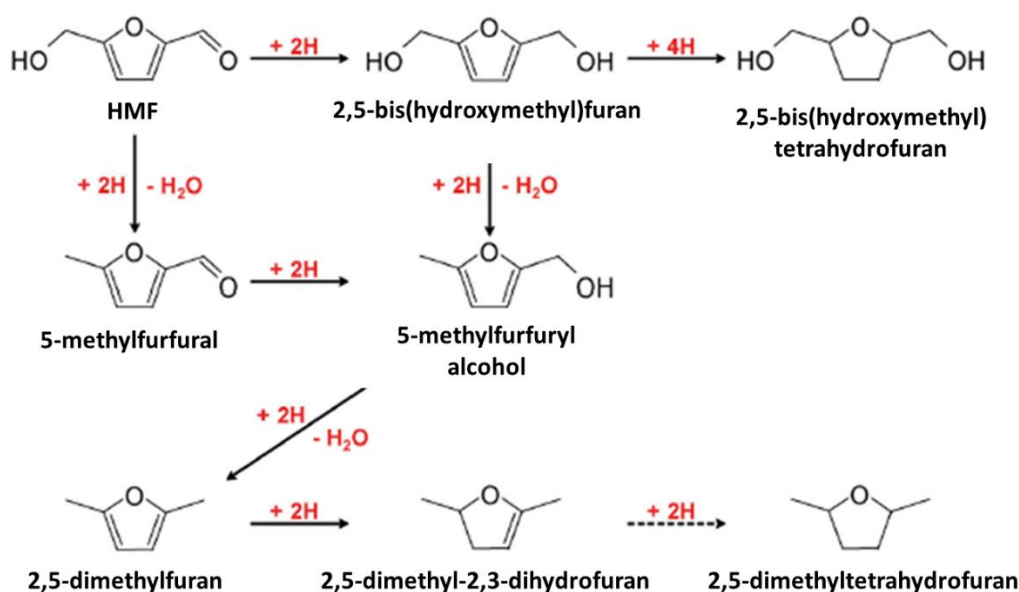


Figure 3.3. Proposed reaction mechanism for the electrochemical hydrogenation or hydrogenolysis of HMF. Adapted from “Electrocatalytic Conversion of Furanic Compounds”, Kwon et al. ACS Catal. 6, 6704–6717, 2016.

For instance, copper is known to drive HMF hydrogenation toward hydrogenolysis products. DMF is formed on a Cu foil electrode in 0.5 M H₂SO₄ solution with 35.8% selectivity,⁶⁷ however also a ZrO₂-doped graphite electrode in KNO₃ solution produces DMF with a 30.7% yield.⁶⁸ In these works, BHMF is an intermediate for DMF production.

A bimetallic CuNi electrode was recently proposed by Zhang et al. for the selective electrochemical reduction of HMF to DMF in acidic media (0.2 M sulphate buffer solution - pH 2.0 - containing 2 g L⁻¹ of HMF). This catalyst, in these conditions, promotes the hydrogenolysis reaction, obtaining 88% FE and 91.1% of DMF selectivity; yet, employing a pure Ni catalyst, BHMF resulted as the mainly product (selectivity >80%).⁶⁹

A Pd based catalyst, on Vanadium Nitride/Carbon fibers (Pd/VN/CF), has instead been proposed for the complete hydrogenation of the furanic ring, in a 0.2 M HClO₄ as electrolyte with HMF 0.01 M, forming 2,5-bis(hydroxymethyl)tetrahydrofuran (BHMTHF). High selectivity (≥88%) and high HMF conversion (≥90%) were achieved, with a faradaic efficiency ≥86%.⁶²

Another product, 2,5-hexanedione (HD), can be obtained from the opening of furanic ring. HD has application in alternative fuels and as precursor in the production of terephthalic acid. Roylance et al. obtained HD in a 0.2 M sulphate buffer solution (pH 2.0) containing 0.02 M HMF, at a constant potential of -1.2 V vs. Ag/AgCl, with a Zn electrode; they found that this catalyst conduct a one-step hydrogenolysis, Clemmensen reduction and ring opening reaction, achieving over 82% selectivity to HD product.⁷⁰

Moreover, the same group investigated the reduction of low concentrated HMF solutions to 2,5-bis(hydroxymethyl)furan (BHMF) in alkaline media, using a borate buffer as electrolyte (0.02 M HMF, 0.5 M borate buffer, pH 9.2), with an Ag/Cu flat electrode. Close to 100% faradaic efficiency and selectivity to BHMF was achieved at the optimal applied potential (-1.3 V vs Ag/AgCl). The lower FE and BHMF yield obtained increasing HMF concentration, from 20 to 100 mM, are mainly owing to a higher probability to form undesired side reaction products via dimerization or polymerization.⁶³

Electrode and catalyst design, and in particular the morphology of active phase, are crucial for avoiding undesirable reactions and achieving selective and efficient electrochemical conversion of aldehydes to targeted products.

For instance, in the above mentioned work of Roylance et al.⁶³ the performance of an Ag-based electrode deposited on Cu plates by either galvanic displacement or sputtering were compared. The results demonstrated that dendritic morphology obtained by galvanic displacement enhanced the activity, compared to sputtered electrode. Indeed, the nano-structuration of the catalyst, provided by dendrites, increased the surface area of flat support and probably enhanced the number of binding sites for HMF molecules, favouring the interfacial charge transfer processes.

Recently, on the basis of this work, Zhang et al.⁷¹ studied the role of Ag-Displaced Nanotextured Cu Catalysts on BHMF production. The best results were obtained after 2h of HMF electrolysis at -1.9 V vs Ag/AgCl in a 2 mL of 20 mM HMF in borate buffer (0.50 M, pH=9.2), with 98% of HMF conversion, 92% of BHMF selectivity and 58% FE. As also observed by Roylance⁶³, they conclude that nanostructuring largely increases the available surface area and therefore the productivity. Instead, Chadderon et al.⁵⁵ studied the activity of Ag nanoparticles on carbon black (Ag/C) catalyst, conducting the electrolysis in a sodium borate buffer (0.5 M – pH 9.2) with HMF 0.02 M, for 30 minutes. They demonstrated the higher activity of nanoparticles than bulk Ag; the carbon support material was also active for HMF reduction, but a strongly cathodic potential was required, leading to additional HMF hydrodimerization and low BHMF selectivity. Nevertheless, Ag/C catalyst showed high BHMF selectivity and FE (>95%) with the main by-product that is the dimer 5,5'-bis(hydroxymethyl)hydrofuroin (BHMHF – Figure 3.4).

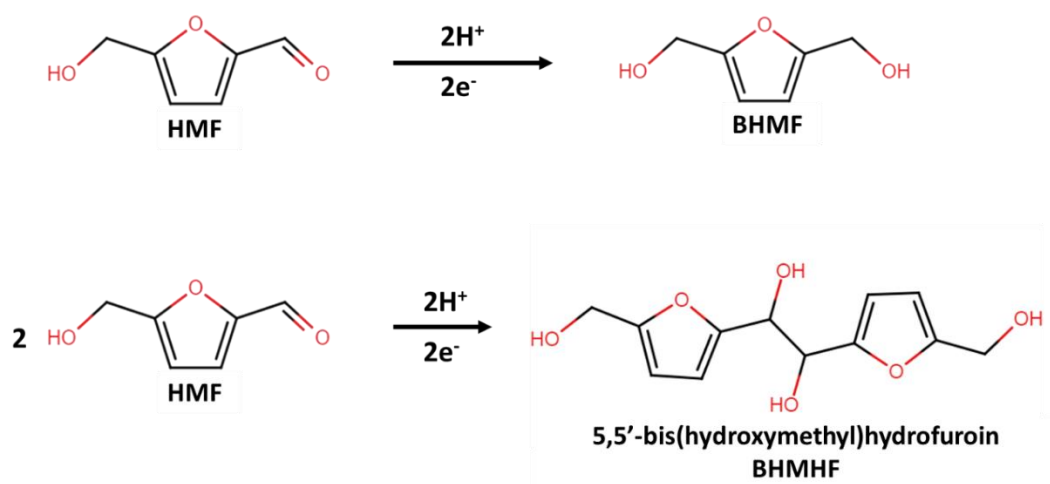


Figure 3.4. Electrochemical conversion of HMF: Route for the formation of BHMF (top) and 5,5'-bis(hydroxymethyl)hydrofuroin (bottom).

3.2.2. Ag nanostructured on Cu foams for the selective electrochemical hydrogenation of HMF to BHMF

Despite the advantages provided by nanostructuring on catalytic performances of Ag/Cu electrodes, the largest productivities reported in the literature, for the HMF electroreduction to BHMF, are still low for a real industrial application.^{63,71} Hence, it is advisable the design of new catalysts that combine the high surface per unit of volume provided by 3D supports, such as metal foams, with the benefits of active phase nanostructuring, developing an electrocatalyst with hierarchical porosity. Nevertheless, when foams are used as a support, the coating procedure for the deposition of the active phase plays a role of paramount importance to control the size, shape and distribution of the metallic particles.

In this way, galvanic displacement and electrodeposition are two simple methods to produce additive-free Ag particles with different shape on the surface of Cu foam.⁷¹⁻⁷³ The morphology of the particles largely depends on how far the formation conditions are from thermodynamic equilibrium.⁷³

In Galvanic displacement, the spontaneous precipitation of metal Ag and the simultaneous oxidation of Cu support was observed, following the reaction 3.1. It should be noted that the type of counter anion influences the growth rate of dendrites. For instance the presence of SO₄²⁻ anions accelerates the formation of Ag dendrites, compared with NO₃⁻.⁴⁵



In the electrodeposition method the precipitation of Ag particles is due to the application of a cathodic potential (3.2).



In both electrodeposition and galvanic displacement, it is possible to work under near- or far-equilibrium conditions by tuning the electrochemical parameters (deposition mode, potential applied) and the properties of the electrolyte (concentration and type of precursors)^{45,73} obtaining different shapes of particles. Crystals grown under equilibrium or quasi-equilibrium conditions generally have simple shapes with well-developed facets, which can achieve a minimum surface energy. When the condition depositions are far from equilibrium, the mass transfer play a key role in crystals growth, and it leads to the formation of irregular and complicated shapes (dendrites or branching formation).^{71,74}

Electrodeposition is largely used to produce Ag nanoparticles, but adjusting the cathodic potential applied and the deposition time also the growth of dendrites on Cu foam can be obtained.^{72,75}

3.3. Experimental section

3.3.1. Materials and chemicals

Cu and Ag commercial foam panels of 1.6 mm thickness and 450 μm cell size were supplied by Alantum. Cu foil (0.25 mm thickness, 99.98%) and Ag foil (0.127 mm thickness, 99.99%) were purchased from Sigma-Aldrich and Alfa Aesar, respectively.

The chemicals used were sodium hydroxide ($\geq 98\%$, Sigma-Aldrich), boric acid ($\geq 99.5\%$, Sigma-Aldrich), silver nitrate (99.9+%, Alfa Aesar), copper sulphate (0.9995, Sigma Aldrich) and 5-(hydroxymethyl)furfural (99%, AVA Biochem). 2,5-bis(hydroxymethyl)furan (Toronto Research Chemicals) was used as standard for High Performance Liquid Chromatography (HPLC) analysis. For the determination of Electroactive Surface Area (EASA), Lead Nitrate (99.5 %), Sodium Potassium Tartrate (99%) and Sulfuric acid (96%) were purchased from Sigma-Aldrich. All chemicals were used without further purification. Ultrapure water, UPW, (18 $\text{M}\Omega\cdot\text{cm}$) was used for the preparation of all aqueous solutions.

3.3.2. Synthesis of electrocatalysts

Foam electrodes were prepared by cutting Cu and Ag foam panels, of 1.6 mm thickness and 450 μm cell size, into 10 mm \times 10 mm pieces (geometric surface area 2.64 cm^2). Also Cu and Ag foils were cut into 10 mm \times 15 mm pieces, the actual exposed area is 10 mm \times 10 mm (geometric surface area 2 cm^2). Before the use, the electrodes were cleaned by washing with 2-propanol and ultrapure water, followed by immersing in 1 M HCl for 5 min to remove surface oxides, and water to remove residual HCl.

Ag/Cu electrodes were synthesized by electrodeposition (Ag/Cu ED) and galvanic displacement (Ag/Cu GD).

Ag electrodeposition on Cu foams or foils was performed in a single-compartment three-electrode cell controlled by a potentiostat/galvanostat Metrohm Autolab PGSTAT204, equipped with NOVA software. Foams or foils were the working electrodes (WE), while a saturated calomel electrode (SCE) and a Pt wire were the reference electrode (RE) and counter electrode (CE), respectively. The RE was placed close to surface of the WE, in the centre of the cell, and both were surrounded by the CE placed close to the walls of the cell. The electrodeposition was carried out by applying a 25 s pulse at -0.9 V vs SCE (-0.11 V vs RHE - Reversible Hydrogen Electrode), using 25 mL of 5.0 mM AgNO₃ aqueous solution electrolyte, under magnetic stirring of 500 rpm. After electrodeposition, the catalysts were rinsed gently with ethanol and water.

Ag galvanic displacement was performed by immersing Cu foams in a beaker containing 25 mL of 5.0 mM AgNO₃ aqueous solution, for 5 min. The foams were attached to a rotor and kept under mechanical stirring of 200 rpm. After synthesis, all the catalysts were rinsed gently with ethanol and water.

For comparison purposes, nanostructured Ag/Ag and Cu/Cu electrodes were synthesized by electrodeposition on Ag and Cu foam, respectively. Ag particles were electrodeposited on Ag foam by using a 5 mM AgNO₃ aqueous solution and applying a cathodic pulse of -1.1 V vs SCE (-0.44 V vs RHE) for 50 s. The electrodeposition of Cu particles was carried out in an electrolyte containing 0.024 M CuSO₄ and 0.08 M H₂SO₄ solution at -0.3 V vs SCE (0.006 V vs RHE) for 300 s.

3.3.3. Electrochemical measurements

All electrochemical experiments were controlled by a potentiostat/galvanostat Metrohm Autolab PGSTAT204, equipped with NOVA software; Cu or Pt wires were attached to the electrodes to enable connection to the potentiostat.

A three-electrode three-compartment cell, separated by glass frits, was used to perform the measurements. Working electrodes were bare and coated foils and foams, placed in the central compartment. Counter electrodes were Pt wires placed in the side compartments. A saturated calomel electrode (SCE) was used as reference electrode. The RE was kept in electrolytic contact with the main compartment via a Luggin capillary.

All potentials were reported vs SCE and RHE ($V \text{ vs RHE} = V \text{ vs SCE} + 0.244 \text{ V} + 0.0591\text{pH}$). The cell was immersed in a thermostated water bath at 25°C. The iR drop (ohmic drop), determined by current interrupt approach, for all the Linear Sweep Voltammeteries (LSVs) was compensated after

measurements, assuming a constant R_u (Uncompensated Resistance) during the scans; instead the constant-potential electrolysis were performed without compensation.

Catholytes were 25 mL of 0.5 M borate buffer aqueous solution (pH 9.2) with and without HMF at different concentrations as 0.02, 0.05, 0.10 and 0.50 M. In the counter electrode compartments the anolyte was a borate buffer with 0.5 M sodium sulphite, to prevent the drift of the anode potential.⁶³ To avoid the presence of dissolved oxygen, all the solutions were purged with N_2 before each electrochemical experiment, and a N_2 flow was kept in the open space of the cell during experiments. The LSVs were recorded for the electrochemical characterization of the catalysts. The potential was scanned from 0 to -1.4 V vs SCE (from 0.79 to -0.61 vs RHE) with a scan rate of 1 mV s^{-1} in borate buffer or at 5 mV s^{-1} in borate + HMF. The slowest scan rate in the LSV without HMF was chosen to ensure the reduction of the electrocatalyst.

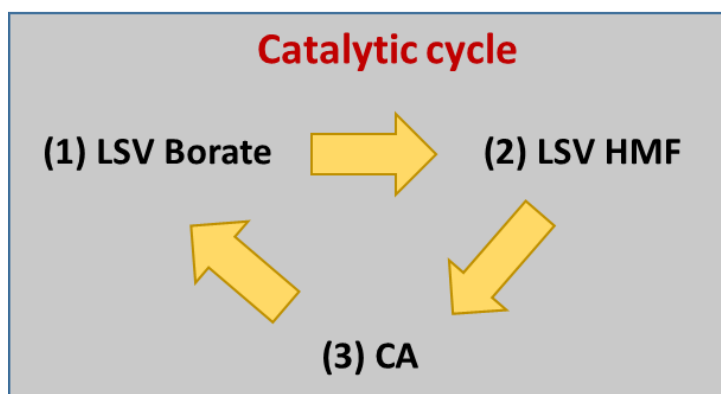
The electroactive surface area (EASA) was estimated using lead underpotential deposition (UPD), comparing the results with the response of polished Ag foil.

A 10 mm \times 10 mm Ag foil was abraded with emery paper of 300, 600, 800, 1200, 2500 grit and finally polished with 50 nm colloidal silica, then the material was rinsed with water and acetone. The measurements of EASA were performed recording a cyclic-voltammetry (CV) in the single compartment three-electrode cell described in section 3.3.2. Cyclic voltammograms (CVs) were recorded between 0 and -0.6 V vs SCE (from 0.79 to 0.19 vs RHE), with a scan rate of 50 mV s^{-1} . The electrolyte was an aqueous solution of 0.10 M sodium potassium tartrate containing 0.01 M H_2SO_4 and 3×10^{-4} M $Pb(NO_3)_2$.

Electrocatalytic hydrogenations were performed potentiostatically at -1.3 V vs SCE (-0.51 V vs RHE) using deaerated electrolytes with different HMF concentrations (0.02, 0.05, 0.10 and 0.50 M) and flushing N_2 in the overhead of the working electrode compartment. The experiments were performed under stirring of the solution with a magnetic bar at a rotating speed of 1000 rpm.

The catalytic cycle is composed by a sequence of LSVs without and with HMF, electrolysis at constant potential and then the first two LSVs are repeated. The LSVs before the HMF electroreduction were performed to assure the reduction of any surface oxide species and therefore to minimize Faradaic loss during the process; conversely, after the catalytic test, they allow to check for any change in the electrocatalysts after reaction. Once the first cycle was completed a new electrolysis could be immediately performed, starting a new catalytic cycle (Scheme 3.1). This sequence was replicated for all investigated HMF concentrations.

The reactions were carried out under total HMF conversion conditions, which were obtained through the transfer of the charge necessary to convert all HMF in solution into BHMF (i.e. through a 2 e-process) assuming a 100 % Faradaic Efficiency. At the end, the solutions were collected and analysed with HPLC. All the measurements were performed in three replicates. The geometric surface areas of the electrodes were considered for calculating current densities.



Scheme 3.1. Description of the catalytic cycle: after the synthesis the catalyst undergoes an LSV in borate buffer (1), followed by an LSV in borate+HMF (2) and a chronoamperometry (CA) (3) in HMF solution. After the CA, the first two LSV are repeated, afterwards the cycle can stop or start again with another electrolysis.

Electrochemical impedance spectroscopy (EIS) was measured in the same three-electrode three compartments cell with a Biologic VSP-300 multichannel bi-potentiostat. EIS experiments were performed in a borate plus HMF 0.05M solution from 100 kHz to 100 mHz with amplitude of 20 mV, at fixed -1.1 V vs SCE (-0.31 V vs RHE) potential.

3.3.4. Products Analyses

Quantitative analysis of the products in the electrolytes was conducted by means of a HPLC Agilent 1260 Infinity Series, provided with Cortecs T3 2.4 μm ($4.6 \times 100\text{mm}$), operating at 30°C , equipped with an autosampler (injection volume 1 μL) and a Diode-Array Detector set at 284 nm for the identification of HMF and 223 nm for the identification of BHMF. The analyses were performed with gradient elution in three steps: isocratic conditions for 6 minutes, with eluent composed of $\text{CH}_3\text{CN}/\text{H}_2\text{O}$ 10/90 v/v ratio; gradient elution for 5 minutes until a $\text{CH}_3\text{CN}/\text{H}_2\text{O}$ 50/50 elution ratio was obtained; gradient elution for 4 minutes until a $\text{CH}_3\text{CN}/\text{H}_2\text{O}$ 70/30 elution ratio was obtained. The flow rate was 0.7 mL min^{-1} . Conversion, selectivity, faradaic efficiency (FE) and BHMF productivity were calculated with the following equations (3.3 – 3.6):

$$\chi_{\text{HMF}}(\%) = \frac{\text{mol}_{\text{HMF consumed}}}{\text{mol}_{\text{HMF initial}}} \times 100 \quad (3.3)$$

$$S_{\text{BHMF}}(\%) = \frac{\text{mol}_{\text{BHMF formed}}}{\text{mol}_{\text{HMF consumed}}} \times 100 \quad (3.4)$$

$$FE (\%) = \frac{mol_{BHMF \text{ formed}}}{\frac{charge \text{ passed}}{F \times 2}} \times 100 \quad (3.5)$$

where F is the Faraday constant.

$$BHMF \text{ productivity} = \frac{mol_{BHMF \text{ formed}}}{reaction \text{ time (h)} * area (cm^2)} \quad (3.6)$$

The area corresponds to the geometric area of electrodes, 2.64 cm².

The identification of some by-products was performed by Gas Chromatography-mass spectrometry (GC-MS) and electrospray ionization mass spectrometry (ESI-MS). The GC-MS was an Agilent 6890 N series instrument coupled with a mass spectrometer Agilent technologies 5973 Inert, with manual injection, and with a capillary column Agilent HP5, composed by (5 %-Phenyl)-methylpolysiloxane. The identification of the products was made via MSD Chemstation software including the standard NIST database.

The ESI-MS instrument was a Waters micromass ZQ 4000, with manual injection.

For GC-MS and ESI-MS analyses an amount of the reaction solution was extracted for three times with acetonitrile. Then both the aqueous and organic phases were analysed.

3.4. The role of three-dimensional support and nanostructuring of AgCu bimetallic particles

3.4.1. Characterization of Ag/Cu foams and foils electrocatalysts

SEM images of Ag and Cu bare foams are shown in Figure 3.5. The foams are made by interconnected struts of about 50 μm diameter, with a cell dimension of 450 μm (Figure 3.5a, b). In the enlargement in Figure 3.5a1 the smooth surface of Cu foams can be observed, but cubic particles are also present in some regions (inset). The Ag foam exhibits a surface composed by a packed polyhedral-like structure, which provides a high roughness (Figure 3.5b1). Finally, Ag and Cu bare foils counterparts showed rough surfaces caused by the presence of some stripes, probably due to their manufacturing by rolling (Figure 3.5c, d).

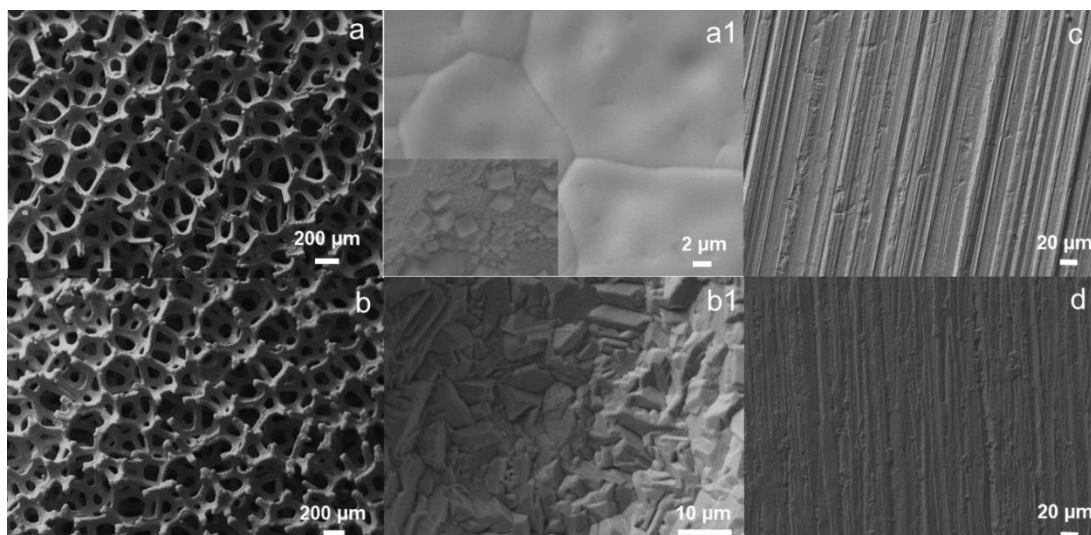


Figure 3.5. SEM images of: Cu (a, a1) and Ag (b, b1) bare foams; Cu (c) and Ag (d) bare foils.

As discussed in chapter 3.2.2, the morphology of deposited particles is influenced by the proximity (or not) to thermodynamic equilibrium.⁷³ For Ag/Cu ED sample, the stirring of the electrolyte during electrodeposition promotes the replenishment of the fresh solution in the electrode-electrolyte interface, increasing the mass transfer and the deposition condition is under thermodynamic control at the short deposition times. In Figure 3.6. SEM and FE-SEM images show that after electrodeposition, the Cu surface results homogeneously covered by an Ag film, made by arrays of particles (Figure 3.6a) that cover not only the Cu surface but also the inner part of the foam (Figure 3.6c). High resolution FE-SEM images (Figure 3.6a1) reveal that the coating is made by ill-defined 50-200 nm particles, well faceted two-dimensional nanoplates, and some three-dimensional octahedral particles (20-50 nm).

Some Ag dendrites are only detected in the edges of some struts (more exposed sites of the foam), where the electrodeposition may be faster and limited by mass-transfer, conditions prone to dendritic particle growth at the applied potential. The length of the dendrites and size of the branches are in the 2 to 7 μm and 500 to 1000 nm range, respectively (Figure 3.6b, b1, b2).

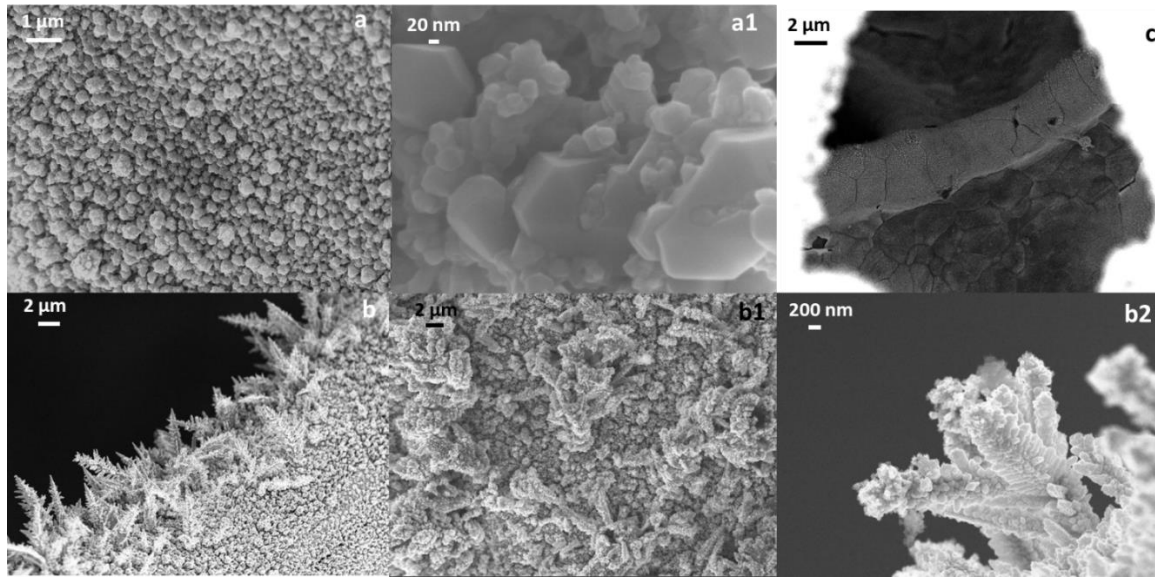


Figure 3.6. FE-SEM images of the Ag/Cu ED sample showing the deposition of agglomerates of nanoparticles (a, a1) and dendrites (b, b1, b2). Detail of the inner part of the coated foam (c).

In galvanic displacement the Ag deposition is mainly governed by mass transfer, consequently Ag/Cu GD sample shows the growth of large and highly branched dendrite structures, with overall length from 10 to 40 μm . This preferentially happens on the edges of the pores, partially blocking them (Fig. 3.7a). The dendrites (Fig. 3.7b) are composed by hexagonal and ill-shaped particles of ca. 120 - 200 nm and 50 - 100 nm respectively, while more rounded particles, less than 50 nm, are in the top of the branches (Fig. 3.7c). The growth of aggregates of hexagonal nanoparticles begins in perpendicular direction to the surface of the foam, later the branching occurs since each corner of a crystal formed is able to promote the growth of a branch⁷⁴ (Fig. 3.7c-inset). The morphology of these dendritic frameworks are similar than those obtained in the work by Roylance et al. on a Cu foil.⁶³ Though the surface is largely covered by dendrites, the inner parts of surface, far from the pores, are covered by a homogeneous layer formed by hexagonal, ca. 100-350 nm, and smaller ill-defined particles (Fig. 3.7d-f).

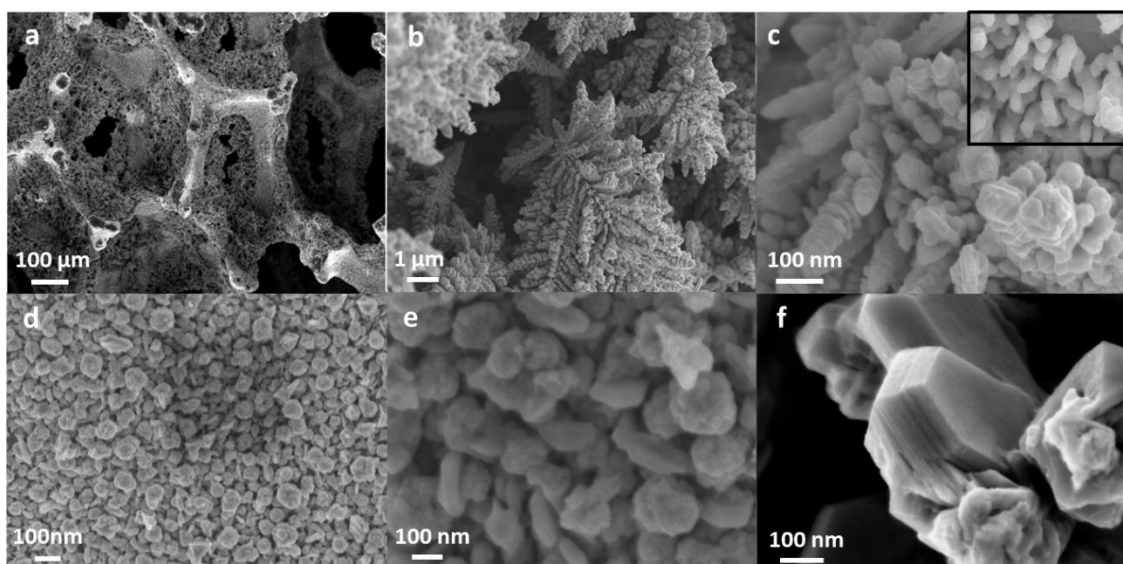


Figure 3.7. FE-SEM images of the Ag/Cu GD sample showing pores blocked or partially blocked (a), dendrites (b and c), and aggregates of nanoparticles at different magnifications (d, e, f).

With the aim to compare the performances of 2D and 3D electrodeposited catalysts, a Cu foil was also coated by Ag, using the same electrodeposition parameters and conditions previously employed for Cu foam.

The deposition on Cu foil leads to the development of an Ag film thicker and less homogeneous than those formed for the foam (Figure 3.8a, b), with the formation of aggregates of spherical, needle-like and dendrite Ag particles (Figure 3.8b, c). The different morphology and shape of particles observed on foil than on foam can be due to the different shape of the support, which may modify the properties of the coating.

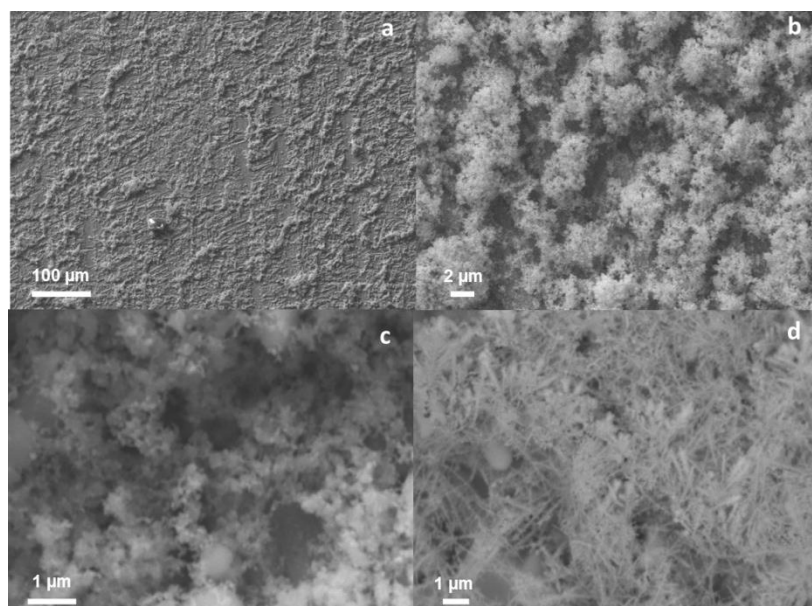


Figure 3.8. SEM images of the Ag/Cu ED foil at different magnification (a, b, c, d).

Finally, in order to distinguish the effect of the nanostructuring of the foam surface from the effect of the deposition of Ag on Cu foam, on catalytic activity, the electrodeposition of Ag particle on Ag foam and Cu particle on Cu foam was carried out. SEM images in figure 3.9 show a rather homogeneous coating for Cu/Cu foams, with irregular polyhedral Cu particles dispersed on surface and some ill-defined dendrites structure on the edges of the pores (Figure 3.9a, a1). Instead, the Ag/Ag sample has a less homogenous coating, with the formation of ill-defined agglomerated particles dispersed on surface and needle-shaped dendrites growing on the struts (Figure 3.9b, b1).

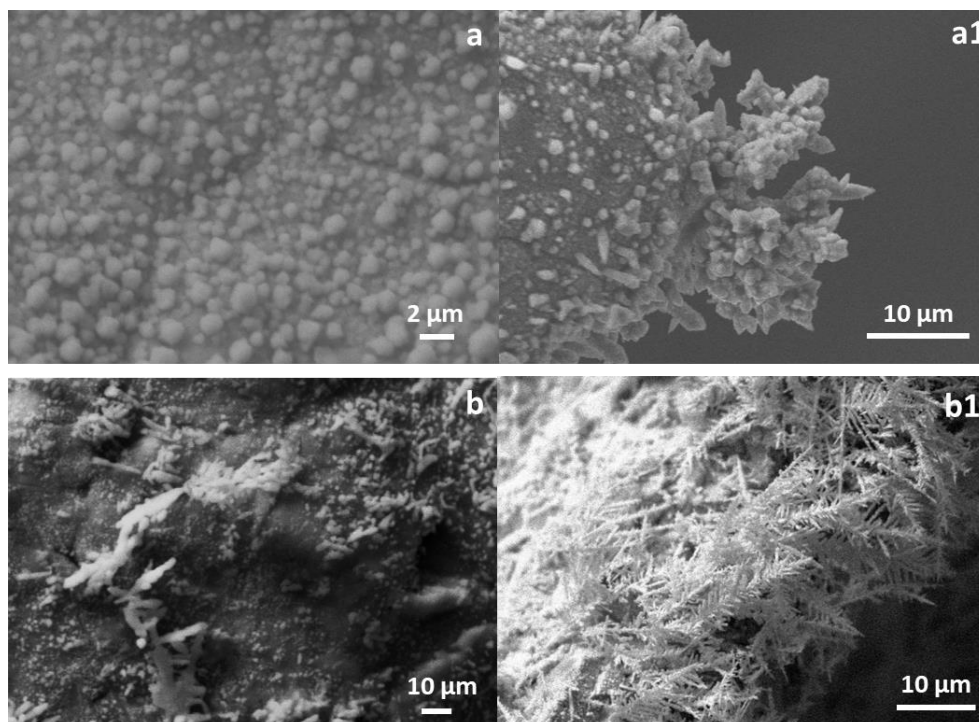


Figure 3.9. SEM images of nanostructured Cu/Cu (a, a1) and Ag/Ag (b, b1) electrocatalysts.

XRD analyses (Figure 3.10a) suggest that the cubic particles observed on Cu foam surface (Figure 3.5a1-inset) are Cu_2O . Micro-Raman spectra (Figure 3.10b) confirm this hypothesis showing the bands of Cu_2O ($145, 215, 421, 528$ and 619 cm^{-1}), also observed for Cu foil (not shown), which could be formed because of exposure to air of the material. Moreover, the band at 118 cm^{-1} suggests the presence of a defective Cu_2O phase; it is related to the Γ_{12}^- forbidden mode, active only in presence of defects in Cu_2O .^{76,77} No oxidised species are shown on Ag foam and foil, indeed only cubic Ag^0 reflections are observed by XRD.

Low intense cubic Ag^0 reflections are displayed from XRD patterns of Ag/Cu foams (Figure 3.10a), which grow preferentially in the (111) direction; nevertheless, considering the ratio between the intensity of the (111) and (220) planes, some differences are observed. Indeed, Ag/Cu GD showed a higher ratio, $I_{(111)}/I_{(220)} = 6$, than Ag/Cu ED, which has $I_{(111)}/I_{(220)} = 3$. This behaviour can be due to the larger Ag loading (3-5 times greater) and the formation of dendrites on GD catalyst. Since the

diffraction patterns did not show any peak shift or modification compared to pure metals, we can conclude that pure Cu and Ag atoms were not alloyed but mixed in the Cu-Ag films/particles. Note that the reflections related to Ag are not visible for Ag/Cu foil sample, in Figure 3.10c, probably due to the very low thickness of Ag coating.

Along with these peaks, Cu^0 and Cu_2O reflections from the support are recorded for both electrodeposited and galvanic displace samples. As above discussed for the Cu foam, we can attribute the formation of these oxidised species, also evidenced in Raman spectra, to the exposure of the catalyst to the air. Nevertheless, in these cases, also the deposition conditions can lead to the oxidation of the support. Indeed, the potential applied during electrodeposition generates a basic media close to the foam, in the electrode/electrolyte interface, due the reduction of nitrates and water, which provokes the Cu foam oxidation. Whereas, in galvanic displacement the Cu^0 is spontaneously oxidised to Cu ions (Cu^{2+} or Cu^+), while Ag^+ from solution is reduced to Ag^0 and deposited on Cu surface.⁷⁸ In both cases, the existence of copper ions dissolved in solution after deposition is revealed by ICP analysis.

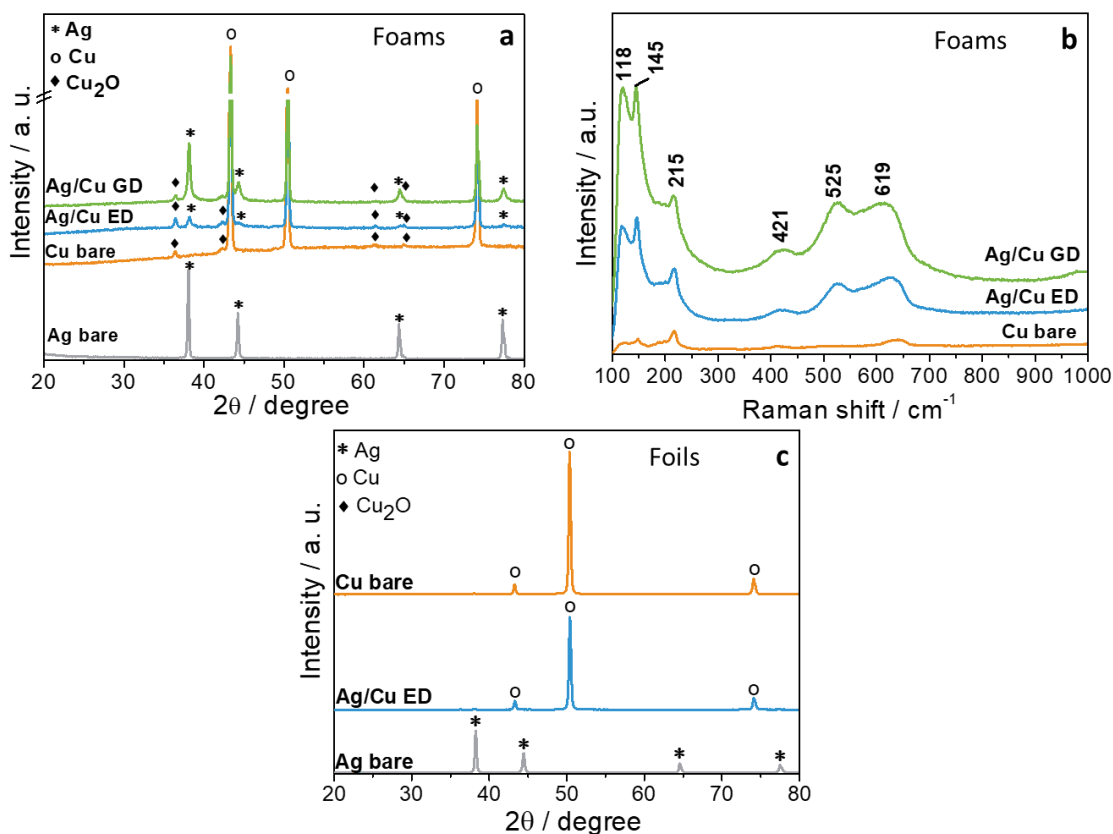


Figure 3.10. XRD patterns (a) and Micro-Raman spectra (b) of fresh Ag, Cu, Ag/Cu ED and Ag/Cu GD foams; XRD patterns of Ag, Cu and Ag/Cu ED foils (c).

To evaluate the distribution of Ag and Cu on the foam surface and to estimate the composition of particles deposited, a preliminary study using EDS elemental maps was performed for GD and ED samples.

It was possible to acquire EDS elemental maps for dendrites “isolated” from the support, namely, dendrites growing in a direction that allows to eliminate (or limit) the influence of the support on the Cu signal (Figure 3.11a, b). The maps indicate the coexistence of well dispersed Ag and Cu elements for both Ag/Cu GD (Figure 3.11a1, a2) and Ag/Cu ED (Figure 3.11b1, b2) samples, however from XRD analyses showed above we can exclude the formation of an AgCu alloy. Nevertheless, to confirm this hypothesis more in-depth analyses were needed.

Therefore, the coatings were detached from the foam supports and analysed by HRTEM, to further investigate and explain the morphology and composition of the particles deposited on surface.

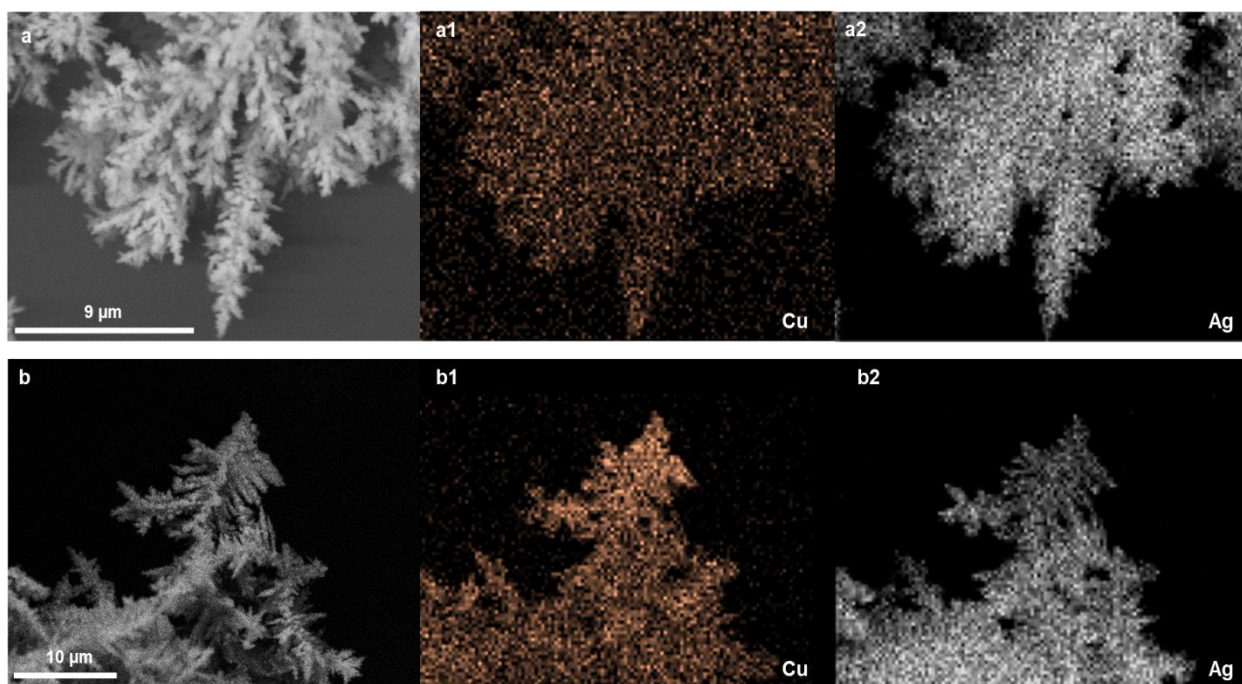


Figure 3.11. SEM images of dendrites: Ag/Cu GD sample (a) with Cu (a1) and Ag (a2) EDS elemental maps; Ag/Cu ED sample (b) with Cu (b1) and Ag (b2) EDS elemental maps.

The images confirm that the dendrites in both electrodeposited and displaced samples are composed by interconnected and stacked particles, containing both Ag and Cu. It should be noted that the Ag/Cu atomic ratio estimated from EDS analyses is rather constant and it is around 84-85/16-15 (Figure 3.12a, b), similar to those already reported for AgCu bimetallic catalysts prepared by electrodeposition,⁷⁵ galvanic displacement⁷¹ or by melting in a microwave inductive furnace.⁷⁹

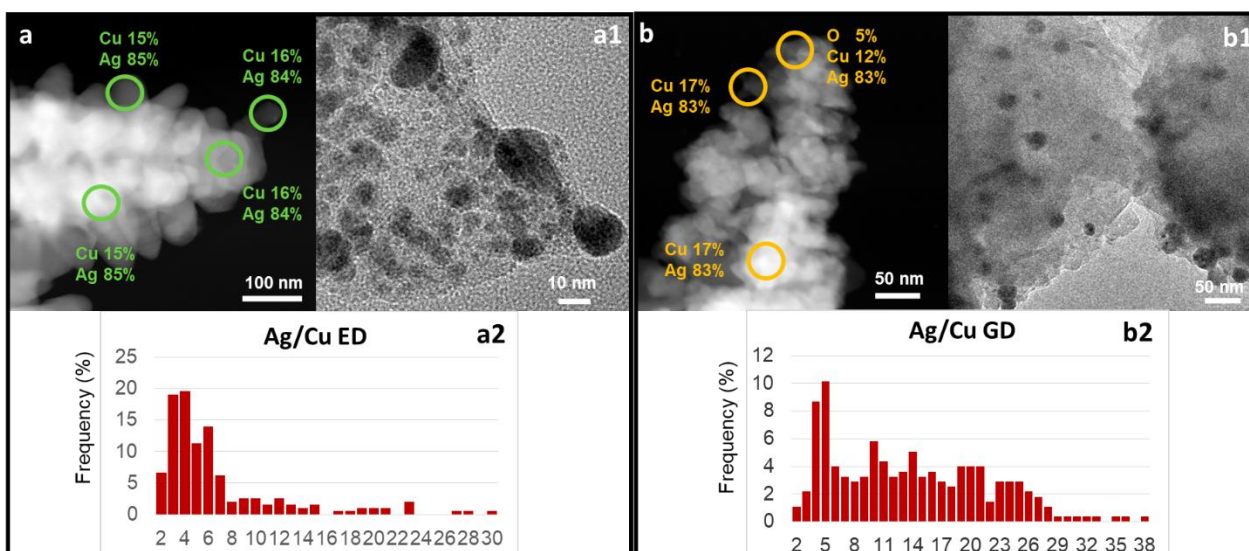


Figure 3.12. TEM characterization of Ag/Cu fresh ED (a, a1, a2) and GD (b, b1, b2) foams: HAADF/STEM images of a dendrite with EDS data in the regions (a, b), HRTEM images of the arrays of particles coating (a1, b1) with particle size distribution of nanoparticles in the histogram (a2, b2).

The HRTEM and HAADF/STEM images showed the ill-defined and large arrays of particles already observed by FE-SEM, nevertheless the coatings, detached from the flat zones, also unveil the presence of well dispersed small nanoparticles. Note that both electrodeposited and galvanic displaced samples show similar types of particles, grown in the range of 2 – 30 nm, however the distribution in figure 3.12a2 and b2 reveals that ED sample developed smaller particles, with the 75% between 2 – 7 nm, conversely ED sample has a larger distribution between 2 and 30 nm.

From the EDS analyses of a scratched zone, in figure 3.13a and b, it can be observed that the Ag particles, developed on both Ag/Cu electrodes, can be supported on a Cu metallic or oxidised support. In any case, despite the influence of Cu support, the Ag/Cu ratio observed is similar to that above found in the dendrites; this is confirmed by the EDS analysis of a not-supported particle in the electrodeposited catalyst that also proves the formation of AgCu bimetallic particles (Fig. 3.13c).

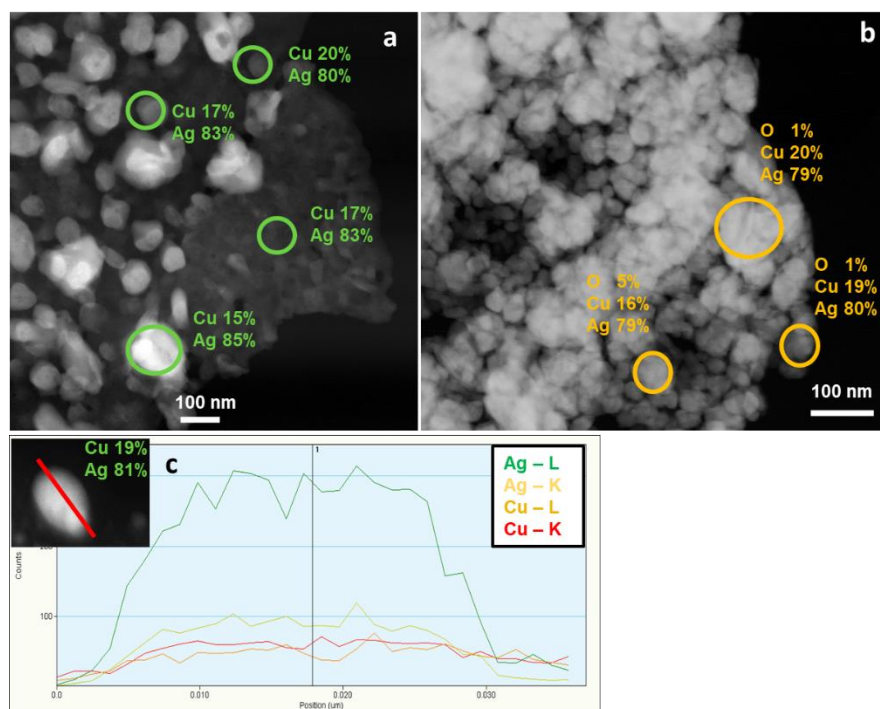


Figure 3.13. HAADF/STEM images of the arrays of particles for Ag/Cu ED (a) and Ag/Cu GD (b) samples with EDS data. HAADF/STEM image of an Ag/Cu unsupported particle, with the elemental composition along a line (c) for Ag/Cu ED.

The results obtained from XPS measurements (Figure 3.14) confirm and reinforce the information obtained from XRD and Raman analyses. Ag particles are present in the metallic phase, whereas Cu is present on the electrode surface both as a metallic and as oxidised species. The Cu 2p and Ag 3d spectra of both electrocatalysts, reveal some differences on the surface composition depending on the preparation method. The surface of the electrodeposited sample is enriched in Cu (Figure 3.14a, a1), meanwhile the displaced sample is Ag enriched (Figure 3.14b, b1), as expected considering the large difference of Ag amount deposited on GD sample (4-5 times greater) compared to ED sample.

The valence band measurements reveal that the Ag 4d and Cu 3d components for both Ag/Cu ED (Figure 3.14a2) and GD (Figure 3.14b2) samples can be fitted by a linear combination of their principal components (Ag and Cu reference samples) indicating that there is no alloy formation, i.e. lack of charge transfer between both components or distortion in the spectrum shape.

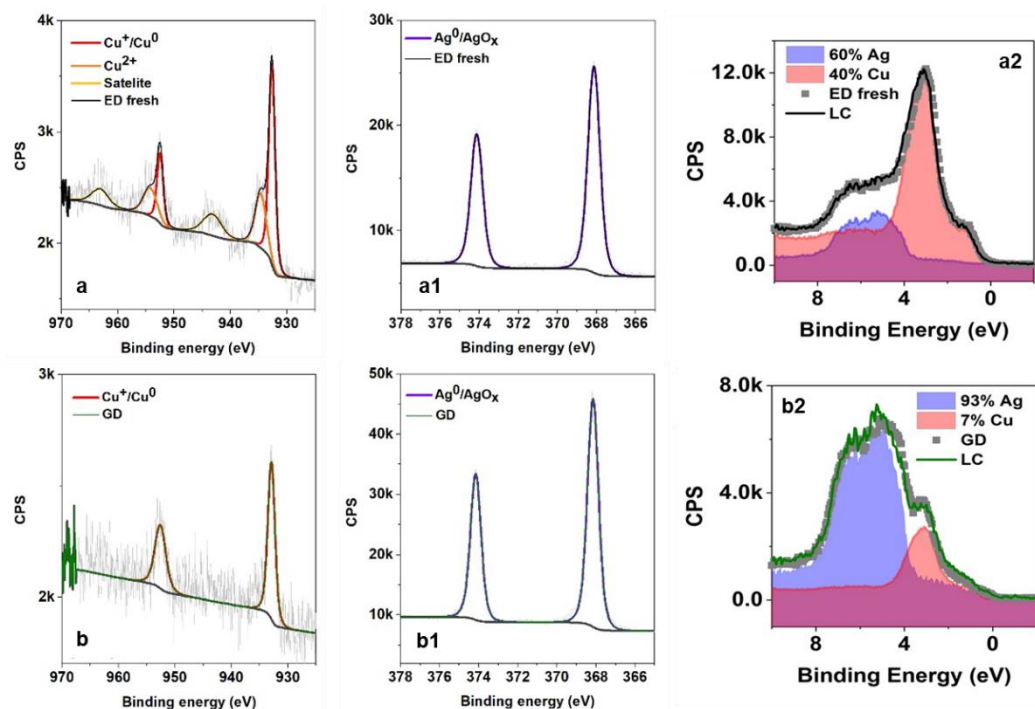


Figure 3.14. Cu 2p and Ag 3d spectra of the Ag/Cu ED fresh (a, a1) and Ag/Cu GD fresh (b, b1) foams. Valence band measurements of the Cu 3d and Ag 4d of the fresh Ag/Cu ED (a2) and Ag/Cu GD sample (b2).

Lastly, the electrical resistivity of the Ag/Cu foams electrodes was investigated to evaluate the contribution of deposition method on this parameter, which can affect the performances of the electrodes. The electrical resistivity of pure metallic Ag and Cu is very low (1.6 and 1.68 $\mu\Omega$ cm at 20°C,⁸⁰ respectively), but their combination may modify the resulting resistivity compared to pure metals⁸¹. It is well-known that the incorporated Ag atoms act as a scattering source against electron passage and surface roughness increases electrical resistivity of thin films.⁸¹ Hence, the morphology of AgCu particles, the interconnected areas among the bimetallic particles and the contact resistance between the particles and the substrate can also lead to an increase in electrical resistance.

Electrical Resistivity Tomography (ERT) experiments were performed to examine and clarify these aspects, obtaining a dimensionless mean conductivity values.⁸² The experiments were performed by adjusting the conductivity of the water solution where the electrode was immersed, so that the conductivity inside the probe did not vary significantly, returning a mean value of the dimensionless conductivity close to 1.

The measures with Ag bare and Ag/Cu ED foams supplied a dimensionless conductivity equal to 1.85 and 1.41, respectively. This confirms the higher conductivity of Ag in comparison to Cu and that Ag particles deposition on Cu foam enhances the conductivity of the bare electrode. The increment is, however, lower than that estimated using the Ag/Cu atomic ratio, probably because of the presence

of a tiny interconnected area, between the AgCu particles and the substrate that induces the presence of a non-negligible electrical resistance.

At the end of this series of characterizations analyses, it is possible to give an overview of the morphology and the composition of Ag/Cu ED and GD electrocatalysts. Hence, regardless of the preparation method, the catalysts could be described as a Cu metallic foam coated in some regions by a Cu₂O film, and wherein bimetallic AgCu particles are deposited and strongly stabilized as a homogenous layer, which is Cu- or Ag-enriched in the electrodeposited or displaced catalysts, respectively, depending on the amount of Ag deposited. As demonstrated by ERT measurements, and also confirmed by EIS data reported below (chapter 3.3.2), this configuration enhances the electron transfer between the support and the active species and may explain the stability of the film during the electrocatalytic tests.

The deposition method affects the average dimension of agglomerates formed, particularly, galvanic displacement leads to the formation of dendrites and bigger particles, with a large distribution of dimension. Nevertheless, this does not influence the composition of AgCu particles, wherein Cu and Ag are well distributed, but not alloyed, and where the Ag/Cu ratio is rather constant around a well-determined value, for both ED and GD electrocatalysts.

The formation of the bimetallic particles occurs as a side reaction during Ag deposition by both preparation procedures. The dissolution of Cu as Cu²⁺ or Cu⁺ during the electrodeposition or galvanic displacement and their reprecipitation with Ag, could explain the formation of AgCu bimetallic catalysts. The reprecipitation of copper for electrodeposited samples is fostered by the cathodic reduction potential, while an explanation to this behavior for displaced samples is not clear yet. Note that in a previous work, it was shown that Cu electrodeposited as Cu⁺, this may also explain the presence of Cu₂O on the ED catalysts.⁸³

3.4.2. Electrochemical Characterization

The electroactive surface area (EASA) of foam and foil electrocatalysts is estimated by Pb underpotential deposition (Pb-UPD). The procedure consists on the selective deposition of a full monolayer of Pb on Ag or Cu surface, the charge associated to the deposition/dissolution of the Pb monolayer is directly proportional to the substrate surface area and can be evaluated by estimating the Pb-UPD for a polished foil with known geometric area (Figure 3.15).⁸⁴

The values of EASA, summarized in Table 3.1, show that the electroactive surface exposed to the electrolyte is three-fold larger for Ag/Cu than Ag regardless of the shape of the electrode, foam or foil. The use of a 3D support for Ag deposition also provides a three-fold EASA increase, in comparison to the foil counterpart, i.e. ~80 vs 23 cm² for the Ag/Cu foam and foil respectively.

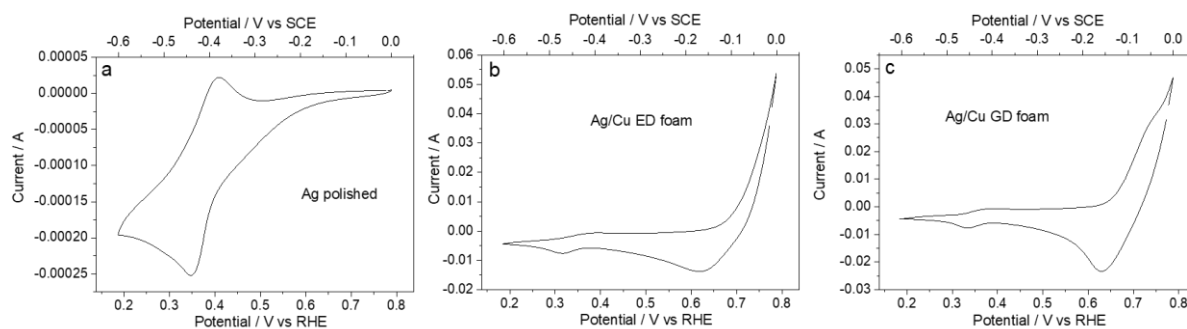


Figure 3.15. CVs recorded during Pb-UPD on Ag polished foil (a), Ag/Cu ED foam (b) and Ag/Cu GD foam (c).

The EASA of Ag/Cu displaced and electrodeposited samples is very close (81 and 79 cm², respectively) and higher than those of the Cu and Ag bare foams. Note that both Ag and Cu are active in Pb-UPD for Ag/Cu samples and it is not possible to distinguish their individual contributions,⁸⁴ indeed a surface area of 15 cm² was obtained for the Cu foam and 8 cm² for Cu foil, a value similar than for Ag foil. However, if the EASA is referred to the mass of Ag loaded, measured through ICP analysis, the obtained values, i.e. 79 and 18 cm²/mg_{Ag} for ED and GD fresh samples, respectively, clearly evidence that a lower amount of Ag is available for the electrochemical reaction in dendrites than in nanoparticles. The larger particle size in the displaced sample may explain the differences. However, it should be noted that UPD on Ag may have some limits that can affect the measurements, avoiding to give absolute surface area values. For instance, it has been reported that different catalysts may behave somewhat differently during Pb-UPD and thus the appropriate potential range should be selected; moreover, it has been claimed that the underpotential deposition of Pb does not take place on Ag nanoparticles smaller than ca. 50 nm.^{85,86}

As regards Ag/Ag and Cu/Cu samples, the nanostructuring has a positive impact and increases the EASA of the bare foams, although the increase is not as high as that obtained for Ag/Cu foams (~1.2 times for Ag/Ag, ~1.6 times for Cu/Cu and ~5.3 times for Ag/Cu).

Table 3.1. Electroactive surface area (EASA) values obtained by Pb UPD for foams and foils electrocatalysts.

EASA / cm ²	Cu bare	Ag bare	Ag/Cu ED	Ag/Cu GD	Cu/Cu	Ag/Ag
Foams	15	29	79	81	24	34
Foil	8	7	23	-	-	-

*Ag polished plate (experimental): 3.61*10⁻⁶ C cm⁻²

*Cu polished plate (experimental): 3.00*10⁻⁶ C cm⁻²

In order to deepen into the charge and mass transfer properties of the investigated samples, EIS analysis were performed both in borate plus 0.05 M and 0.02M HMF solution at -1.10 V vs SCE (-0.31 V vs RHE) potential. No significant differences were observed varying the HMF concentration, therefore, as an example, the data obtained at HMF 0.05M were reported and discussed.

Observing the Nyquist plots reported in Figure 3.16a it is evident the larger total impedance obtained for bare foams than those of displaced and electrodeposited samples (reported in the inset of Figure 3.16a). Another difference among these two pairs of samples is the shape of the Nyquist plots: in fact, the bare foams exhibit a typical two-time constant spectrum constituted by two arcs (partially overlapped in the case of Cu foam), while only a single arc is distinguishable for the Ag/Cu ED and GD samples.

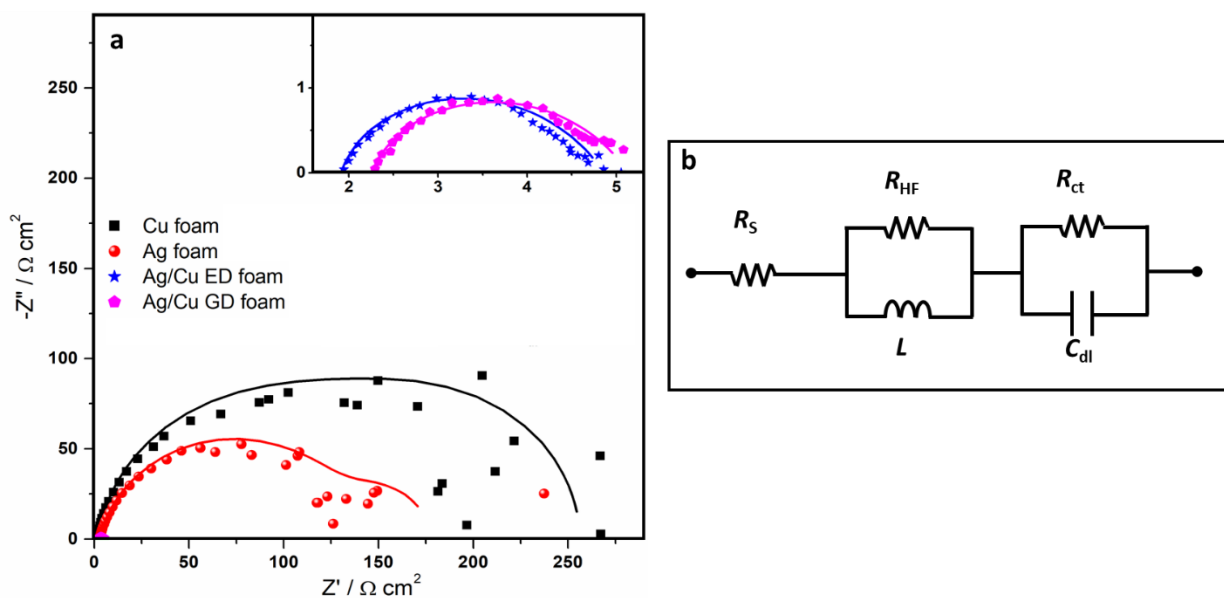


Figure 3.16. Nyquist plot from EIS measurements using the Ag/Cu ED, Ag/Cu GD, Cu bare, and Ag bare foams samples (a). The lines represent the data fitted by using the Randles equivalent circuit (b).

The experimental data are fitted through the Randles equivalent circuit shown in figure 3.16b,⁸⁷ constituted by a series resistance R_s (accounting for electrolyte and contact resistances), a charge transfer resistance R_{ct} , a double layer capacitance C_{dl} and a Warburg element Z_w (accounting for diffusion). The latter is not included in the fitting procedure of GD and ED samples, since only a time constant is exhibited by these two catalysts. The as-obtained parameters are resumed in Table 3.2. Similar R_s values are showed for all the samples; while, comparing R_{ct} and C_{dl} , bare foams exhibit rather larger resistances and lower capacitance than Ag/Cu samples, implying lower intrinsic activity and EASA, in accordance with the results obtained from Pb-UPD. Moreover, it is worth to note that both the foams are characterized by mass transport limitation, as evidenced by the presence of the low-frequency feature in their spectra. In particular, the diffusion resistances R_d , calculated from the Warburg element⁸⁸ and reported in Table 3.2, confirm that this phenomenon is more pronounced in Cu foam. Conversely, no evidence of mass transport limitation is present in both GD and ED samples. Finally, charge transfer time constants τ are calculated by multiplying R_{ct} and C_{dl} values⁸⁹ (see Table 3.2). It is found that the Ag/Cu ED sample is characterized by the lowest value, followed by the

Ag/Cu GD catalyst; quite larger values are exhibited by both the bare foams, implying that the charge transfer is slower for the latter samples. By summarizing the results obtained from the EIS analysis, we can expect larger activity of GD and ED samples attributed to their enhanced charge transfer properties and higher EASA with respect to the bare foams. Moreover, both Ag and Cu foams suffer of mass transport limitations that can further limit their electrochemical activity.

Table 3.2. EASA from Pb_{UPD} and equivalent electric parameters obtained from EIS analysis for Ag bare, Cu bare and Ag/Cu foams.

Sample	EASA / cm^2	R_s / Ωcm^2	R_{ct} / Ωcm^2	C_{dl} / $mF cm^{-2}$	R_d / Ωcm^2	τ / ms
Ag/Cu ED	79	1.9	2.7	5.79	-	15.7
Ag/Cu GD	81	2.3	3.1	6.57	-	20.4
Cu bare	15	2.0	144.3	0.21	110.6	30.3
Ag bare	29	2.8	136.9	0.24	38.2	33.2

3.4.3. Electrochemical hydrogenation of low concentrated HMF solutions

3.4.3.1. Electrochemical characterization of electrocatalysts

The role of the 3D supports on the electrocatalytic reduction of HMF to BHMF was firstly studied, focusing the work on the conversion of diluted HMF solutions (0.02 M), comparing the performances of foam- and foil-based electrocatalysts.

Preliminary, LSV experiments were performed in both borate buffer with and without HMF electrolytes in order to investigate the activity of the electrocatalysts towards the Hydrogen Evolution Reaction (HER) and HMF reduction, respectively (Figure 3.17).

In the HER, Cu is more active than Ag foam, indeed the discharge starts at ca. 100 mV lower overpotential and the current density increases faster at more cathodic potentials (Figure 3.17a); however, both are moderate H_2 evolution catalysts. The deposition of Ag by both ED and GD provokes a shift of the onset towards lower overpotentials compared to the bulk sample. Tafel slopes for the Ag/Cu ED and GD samples reported in Table 3.3 are very similar (95-100 $mV dec^{-1}$), meaning similar electron transfer kinetics for both. These values are around 1.2 and 2.1 times lower than for Cu and Ag bare foams, respectively, confirming an enhanced HER kinetics on the Ag/Cu electrocatalyst surfaces. Hence, the nanostructuring of the foam surface with AgCu bimetallic and the higher EASA increases the activity in the HER in comparison to pure Ag.

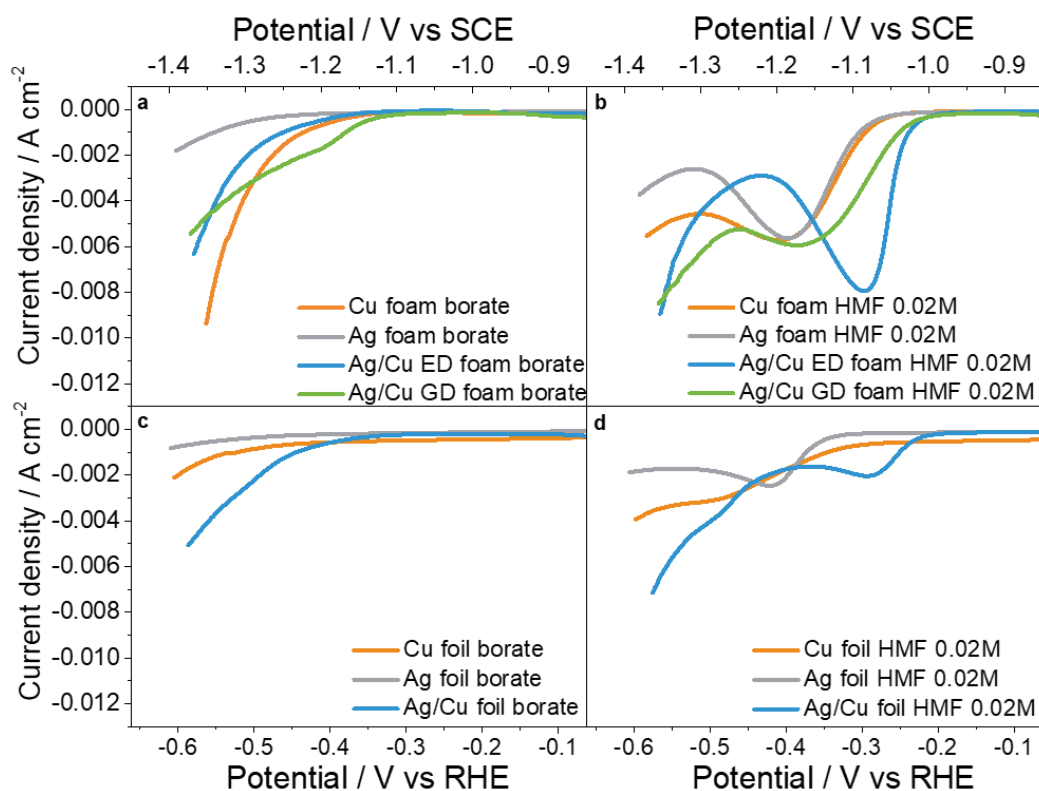


Figure 3.17 Linear Sweep Voltammeteries over Ag, Cu, and Ag/Cu foam and foil electrocatalysts in borate buffer (pH=9.2) and 0.02 M HMF+borate buffer. a, b) LSVs recorded for foams; c, d) LSVs recorded for foils. Range: 0 to -1.4 V vs SCE. Scan rate: 1 mV/s in borate solutions and 5 mV/s in HMF containing solutions.

Indeed, the Ag/Cu ED catalyst behaves in between Ag and Cu electrodes, with the LSV curve that only shifts by around 30 mV towards more negative potentials in comparison to Cu (Figure 3.17a), and a lower current density is recorded afterwards, due to the poor activity of Ag in HER. Conversely, Ag/Cu GD foam is more active for HER, with an onset potential ca. 90mV lower than Ag/Cu ED and 60mV lower than Cu foam.

Table 3.3. Tafel slopes determined from LSVs recorded in the electrolytes containing borate and borate+HMF 0.02 M.

Sample	Slope Borate / mV dec ⁻¹	Slope HMF 0.02 M / mV dec ⁻¹
Ag/Cu ED fresh	99	39
Ag/Cu GD fresh	95	70
Cu bare	119	69
Ag bare	196	73

It should be remarked that at less cathodic potentials than -0.9 V vs SCE (-0.11 vs RHE) some peaks are recorded (not shown). In particular, a high intensity peak at around -0.8 V vs SCE (-0.01 V vs

RHE), probably related to copper oxides reduction, is observed only in the first LSV in borate over Ag/Cu foam, while it is absent in Cu foams. The peak disappears in the following LSVs.

Adding HMF in the electrolytes, the characteristic peak of HMF reduction occurs at less cathodic potentials than the HER discharge (Figure 3.17b).⁶³ The easy reduction of HMF has been related to the delocalization of the charge in the furan ring,⁶¹ though the type of catalyst determines the overpotential and the kinetics, suggesting that the HMF reduction is more affected by the catalyst structure and composition than the HER.

The onset and minimum of the peak are quite similar for Ag and Cu foam. At more cathodic potentials than -1.2 V vs SCE (-0.41 V vs RHE) both HER and HMF reduction contribute to the shape of peak, but HER becomes dominant by moving to more negative potentials. Therefore, the higher electroactivity of Cu for HER can explain the change in the shape of the curve observed in that potential region. Remarkably, the presence of Ag, as NPs or dendrites on the surface of the Cu foam, reduces the HMF hydrogenation overpotential of about 60 mV for both GD and ED electrocatalysts. The onsets observed in figure 3.17b for both Ag/Cu foams are in agreement with that reported by Roylance et al⁶³ for Ag displaced on Cu foil.

The enhanced kinetics in HMF reduction, in comparison to the HER, is demonstrated by a decrease in the Tafel slope for all the catalysts. The slope values indicate that the charge transfer occurs faster for Cu than Ag (67 vs 73 mV dec⁻¹) and that only the ED method contributes to an enhancement of the kinetics (39 mV dec⁻¹), in comparison to Cu foam. The enhancement in the activity of the Ag/Cu electrocatalysts in the HMF reduction, in comparison to Ag and Cu bare foams, could be related to an increase in the intrinsic activity and/or in the mass transfer, as confirmed by the EIS analyses. The differences between catalysts can be related to a different extent of the frontier orbital overlap with the HMF and in the morphology that in turn modify their mass transfer resistance.

Unlike foams, the onset for the HER observed for Ag and Cu foils is quite similar (Figure 3.17c), though for the latter a higher current density is recorded. In Ag/Cu foil the current greatly increases in comparison to Ag and Cu foils; the onset was recorded at ca. 100 mV less cathodic potential, at potential values comparable with those observed for Ag/Cu foams.

The HMF reduction onset is around 30 mV forward for foils than foams and the current densities exchanged decrease (Figure 3.17d). A low intensity peak is observed for Ag and Ag/Cu samples, while a shoulder is only recorded for Cu. The feature at around -1.27 V vs SCE (-0.48 V vs RHE) for the Ag/Cu sample has not been clearly identified yet but may be related to the further reduction of species adsorbed on surface.

Hence, it would appear that the large surface area of the foams may improve the electroreduction of HMF.

3.4.3.2. Electrolysis of a 0.02M HMF solutions

After the LSVs in borate, and borate with HMF, the electrolysis of a 0.02 M HMF solution at -1.3 V vs SCE (-0.51 vs RHE) were performed for foams and foil electrocatalysts. The charge accumulated is 96.5 C, corresponding to theoretical charge to selectively reduce all the 0.02 M HMF to BHMF, considering a $2e^-$ process and 100% FE.

From Figure 3.18a it can be observed a fast decrease of current density, during the first ca. 1800 and 300 s, for Ag and Cu foams, respectively, due to their mass transfer limitation. Moreover, Cu reached a greater limiting current density, probably related to the faster kinetics exhibited for HMF reduction or a higher contribution of the HER, compared to Ag bulk.

The largest surface area of Ag/Cu foams may provide an increase in the charge and mass transfer, and therefore in the reaction rate at similar potentials. Hence, the decreases in the current density with time is slower in ED and GD than in bare foams, avoiding to reach the limiting current density (Figure 3.18a). However, the faster kinetics of Ag/Cu ED observed from figure 3.17a and table 3.3, provokes the development of a higher current density compared to GD foams.

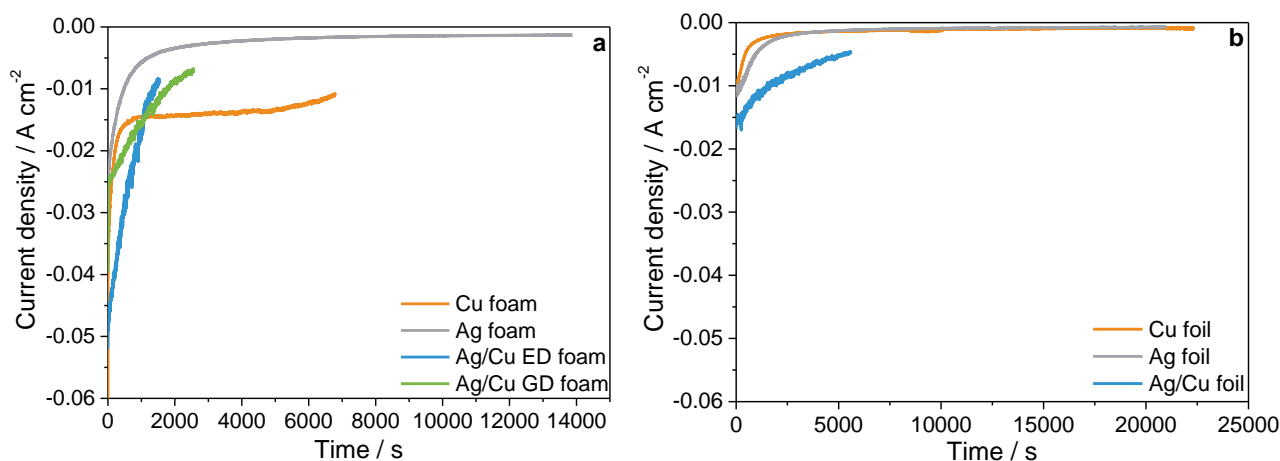


Figure 3.18. Current density-time plot recorded for the reduction of a 0.02 M HMF solutions in borate buffer (pH=9.2) at -1.3 V vs SCE (-0.51 V vs RHE) over foams (a) and foils (b) electrocatalysts. The charge accumulated for Ag and Cu foils was 60 C.

The electrolysis results in figure 3.19a showed that Ag deposited outperforms Cu electrocatalyst in both HMF conversion and BHMF selectivity. For Ag, 93% conversion and 75% selectivity values are achieved and the low FE, ca. 69%, is related to the formation of other HMF derived by-products. The Cu bare foam is less active and selective in the conversion of HMF to BHMF, and in turn FE is only 47%. Conversely, a higher BHMF productivity was reached over Cu than for the Ag foam, due

to the shorter time to accumulate the full charge, i.e. 6890 s for Cu vs 13875 s for the Ag electrode, related to the higher contribution of the HER. Therefore, despite the faster reaction rate for both HER and HMF exhibited from Cu foam than Ag, HMF mainly evolves to other by-products.

Ag/Cu foams almost selectively convert HMF to BHMF (Sel. BHMF >98%), while the conversion is ca. 85 and 90% for GD and ED electrodes, respectively.

Hence, nanostructuring the foams with Ag particles improve the catalytic activity. The configuration of the HMF molecule activated on the catalyst surface could be modified as well as the kinetics of HER and HMF reduction. However, unlike for Cu and Ag foams, BHMF selectivity is very high.

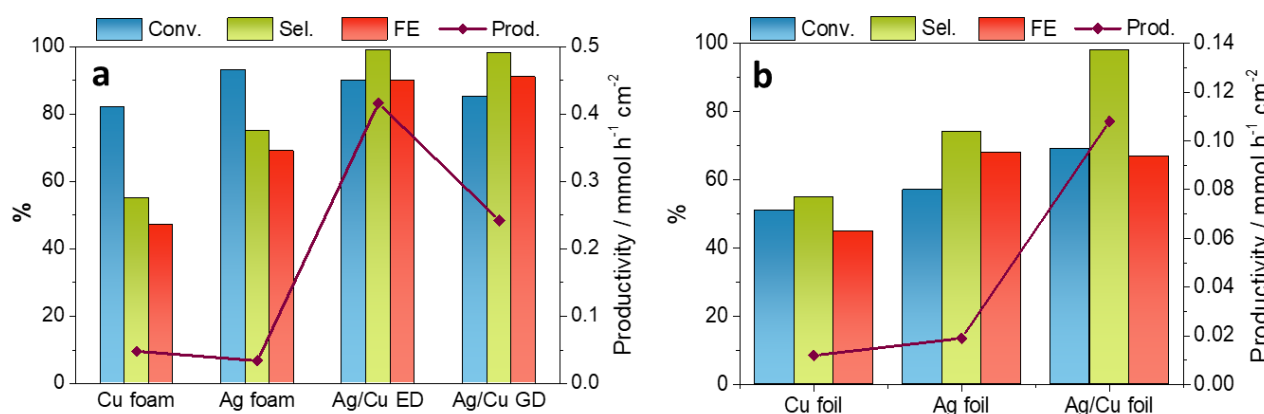


Figure 3.19. Results from electrolysis of a 0.02 M HMF solution in borate buffer (pH=9.2) at -1.3 V vs SCE (-0.51 V vs RHE) over Ag, Cu and Ag/Cu foams and foils.

To investigate the role of 3D supports used and their effect on catalytic activity, the results obtained using foil-based electrode counterparts were compared. The effect of a lower surface area of foil electrodes is observed in figure 3.18b, where a decrease in the current density recorded and, consequently, an increase in the length of the experiments occur. Both Ag and Cu electrocatalysts reach a limiting current density of ca. 0.001 A cm⁻², nevertheless the process was too slow to reach the expected charge value, the reaction was stopped after 60 C collected. This does not allow an accurate comparison between Ag and Cu bare foil and foam, nevertheless, it should be noted that selectivities were rather similar to those obtained over foam electrocatalysts (Figure 3.19b). On the other hand, for Ag/Cu foil, like for the foam counterpart, the current density exponentially decreases with the time and it does not reach the limiting current.

Ag nanoparticles on the Cu foil support allow to selectively convert HMF into BHMF (Sel. ~ 98%). Conversely, conversion and FE are low, probably due to the contribution of the HER. Consequently, productivity, strongly influenced by longer reaction time, also largely decreases in comparison to foams, e.g. 0.108 vs 0.416 and 0.242 mmol h⁻¹ cm⁻² for foil, ED and GD foams, respectively.

It should be noted that the productivity is higher than those reported in literature. For instance, Roylance et al. reported a productivity of 0.088 mmol h⁻¹ cm⁻² after 60 C passed (99 % selectivity

86% FE),⁶³ while for Zhang et al. the reported productivity is 0.052 mmol h⁻¹ cm⁻² (28% HMF conversion and 100% FE).⁷¹ These results highlight the advantages of using electrodes based on open-cell foams with a high surface area to increase the efficiency of the process.

3.4.3.3. Stability tests in 0.02M HMF solutions

The stability of the electrodeposited and displaced electrocatalysts was tested performing two more electrocatalytic cycles. LSVs are slightly modified before and after the first electrolysis (Figure 3.20a, b) and the profile of current density during electrolysis also changes (Figure 3.20a1, b1). The time required to collect the charge to selectively convert all the HMF to BHMF changes from the first to the third cycle, modifying the productivity, but the electrocatalytic performance in terms of conversion, selectivity and FE are kept constant (Figure 3.20a2, b2). Tafel slopes for ED and GD (63.7 and 79.2 V dec⁻¹, respectively) reveal that the kinetics of charge transfer of the catalysts for both HER and HMF reduction are decreased after the first cycle. It would appear that the kinetics of HMF reduction are modified along the cycles, consequently influencing on the BHMF productivity. The changes in the shape of the current density-time curves could be related to mass transfer modify because of changes in the morphology of the coatings.

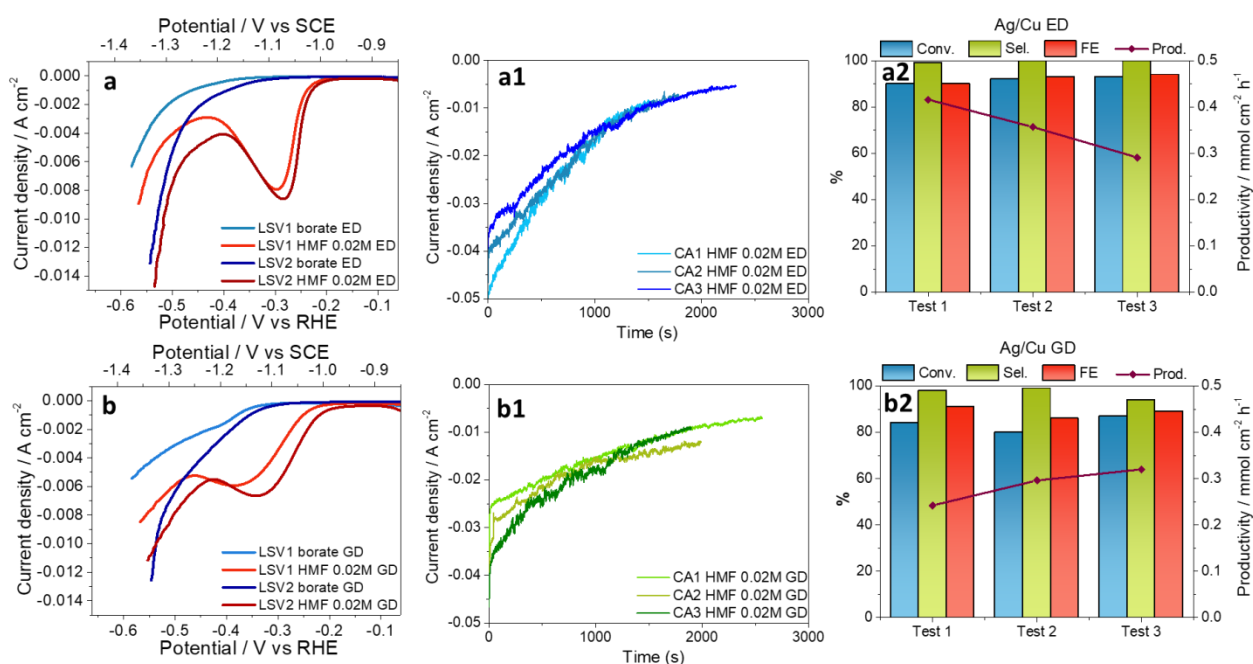


Figure 3.20. LSV in borate and borate+HMF 0.02M (a, b), Current transient of three electrolyses (a1, b1) and results of electrolyses in a 0.02 M HMF solution in borate buffer (pH=9.2) at -1.3 V vs SCE (-0.51 V vs RHE) over Ag/Cu ED and Ag/Cu GD foams, respectively.

3.4.4. Selective Hydrogenation of concentrated HMF solutions

The effect of the HMF concentration on the electroactivity of Ag/Cu GD and ED foams was investigated performing LSVs and chronoamperometries in 0.05 M (compared with Ag and Cu bare foams) and 0.10 M HMF solutions under similar conditions.

LSVs performed in 0.05 M HMF solution showed the same trend observed at 0.02 M HMF, with the only difference that the onset for Ag foam is shifted at more cathodic potentials. The absence of the peak in the Cu catalyst in 0.05 M HMF suggests a lower activity or a mass-transfer limited process. No significant differences were found for ED electrodes for both 0.02 and 0.05 M HMF concentrations investigated, conversely, the onset of GD sample occurs at around 50 mV lower overpotential using HMF 0.10 M; a general increase in the faradaic current was recorded, but not proportionally to the HMF concentration (Figure 3.21). This behaviour could be related to the adsorption of organic compounds on the surface of the electrode, likewise for furfural on Cu electrodes⁶⁷ or due to the competition between HER and HMF reduction⁶⁵.

ED sample reaches, for all the concentrations at a lower potential applied, a higher current density compared to the GD catalyst; except for HMF 0.10 M where the reduction peak is shifted at more cathodic overpotential, probably due to a greater contribution of HER, which allows to develop a greater current density at more negative potentials than -1.2 V vs SCE.

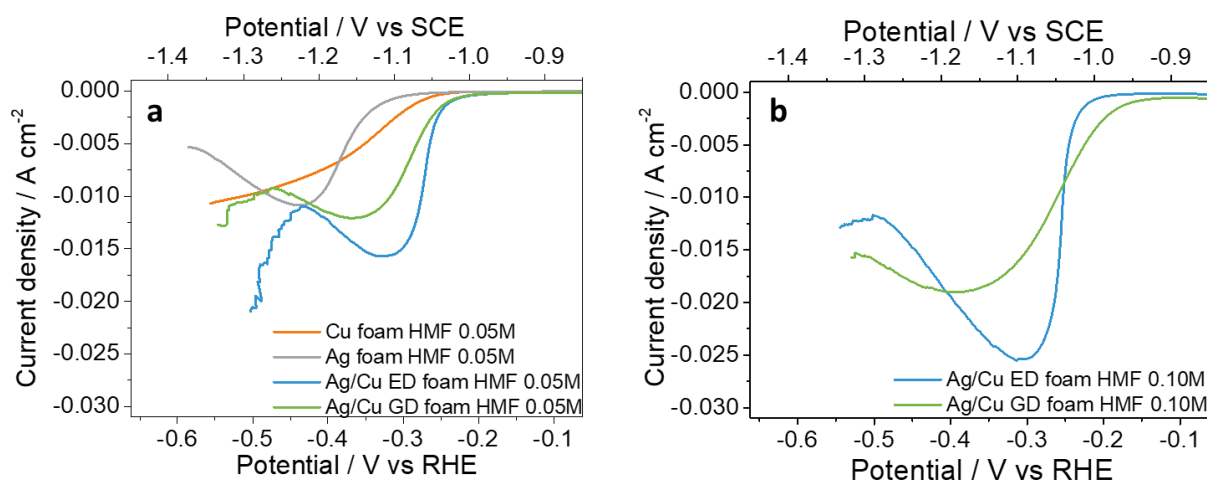


Figure 3.21. LSVs performed in: borate+HMF 0.05M over Ag, Cu, Ag/Cu ED and Ag/Cu GD foams (a) and borate+HMF 0.10 M (b) over Ag/Cu ED and GD foams.

The effect of the deposition of AgCu bimetallic particles, observed at 0.02 M HMF solution, is also evident at high HMF concentration (Figure 3.22). Both Ag/Cu ED and GD catalysts increase the conversion of HMF (~100%) towards BHMF in comparison to the bare foams, and in particular to the Cu electrode. Electrodeposited and displaced catalysts reach BHMF selectivity values (83 and 89 %, respectively, at HMF 0.05 M) well above those obtained for the bare foams (44 % and 65 % for

Cu and Ag, respectively). But, in the more concentrated solution (0.10 M) the selectivity suffers a further drop (Figure 3.22d); note that the GD catalyst preserves acceptable performances (79% selectivity against 69% for ED). The lower FE values seem to be mainly related to the formation of by-products rather than to the contribution of the HER (Figure 3.22c).

Increasing the concentration of HMF, a long reaction time was necessary to accumulate the charge, (Figure 3.22a, b), this, combined with the lower selectivity, provoke a large decrease in productivities, unlike for the electrocatalytic hydrogenation of benzaldehyde, where the increase in the concentration enhanced productivity⁹⁰.

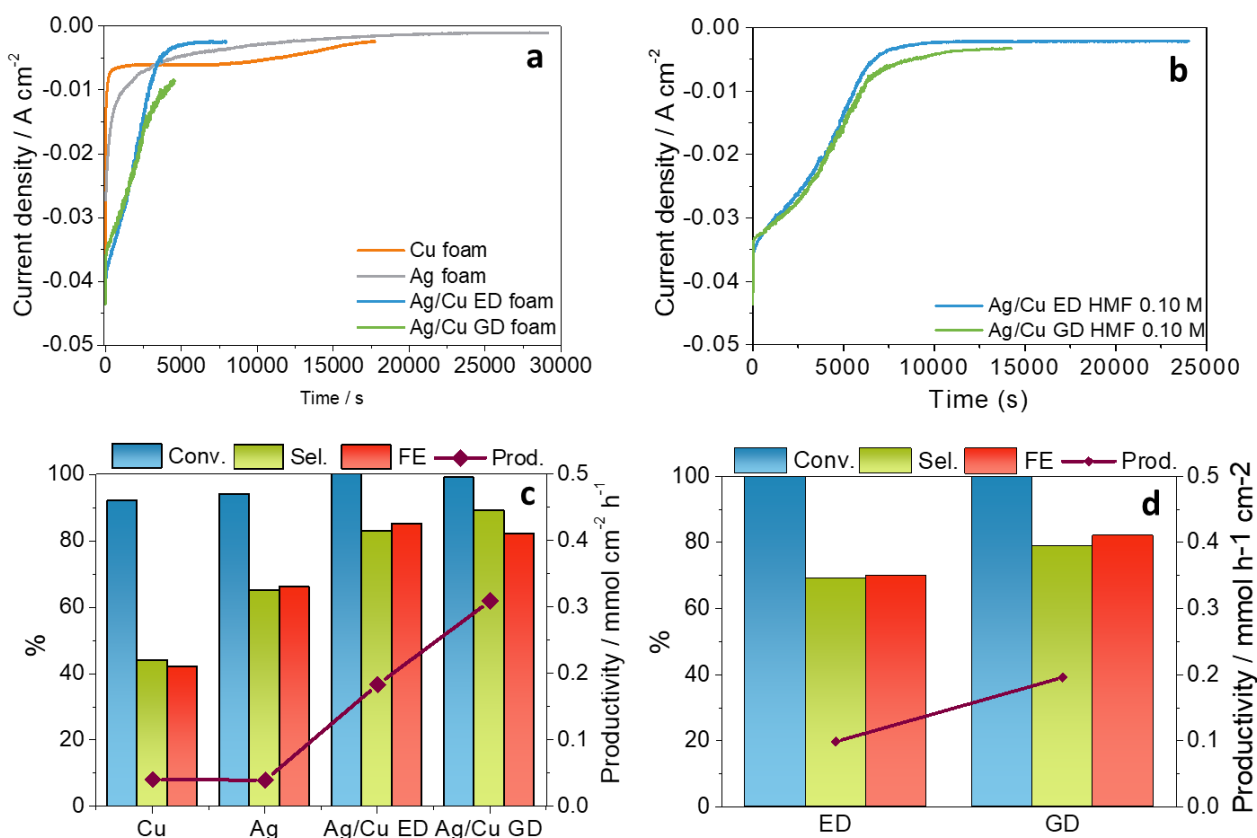


Figure 3.22. Current density vs time curves recorded at -1.3 V vs SCE (-0.51 V vs RHE) in HMF 0.05 M (a) and 0.10 M (b). HMF conversion, BHMF selectivity, Faradaic Efficiency and Productivity obtained after electrolysis of 0.05 M (c) and 0.10 M (d) HMF.

The features of activity and selectivity exhibited by coated electrocatalysts compared to bulk foams could be related to the electroactive surface area, mass and charge transfer (as above confirmed by EIS) and to the composition and shape of the catalyst particles, i.e. nanostructuring of foam. Hence, in order to separate both contributions, the nanostructuring of the surface of the Cu and Ag bare foams is performed by electrodepositing Cu and Ag nanoparticles, respectively.

Actually, the tests performed on Ag/Ag and Cu/Cu catalysts, using HMF 0.05 M, demonstrate that the increase of surface area caused by nanostructuring, improve the performances of bare foams

(Figure 3.23). Nevertheless, the activity and selectivity resulted lower compared to bimetallic samples. These results suggest that there is a synergistic role due to the presence of Ag and Cu that drives the reaction to the desired products.

Making a comparison between Ag/Cu ED and GD, the former sample is more active, considering the amount of Ag loaded, while the GD sample due to the hierarchical porosity may increase the mass transfer, therefore the number of aldehydes at the electrode/electrolyte interface, and in turn the productivity.

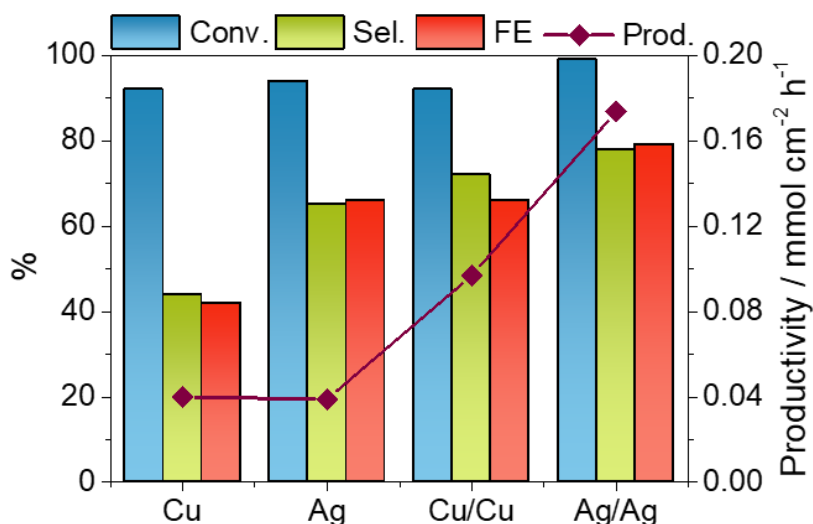


Figure 3.23. Results of electrolysis at -1.3 V vs SCE in borate plus 0.05 M HMF for Ag/Ag, Cu/Cu, Cu and Ag bare foams.

As already done for low concentrated HMF solutions, three catalytic cycles, including electrolysis, and LSVs in both borate and borate+HMF, were carried out with the aim to evaluate the stability of GD and ED samples in 0.05M HMF solutions. The foams showed the same behaviour previously observed at 0.02 M. Changes occur in the LSVs after electrolysis, with the Tafel slopes that reveal a decrease in the kinetics of charge transfer of the catalysts for both HER and HMF (Table 3.4).

Table 3.4. Tafel slopes of fresh and spent Ag/Cu ED and GD electrocatalysts in borate and borate plus HMF 0.05 M.

Sample	Slope Borate /	Slope HMF 0.05 M /
	mV dec ⁻¹	mV dec ⁻¹
Ag/Cu ED fresh	99	39
Ag/Cu ED spent	115	45
Ag/Cu GD fresh	95	56
Ag/Cu GD spent	108	61

The performances are rather constant, while the reaction time enlarges, modifying the productivity (Figure 3.24), probably due to changes in the morphology of the coatings.

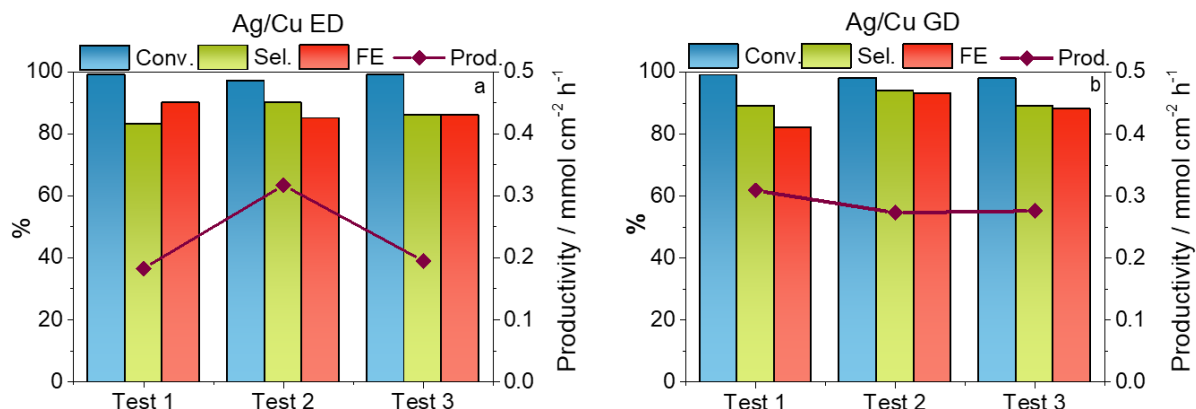


Figure 3.24. Results of electrolysis at -1.3 V vs SCE in borate plus 0.05 M HMF over Ag/Cu ED (a) and Ag/Cu GD (b) foams for three consecutive electrolysis.

3.4.5. Influence of the Area-catalyst/Volume-reaction ratio

The last parameter investigated is the ratio between the “geometric area” of the catalyst employed and the volume of electrolyte. In the previous sections, the catalysts are a piece with dimension of 10 mm x 10 mm, tested in 25 mL of electrolyte; in this section two other cases were studied: in the first one it was evaluated the effect of an ED electrode with double dimension (20 mm x 10 mm) in 25 mL of solution, named as “ED 20x10”; in the second one, conversely, a double volume of electrolyte was employed (50 mL) with a normal electrode (10 mm x 10 mm); the catalyst was called as “ED 50mL”. In both cases the concentration of HMF used was 0.05 M and the catalytic tests were carried out using the same configuration employed for the previous ones.

The results of electrolyses (Fig. 3.25) showed that the increase of the volume of electrolyte does not affect the catalytic activity of the Ag/Cu sample, reaching almost the same conversion and selectivity. Therefore, the same catalyst can be used to successfully convert solutions of different volumes, obtaining the same results.

Conversely, a further increase of the surface area worsens the performances, with the conversion of HMF that remains high, while the selectivity towards BHMF decreases. Hence, it is necessary to modify the set-up of the cell and/or the reaction/synthesis conditions to maintain or improve the performances of the catalyst with increasing the geometric area. However, further analyses are needed to clarify this behaviour.

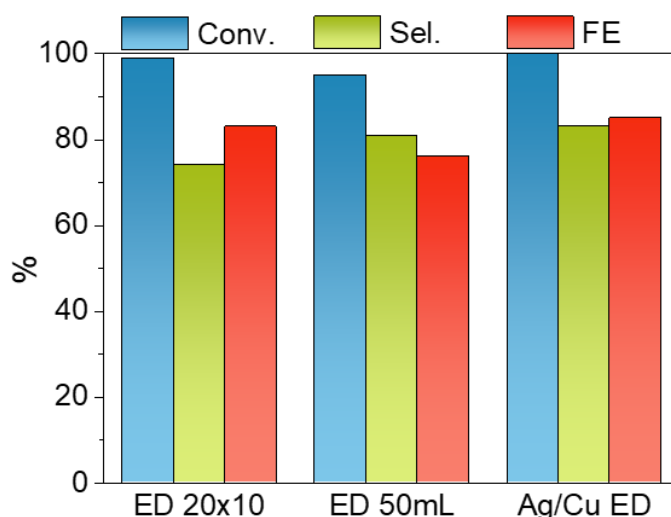


Figure 3.25. Results of electrochemical hydrogenation of a 0.05 M HMF solution at -1.3 V vs SCE over Ag/Cu ED electrocatalysts with different area-catalyst/reaction-volume ratio.

3.4.6. Identification of By-products

The decrease in BHMF selectivity observed with increasing HMF concentration is due to the formation of by-products during electrolysis. The GC-MS analyses, of a post-electrolysis 0.05M HMF solution, evidence the formation of 5-methyl-2-furanmethanol and 5-methyl-2-furaldehyde (Figure 3.26) and the presence of high molecular weight products. It should be noted that no substantial differences emerged between the type of by-products generated, not quantified, using ED or GD electrodes or changing the starting HMF concentration.

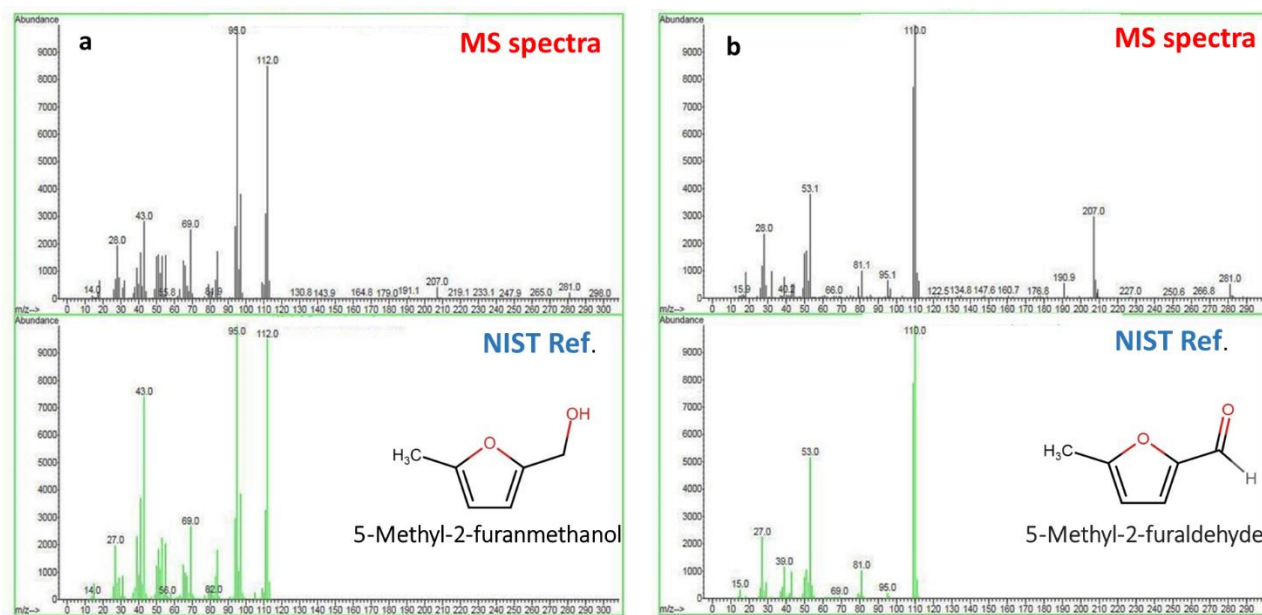


Figure 3.26. GC-MS spectra recorded in a 0.05 M HMF solution after electrolysis at -1.3 V vs SCE over Ag/Cu ED foam catalyst and identification of two by-products: 5-methyl-2-furanmethanol (a) and 5-methyl-2-furaldehyde (b).

The production of 5-methyl-2-furanmethanol occurs by HMF hydrogenolysis and it is related to the presence of Cu.⁷¹ The process could follow the hypothetical pathway above reported in figure 3.3, through the formation of 5-methyl-2-furaldehyde,^{21,65} also identified in GC-MS. It should be considered that making a comparison between our work and the previous one is not straightforward because the differences in reaction conditions.

The presence of a high molecular weight signal suggests the possible formation of dimers and oligomers, previously reported, but not identified, by Roylance et al.;⁶³ while, very recently Chadderdon et al. found the formation of 5,5'-bis(hydroxymethyl)hydrofuroin.⁵⁵

To increase the amount of by-product in solution and simplifying their identification, an electrolysis in a highly concentrated HMF solution (0.50 M) was performed using the Ag/Cu ED foam, accumulating 1152 C instead of 2412 C, because of time issues, and obtaining 96% of HMF conversion and 23% of BHMF selectivity. Actually, in HPLC chromatograms some unknown peaks are observed and, particularly, the most intense one is eluting close to the BHMF peak (Figure 3.27). ESI-MS was employed to further investigate the formation of higher molecular compounds, by analysis of post-electrolysis HMF 0.50 M solution.

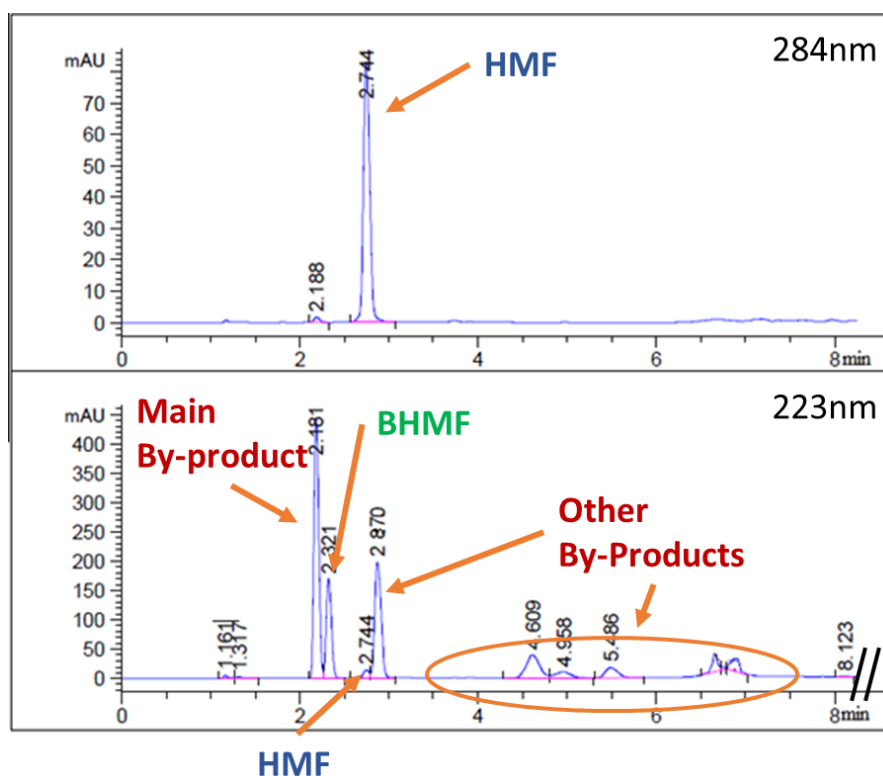


Figure 3.27. HPLC chromatograms of a 0.50 M HMF solution after electrolysis at -1.3 V vs SCE over Ag/Cu ED foam catalyst. The peak of HMF ($R_t = 2.7$ min) was identified using a wavelength of 284 nm. The peak of BHMF ($R_t = 2.3$ min) was identified with a wavelength of 223 nm. The main by-product ($R_t = 2.18$ min) and the other by-products are visible at 223 nm.

The sample was previously extracted with acetonitrile, for three times, to eliminate the aqueous solvent. The MS spectra of as-prepared organic phase also reveals a main peak with a 277 m/z, while the signal of HMF, BHMF and other by-products became traces (Figure 3.28). The 277 m/z corresponds to a 254 mass (277-23); the effective m/z value can be obtained subtracting the mass of coupled-Na (23) from the m/z found. The 254 m/z fits perfectly with the molecular weight of 5,5'-bis(hydroxymethyl)hydrofuroin.

Subsequently, a HPLC analysis was performed to verify the results of the extraction. Chromatograms confirm that the unknown peak is the most observed product in organic phase, with some traces of HMF and BHMF and others (Figure 3.29). Hence, it could be concluded that this peak is related to the 5,5'-bis(hydroxymethyl)hydrofuroin, and that is one of the most abundant by-products.

The proposed mechanism of hydrofuroin formation proceeds by the aldehyde reduction through $1e^-/1H^+$ transfer, which generates a radical that reacts with another radical forming the hydrofuroin (Scheme 3.2) or that further polymerizes as previously observed for furfural and benzaldehyde^{58,67} and recently reported for HMF.⁵⁵

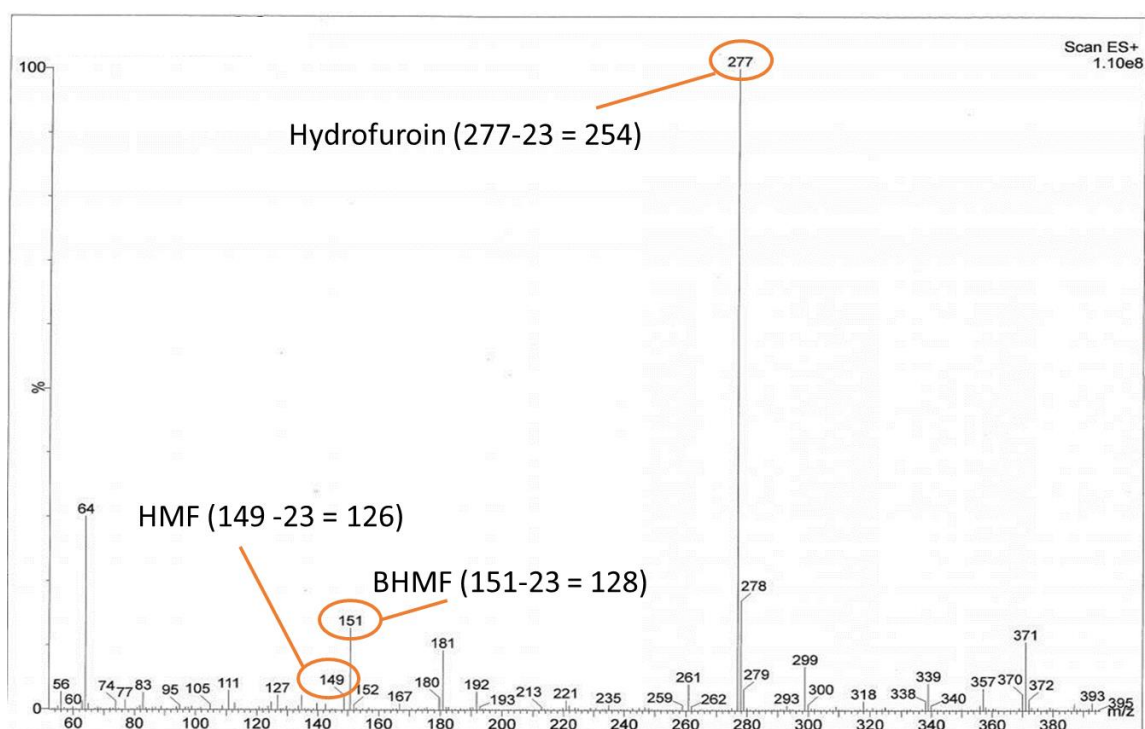


Figure 3.28. ESI-MS spectra of organic phase extracted from a 0.50 M HMF solution after electrolysis at -1.3 V vs SCE over Ag/Cu ED foam catalyst.

Obviously, the process became favoured with the increase of HMF concentration on the electrode surface, because a greater number of HMF molecules are prone to react. Moreover it has been reported that the competition between HMF reduction to BHMF and hydrodimerization and HER is potential-

dependent⁵⁵. This mechanism also explains the almost full conversion of HMF 0.50 M despite the charge accumulated is only 1152 C (instead 2412 C required).

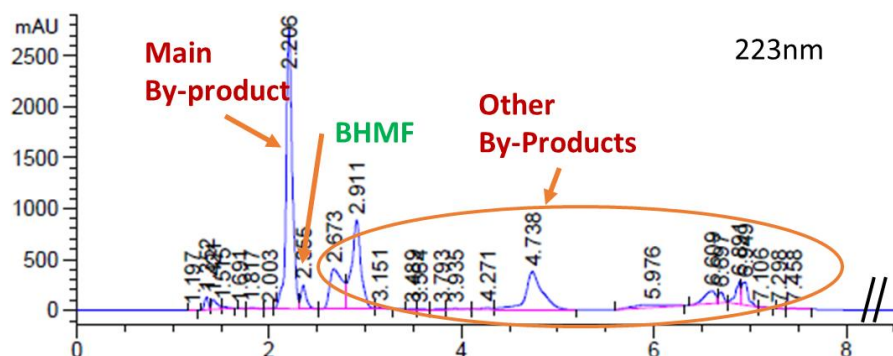
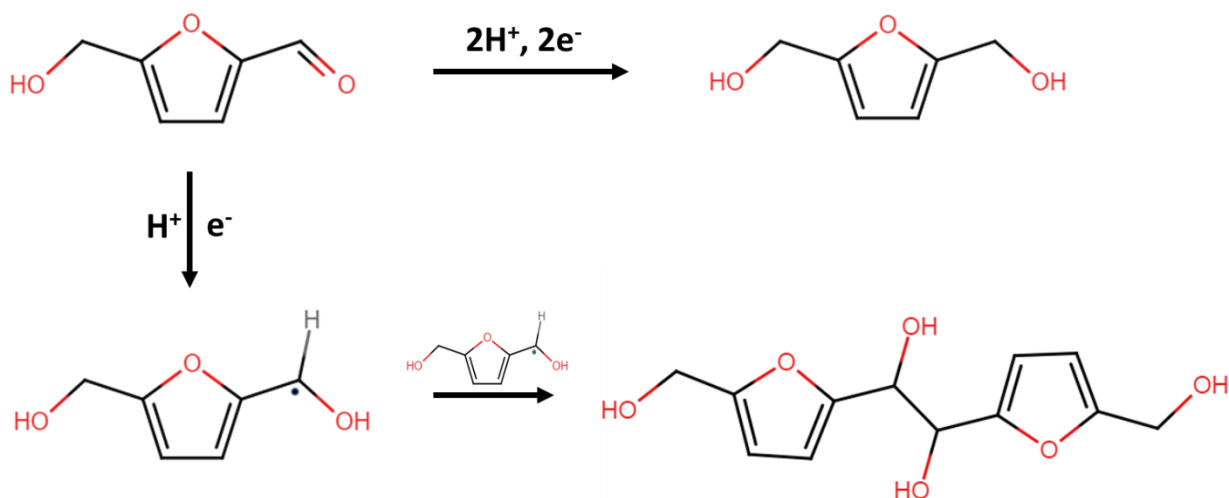


Figure 3.29. Chromatograms of organic phase extracted.

An electrochemical test performed in BHMF 0.05M, applying a -1.3 V vs SCE potential in the same reaction conditions, demonstrate that the formation pathway of by product starts from HMF and not involves BHMF. Indeed, the HPLC chromatograms of the post-reaction solution do not show the peak attributed to the 5,5'-bis(hydroxymethyl)hydrofuroin, confirming its substantially inactivity towards further hydrogenation or dimerization processes.



Scheme 3.2. Routes for the electrochemical conversion of HMF to BHMF (top) and radicalic mechanism for the formation of 5,5'-bis(hydroxymethyl) hydrofuroin (bottom).

Currently, we are not able to quantify the production of hydrofuroin, hence, we can estimate its formation by normalization of the area of the peak recorded on chromatograms with HMF conversion. The results resumed in table 3.5 correlate the dimer formation with the type of catalyst used and HMF concentration employed. The data show that, in general, the production of hydrofuroin is correlated with HMF concentration in solution, in agreement with the formation mechanism discussed above. Nevertheless, interesting trends can be observed. At 0.02 M, the lower furoin production over Cu

bare foam could be due to the occurrence of a different reaction pathway, such as hydrogenolysis, which leads to the formation of a higher amount of other by-products (e.g. 5-methyl-2-furaldehyde); instead, using HMF 0.05 M the greater number of HMF molecules activated on surface leads to the formation of hydrofuroin. This hypothesis agrees with the data of nanostructured monometallic foams that reach higher BHMF selectivity than bare foams with a slightly lower furoin production. The large surface area of AgCu particles deposited on Cu foams, enhances the BHMF selectivity and consequently limits the formation of hydrofuroin.

Table 3.5. Area of the peaks normalized for HMF conversion at 0.02 M, 0.05 M and 0.10 M HMF over various mono- and bi-metallic foam catalysts.

Sample	0.02 M	0.05 M	0.10 M
<i>Cu bare</i>	160	841	-
<i>Ag bare</i>	255	501	-
<i>Ag/Cu ED</i>	75	468	1023
<i>Ag/Cu GD</i>	130	521	1299
<i>Cu/Cu</i>	-	713	-
<i>Ag/Ag</i>	-	383	-

3.4.7. Effect of reaction time

In order to investigate the effect of the reaction time on the electrochemical hydrogenation, including the formation of hydrofuroin side product, aliquots of 0.05 M HMF solutions electrolytes (ca. 0.6 - 0.7 mL) were withdrawn with a syringe, assuming that the composition of the solution is homogeneous thanks to stirring. The withdrawals are set at certain amount of charge accumulated: 50, 100, 150, 200, 220 and 241 C for HMF 0.05 M. The results are shown in figure 3.30.

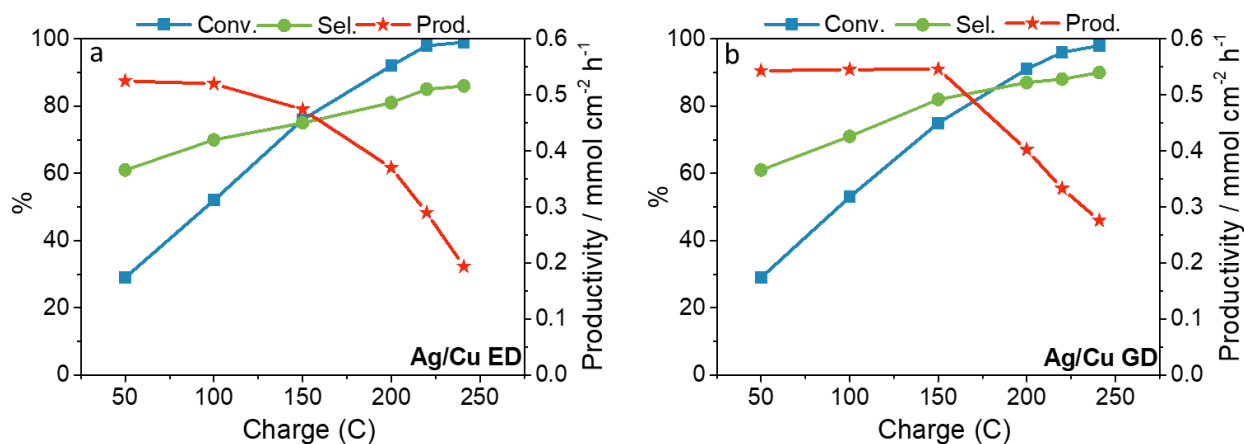


Figure 3.30. Evolution of HMF conversion, BHMF selectivity and productivity as a function of charge passed for HMF 0.05 M over Ag/Cu ED (a) and GD (b) foams.

HMF conversion steadily increases with the charge accumulated regardless the electrocatalyst and the same trend can be observed for the BHMF selectivity (Figure 3.30a, b). For instance, after 20 C passed, both ED and GD catalysts showed a selectivity of 61% with a conversion of 29%, while at the end of reaction the conversion is almost 100 % and the selectivity reached 86% for ED and 90% for GD samples.

A gradually decrease in productivity is reported, as a consequence of the increase in the time elapsed between one step of passed charge and the next.

To explain the trend in selectivity, observed during the reaction time, the furoin-peak/HMF-conv. ratio will be discussed (Fig. 3.31). We can consider this parameter as a “pseudo-rate” of dimer formation. From the graph we can observe that the greater amount of furoin is produced at the beginning of the reaction, and its formation rate quickly decreases with time for both ED and GD samples. This leads the increase of selectivity observed with the charge passed.

The differences observed for the two catalysts, on this parameter, lead at the end of the reaction to obtain different values of total selectivity. Indeed, the lower selectivity of Ag/Cu sample corresponds to a higher amount of hydrofuroin formed.

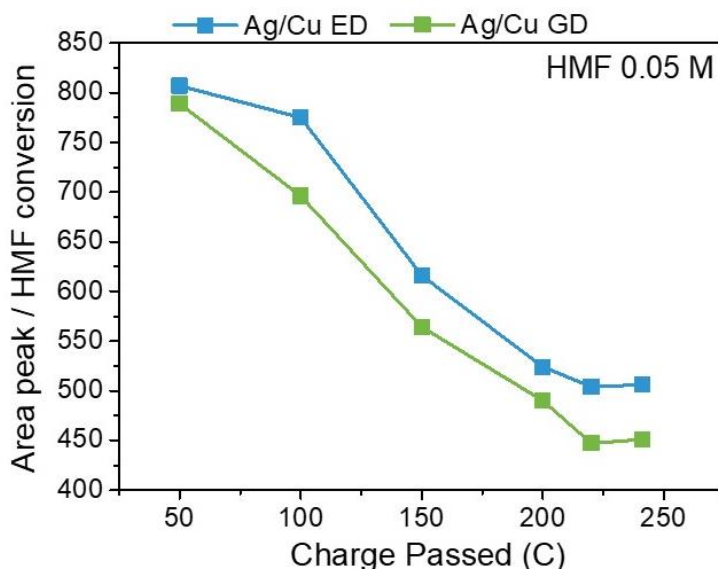


Figure 3.31. Evolution of Hydrofuroin peak/HMF conv. as a function of charge at 0.05 M HMF obtained for both Ag/Cu GD and ED electrocatalysts.

3.4.8. Characterization of electrocatalysts after electrochemical tests

After the catalytic cycles the coating of the foams is rather stable and no detachment was detected (Fig. 3.32). The ICP analyses indicate that Ag leaching does not occur for ED sample, conversely it is observed for the GD sample, with an estimated Ag concentration in the electrolyte lower than 4.5

ppm. This could also suggest that Ag leaching for ED samples could happen, but its amount is below that of the detection limit of the instrument.

Some carbon deposits are identified by EDS analyses, related to organic species adsorbed on the surface; in particular, the presence of dimer or oligomers could be responsible of the carbon build-up on the surface of the electrode.

High resolution FE-SEM images reveal that the sintering of AgCu particles, in both electrodeposited and displaced catalysts, occurs during the electrochemical tests. Changes in the shape of the particles in both the arrays of particles and within the dendrites can be observed, which became more rounded and interconnected (Fig. 3.33), suggesting that the sintering occurs by coalescence and Ostwald ripening mechanisms.

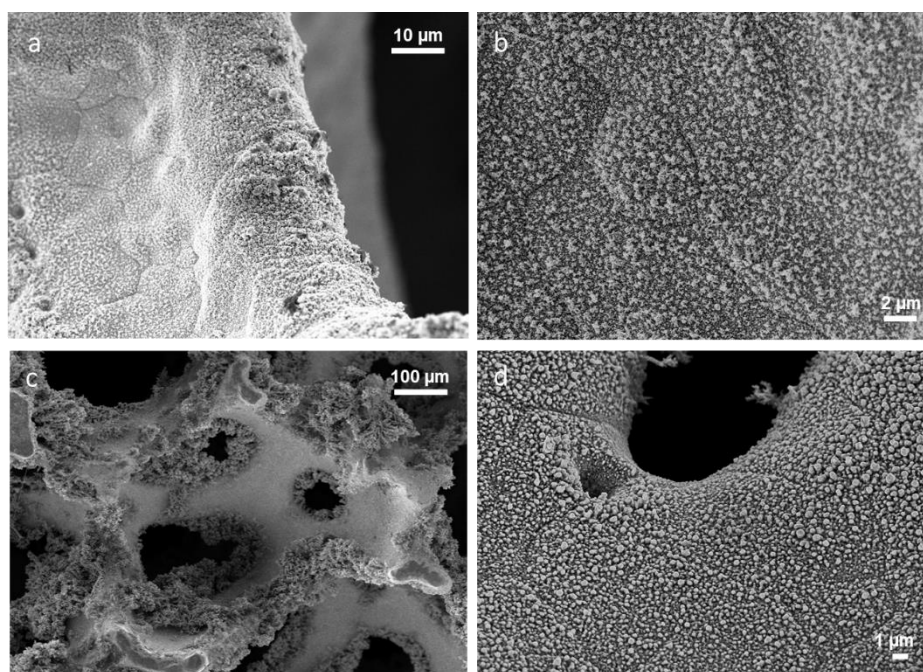


Figure 3.32. FE-SEM images of Ag/Cu ED (a, b) and Ag/Cu GD (c, d) spent catalysts.

Note that the particle size distributions obtained by TEM confirm the growth of the deposits; for ED sample a widening of the distribution is observed with a loss of homogeneity (Figure 3.33a2), GD sample showed a more pronounced growth of particles with the formation of agglomerates of 20 – 50 nm (Figure 3.33b2).

The sintering of silver is confirmed by XRD for the GD sample (Fig. 3.34a), which displays more intense Ag^0 reflections in the pattern after tests. Conversely, there are not remarkable differences for the ED sample. The reflections of Cu_2O are not observed in the patterns of both spent samples, despite the catalysts were exposed to the air.

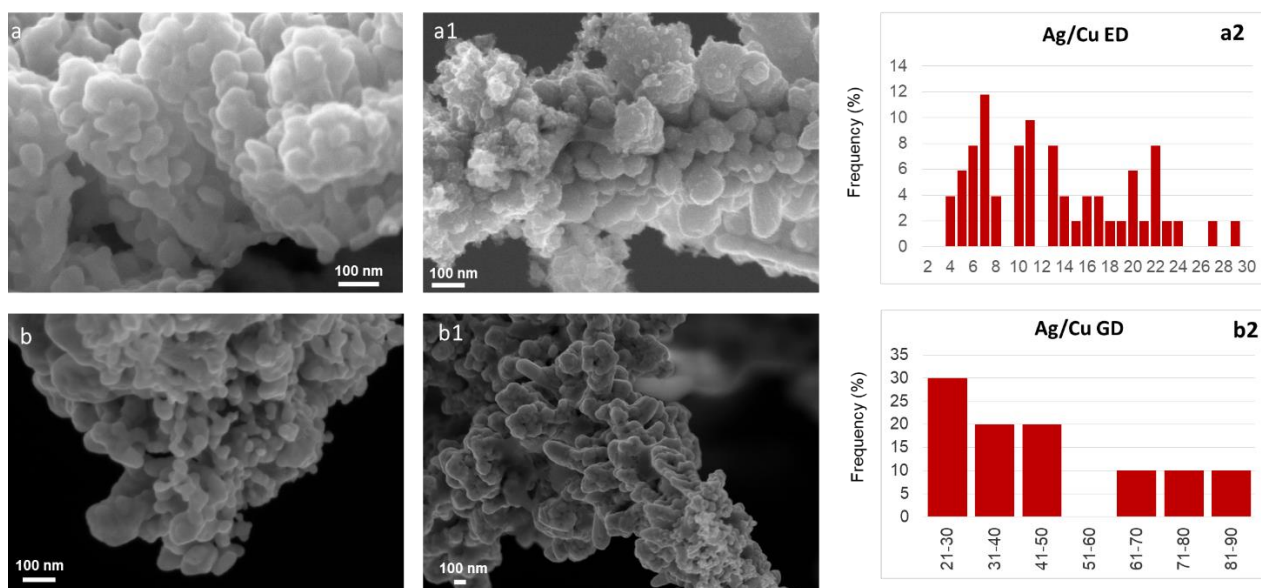


Figure 3.33. FE-SEM images of Ag/Cu ED (a, a1) and GD (b, b1) electrodes after catalytic tests. Particles distribution obtained by TEM of electrodeposited (a2) and displaced (b2) samples.

XPS measurements of Ag/Cu ED sample, performed after electrolysis, confirm the stability of Ag and the presence of Cu metallic and oxide species (Figure 3.34b). Also observed in fresh sample, two different contributions are observed, from Cu 3d and Ag 4d, respectively. The results of measurements suggest a Cu enrichment of foam surface after reaction, due to the segregation of the copper from the bulk to surface.

EDS/STEM analyses of spent samples (Fig. 3.34c, d) confirm a Cu-enrichment of Ag coating, albeit this behavior is not homogeneous. Namely, it seems that the composition of big and rounded particles remains unaltered.

It should be noted that the characterization of the Ag/Cu ED catalyst after the first LSV in borate electrolyte reveals the disappearing of XRD patterns of copper oxide (Figure 3.35a), as also the Cu enrichment was observed from EDS/STEM (Figure 3.35b).

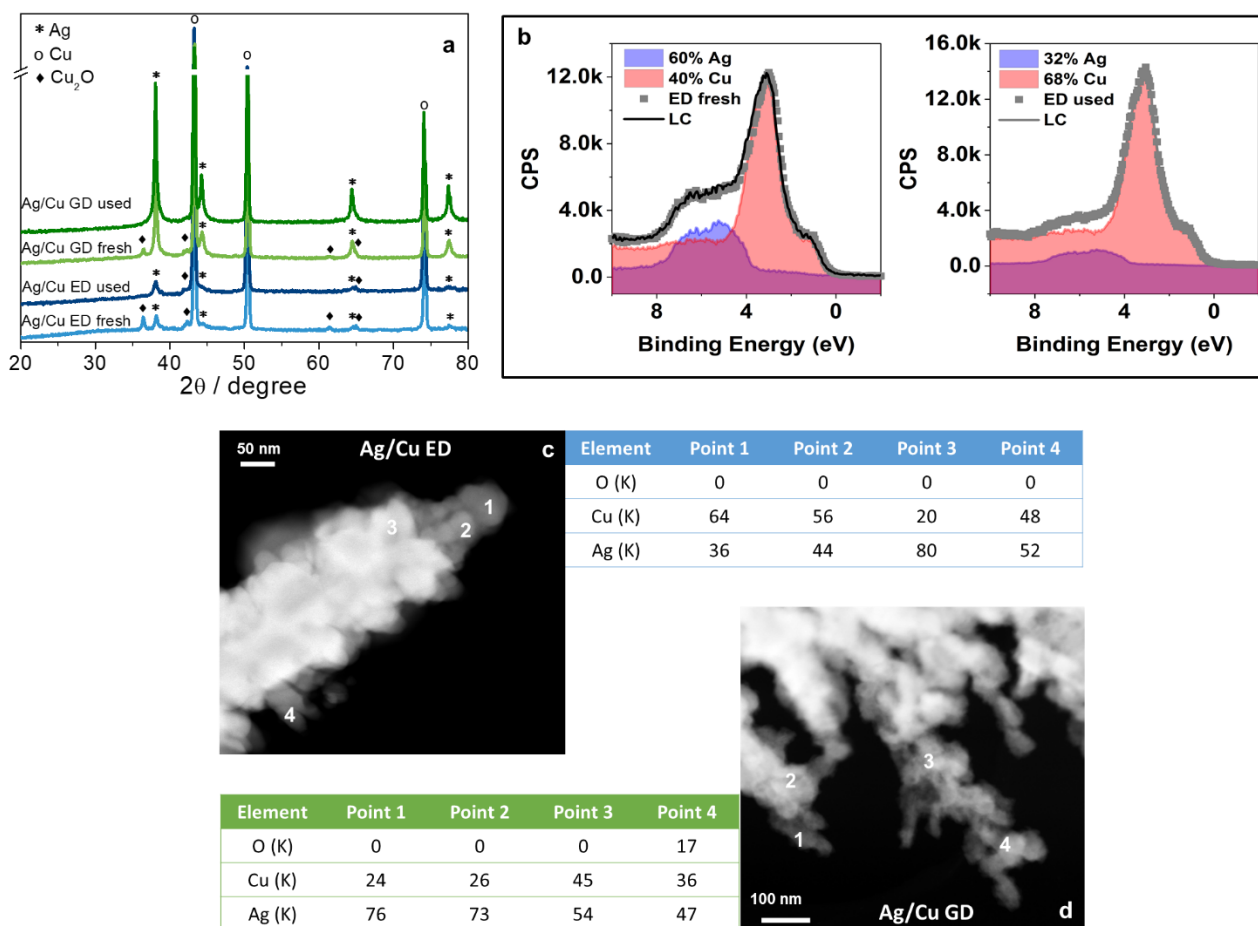


Figure 3.34. XRD spectra of fresh and used Ag/Cu foams (a); Valence band measurements of the Cu 3d and Ag 4d of the fresh and spent (b) Ag/Cu ED sample. HAADF/STEM images and EDS analyses of Ag/Cu ED (c – blue table) and Ag/Cu GD (d – green table) spent catalysts.

The changes in the composition of the coating, could be explained considering the Cu dissolution and reprecipitation⁹¹ and/or the migration of Cu. ICP analyses of the electrolytic solutions, after the first LSV and after electrolyses, confirm the presence of Cu in the electrolytic solution. The dissolution and subsequent electrodeposition of Cu^{2+} in the solution could take place, like during the preparation of the samples by electrodeposition and/or the migration of Cu.

The second mechanism considers the oxidation of Cu,^{75,92} which occurs when the electrode is exposed to the air, but also after immersion in the basic electrolyte. Both phenomena have reported to occur during the course of CO_2 reduction processes.^{93,94}

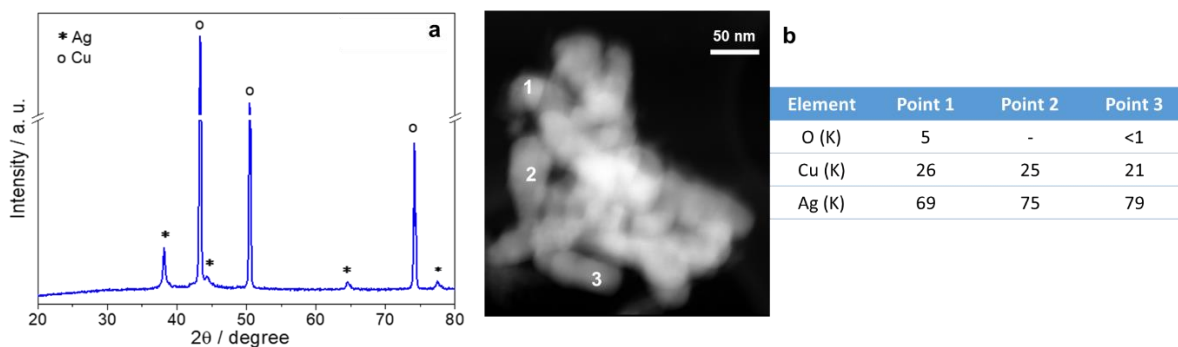


Figure 3.35. XRD (a) and HAADF/STEM images and EDS analyses (b) of Ag/Cu ED foam after first LSV in borate buffer.

3.5. Conclusions

Combining Ag nanostructuring, by electrodeposition or galvanic displacement, and Cu open-cell foams allow to synthesize an active and selective electrode for the electrochemical hydrogenation of HMF electrolytes to BHMF in basic media. The nanostructuring further increases the electroactive surface area of Cu and Ag foams, enhancing the mass and charge transfer.

The electrocatalysts, regardless the deposition method, are made by bimetallic AgCu (not alloyed) nanoparticles, though with different shape (nanoparticles or dendrites), forming a coating highly stabilized on the Cu support. This interaction allows a high electrical conductivity between the coating and the support providing a synergic activity of well dispersed Ag and Cu active sites.

These features favour the kinetics in the HER and HMF reduction reactions and the selectivity in the conversion of low concentrated HMF solutions, largely increasing the productivity in comparison to their 2D foil counterpart. Nevertheless, the enhanced properties of Ag/Cu foams are not enough to provide total selectivity when more concentrated HMF solutions are tested. Indeed, a selectivity drop occurs by increasing the HMF concentration, primarily due to a radical mechanism forming the hydrofuroin by-product.

Regarding the deposition method, the higher Ag loading and the hierarchical porosity of dendrites of Ag/Cu GD sample do not enhance the selective conversion of 0.05 M HMF to BHMF; nevertheless, a lower selectivity drop is recorded in 0.10 M HMF solution and a higher productivity is achieved in concentrated solutions, compared to Ag/Cu ED sample, thanks to the shorter reaction times.

The stability of the electrocatalytic activity of both electrodeposited and galvanic displaced samples is demonstrated by a three-cycle reaction. The current density exchanged is modified during the electrolyses and a longer time is required to accumulate the charge; nevertheless, the catalytic performance is not affected, with conversion and selectivity unaltered during the cycle. However, the longer time of reaction provoke a decrease of productivities.

The post-reaction characterization confirms the stability of the catalysts; the coating is well-adhered, without detachment of active phase, however the sintering of the nanoparticles and most importantly the enrichment of the catalyst surface in Cu occur. These results indicate that the system is modified during reduction conditions in basic media and that the identification of the real active species is not an easy task and needs for future in situ measurements.

4. Glucose as Platform Molecule

Glucose ($C_6H_{12}O_6$) is a simple sugar that contains six carbon atoms with an aldehyde group on C1, it is therefore referred to as an aldohexose. This molecule can exist in both open-chain and ring form. In aqueous solutions the acyclic structure rapidly cyclizes to form a six-membered cyclic hemiacetal (called glucopyranose) via an acid-catalyzed hydrolysis, the process is known as mutarotation. In these rings, each carbon is linked to a hydroxyl side group except for the fifth atom, which links to a sixth carbon atom outside the ring, forming a CH_2OH group. The cyclic and acyclic forms are in equilibrium and at $pH = 7$ the cyclic form is predominant. Depending on the cis-trans arrangement of the hydroxyl group attached to C1 two cyclic glucoses can be made, distinguished into α and β anomers and their isomeric ratio is strongly affected by pH , temperature and the coexisting ions (Figure 4.1).⁹⁵

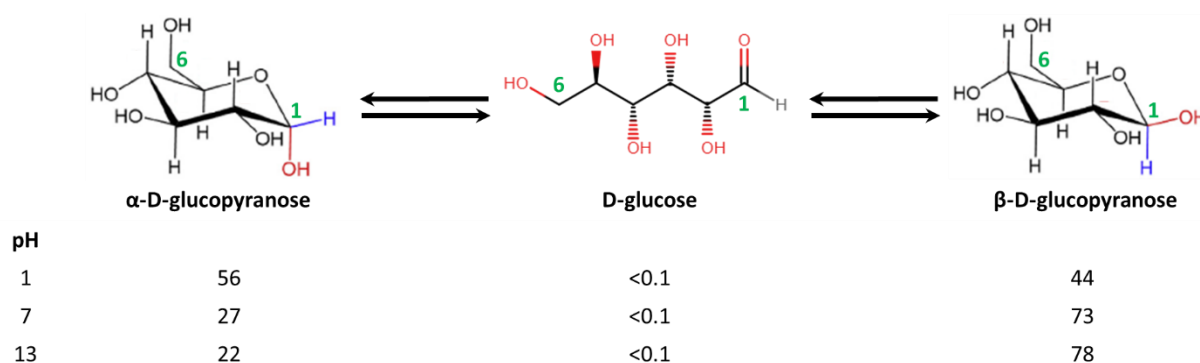


Figure 4.1. Structure of the acyclic and cyclic forms from glucose mutarotation. The numbers below represent the ratio in of aqueous glucose solution, at equilibrium, at different pH .

Currently, glucose is produced via enzymatic or acid/base-catalysed hydrolysis of biomass (in particular, cellulose and starch).⁹⁶ It is a key bio-based platform molecule for various biomass conversions, ranging from fermentations to bioethanol for fuels, to dehydrations to polymer precursors (Fig. 4.2).

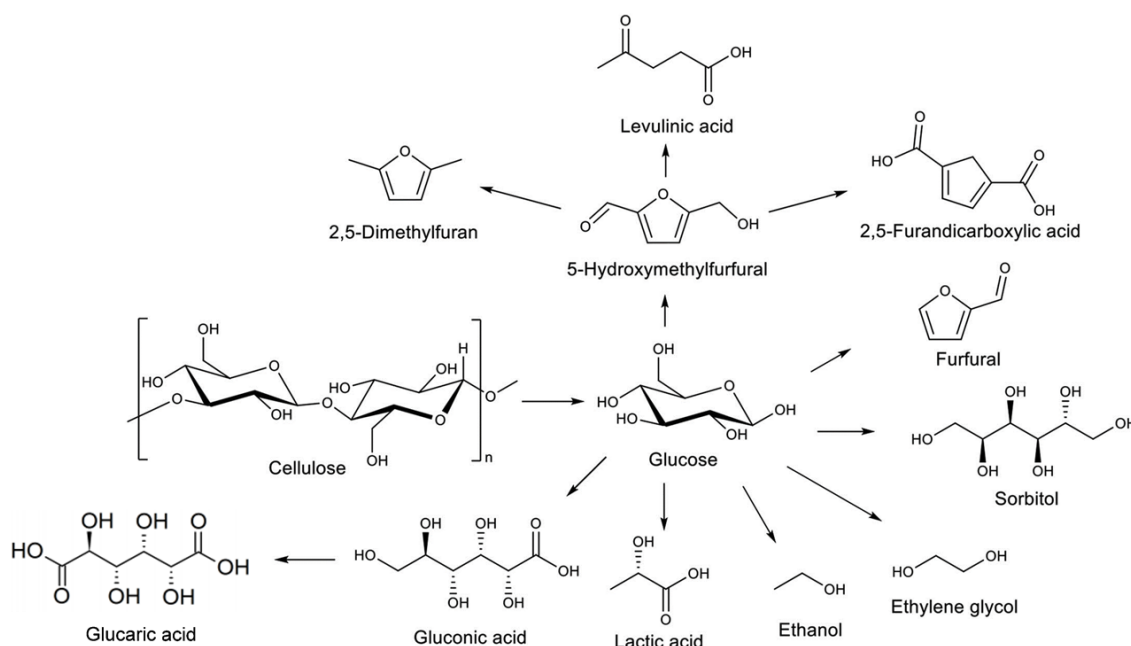


Figure 4.2. Bio-based chemicals obtained from glucose

4.1. Electrochemical Conversion of Glucose

The electrochemical conversion (reduction or oxidation) of glucose was largely studied, in the past, for the development of sensors to detect and analyse the amount of glucose in human blood, as well as to generate power (direct glucose fuel cells); but, recently, it has been gaining interest for the production of chemicals and commodities useful in the food, drugs and cosmetics field.

The electrochemical reduction of saccharides has been studied extensively since the early 1900s and, in particular, most of the efforts have been focused towards the electroreduction of D-glucose to sorbitol (Figure 4.3), the corresponding alditol, because it is a promising platform polyol used as an additive in food, drugs, cosmetics, and various chemicals including vitamin C.^{97,98} This process was previously reported as industrial scale using a lead cathode until 1950, and then totally replaced by the catalytic hydrogenation route because more cost-effective.^{97,99} However, the latter process requires high temperature and pressures, therefore, the development of a more sustainable way is being sought again.⁹⁸

Studies conducted in the first 50 years of the twentieth century reported the successful electrochemical transformation of D-glucose and other sugars to the corresponding alditols, in neutral medium (Na_2SO_4), firstly using a Hg cathode and then an amalgamated Pb cathode, investigating the influence of temperature, initial concentration and pH. Due to isomerisation equilibrium between glucose, fructose and mannose, also the formation of mannitol was reported, however, with low concentration of NaOH (2.5 mM), no mannitol was generated and 59% yield of sorbitol was obtained.

In a commercial application, a range of undesired by-products were also present, depending on the reaction conditions. In weakly alkaline medium (pH = 7–10) and temperature below to 30°C, D-mannitol (1%) and 2-deoxysorbitol (43, 5%) could be isolated; in strongly alkaline conditions (pH = 10 – 13) a more complex mixture was reported.⁹⁸

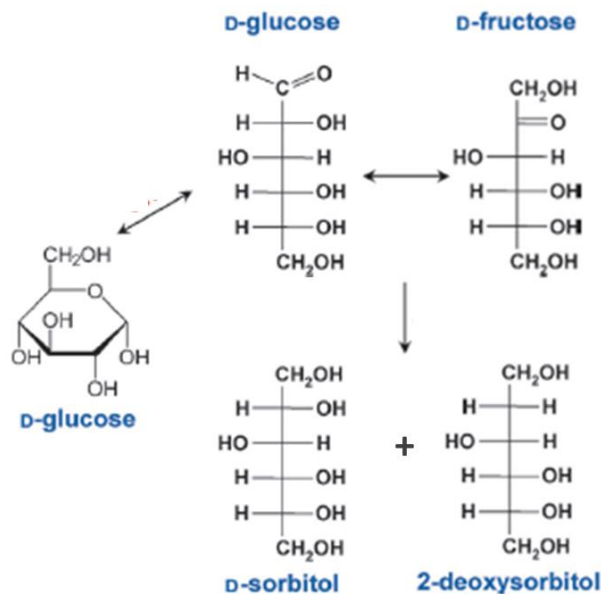


Figure 4.3. Electrochemical reduction of glucose to sorbitol and 2-deoxysorbitol.

The most commonly used metals for the electrochemical reduction of glucose are the metals which suppress the hydrogen evolution reaction (HER),^{97,98} Kwon et al. investigated several pure metal electrodes, for the production of sorbitol or 2-deoxysorbitol, with glucose 0.1 M in 0.1 M Na₂SO₄. Tested metal catalysts are divided into three groups based on the reaction products from glucose reduction:⁹⁷

- The first group is composed by transition metals (Fe, Co, Ni, Cu, Pd, Au, Ag and Al), which convert glucose to sorbitol, but also showed activity for HER. Most of these metals developed a lower reduction current in presence of glucose, compared to the reduction current in the blank solution. Au and Cu exception to this trend, developing the higher current in presence of glucose and showing the highest yield in sorbitol.
- The second group is essentially composed by post-transition metals (Zn, Cd, In, Sn, Sb, Pb, and Bi), which produce sorbitol and 2-deoxysorbitol. These metals are typically poor HER catalysts, therefore, applying a higher overpotential or cathodic current result in a higher glucose conversion and products yield. The formation of sorbitol was highest on Pb, while Sn electrode had the highest selectivity towards 2-deoxysorbitol.
- The third group include Ti, V, Cr, Mn, Zr, Nb, Mo, Hf, Ta, W, Re, Ru, Rh, Ir, and Pt. These metals are substantially inactive for glucose hydrogenation.

Acidic reaction condition (0.5 M H₂SO₄) unfavour the process, even in the presence Co, Pb or Cd, active in neutral medium. Hence, the presence of OH⁻ species is necessary, nevertheless, the use of strong alkaline media promotes the isomerisation of glucose to fructose and mannose, and consequently the formation of various side products.^{97,99}

4.2. Glucose Oxidation Reaction

The oxidation of carbohydrates, and particularly glucose, has been a very active field of research for the last fifty years and it is still intensively studied, for the production of carboxylic acids.

In particular, Gluconic Acid (GO) and Glucaric Acid (GA), and their alkali salts, are two important value-added commodities employed as additives in pharmaceutical, cosmetics, textile, building and food industries and as metal complexation agents;^{35,100,101} moreover, GO is the intermediate for GA production, which is a key platform molecule for the production of adipic acid, conventionally obtained from fossil raw materials, bio-polymers and biodegradable detergents.^{101,102}

Chemical oxidation processes currently require the use of stoichiometric strong and toxic oxidizing agents, such as nitric acid and nitrogen dioxide;^{103,104} with the aim to develop the catalytic process, noble metal-based catalysts can be employed to obtain efficient and selective glucose oxidation, under O₂/air pressure up to 50 bars and 40 – 200 °C.^{102,105,106}

There are, however, far fewer studies on the electrochemical transformation of glucose into chemicals.

Most of the existing literature is focusing on the development of non-enzymatic glucose sensors to help for diabetic treatment, or as a reagent for the biological direct glucose fuel cells (DGFCs),^{107,108} in these studies the structure of the products obtained is generally not investigated.⁹⁸

4.2.1. Non-enzymatic Glucose Sensors

Non-enzymatic sensors use the direct oxidation of glucose to D-glucono- δ -lactone (Fig. 4.4a), to allow the determination of oxidation current and, hence, glucose levels.

Several non-enzymatic systems were studied using different compounds based on: noble and non-noble metals (Pt, Au, Pd, Cu, Ni, Ag, Fe, Co), metal oxides and hydroxides (RuO₂, Ni(OH)₂, MnO₂), alloys (PtPb, PtRu) and carbon-based materials (reduced graphene oxide, carbon nanotubes). Nevertheless, despite decades of research, several problems as the lack of selectivity, the slow kinetics of glucose oxidation, the fouling of the electrode and the limited number of systems suitable at physiological pH, have prevented the practical application of these systems.^{95,108,109}

The mechanism for the oxidation of glucose was firstly proposed by Pletcher that suggested a concerted step, i.e. the process of hydrogen abstraction occurs simultaneously to the adsorption of the

organic species (Fig. 4.4b). However, this mechanism did not consider the oxidative role of hydroxyl radicals. Burke proposed the ‘Incipient Hydrrous Oxide Adatom Mediator’ model (IHOAM) that consider the formation of an OH_{ads} layer on catalyst surface that mediate oxidation. This was already well known for the oxidation of organic compounds.^{95,108,109}

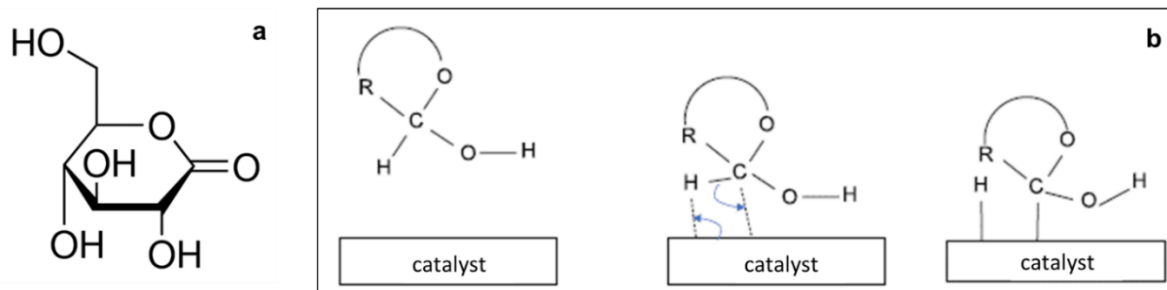


Figure 4.4. Structure of D-glucono- δ -lactone (a); concerted oxidation mechanism of glucose proposed by Pletcher (b).

4.2.2. Direct Glucose Fuel Cells (DGFCs)

Fuel cells directly convert chemical energy into electrical energy through electrochemical reactions and were considered as one of the most promising technologies for the clean energy of the future. Direct glucose fuel cell (DGFC) usually operates with the oxidation of glucose on a Pt anode and the reduction of oxygen at the cathode. Theoretically, DGFCs exploit the complete electro-oxidation of glucose to carbon dioxide and water, which releases 24 electrons; nevertheless, glucose is quickly oxidised to gluconic acid, yielding two electrons, but, due the Pt poisoning, the further steps are much slower and do not significantly contribute to the overall electron yield. This issue causes the development of a low current density ($<10 \text{ mA cm}^{-2}$ in most cases), which forbid wide applications of DGFC.^{110–112} It has been reported that working in alkaline media an improvement of the performances of DGFCs was observed, thanks to the enhanced kinetics of the glucose oxidation reaction in this condition. Non-Pt metals, as Au, Ag, Ni, Pd and manganese oxide based-catalysts, showed long lifetime and operational stability. Also bimetallic catalysts based on noble-metals supported on different materials were studied, as PtPd/C, PtAu/C, PdRh/C, etc.^{107,112} Chen et al. reported the use of Au particles on a nickel foam as catalyst for DGFCs in alkaline media. This catalytic system combines activity of Au with enhanced mass and electron transport properties of nickel foam.¹¹³ Also NiO is studied as one of the most promising catalyst for the electro-oxidation of glucose, and in particular, NiO on Ni foam, to take advantage of the features of metal 3D foams.¹¹²

4.2.3. Selective Electrochemical Oxidation to Gluconic and Glucaric Acids

Although this process exploits the same reaction of non-enzymatic sensors and DGFCs, they serve different purposes: in DGFCs and sensors the aim is the development of the highest possible current

density, hence the activity of the electrocatalyst is not focused on the selectivity of the process; conversely in an electrocatalytic reaction the goal is to optimize the selectivity and the productivity of the catalyst, regardless the current density developed.

Compared to the conventionally processes used to produce Gluconic and Glucaric acids, the electrochemical way represents a fully sustainable alternative route that can be performed in milder conditions, at room temperature and pressure, using water as oxygen source. This allow to prevent the use of high O₂ pressure or strong and toxic chemical oxidants.³⁴⁻³⁶

As also previously reported for DGFCs and sensors, the electrochemical oxidation of glucose is most active in alkaline solutions.^{114,115} Largeaud et al. investigated the activity of glucose for the anodic oxidation in on a Pt electrode, focusing the work on the two main dissolved anomeric forms of glucose (α - and β -glucopyranose). The very low amount of the α -anomer in basic medium makes it difficult to draw conclusions on its activity in these conditions, therefore their conclusions are based on the study in acid medium. The CVs measurements in acidic condition reveal that the β -form showed higher current density than the α -form, suggesting a much higher reactivity of the former anomer on a Pt anode, probably due to its conformation that allows a better planar interaction of the glucose molecule with the electrode surface and a more rapid reaction.⁹⁸

However, there are some critical issues that affect the process working in basic medium. Indeed, if treated with strong bases, glucose undergoes isomerization that leads to the formation of a mixture of isomers (glucose, fructose and mannose). The reaction occurs through the formation of an intermediate enediol (Fig. 4.5) and does not occur in acid because this environment destabilizes the intermediate. Being an equilibrium, the amount of glucose, fructose and mannose become constant in the final mixture, after a sufficient interval of time, and it is always obtained starting from any of these three monosaccharides.¹¹⁶

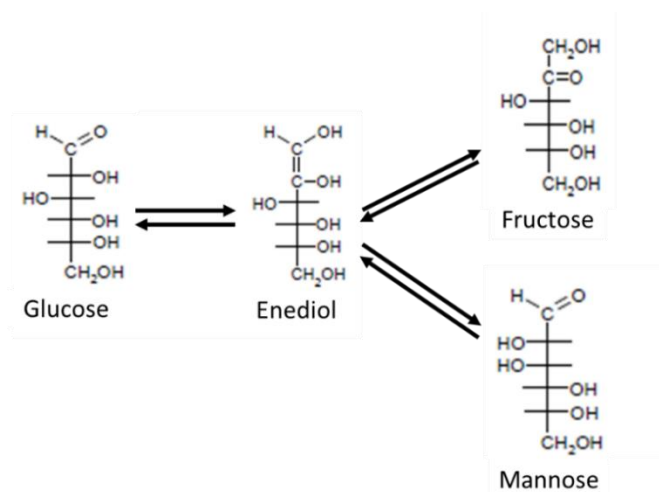


Figure 4.5. Isomerization of glucose in fructose and mannose through enediol intermediate.

Secondly, glucose is subjected to degradation with time, when dissolved in strong alkaline solutions, leads to the formation of mixtures of high and low molecular weight molecules, due the occurrence of a series of irreversible side reactions as aldolization/retroaldolization, β -elimination and benzylic rearrangement. The higher concentrations of glucose appeared to decrease the secondary reactions limiting the production of $<C_6$, instead in diluted solutions an almost complete conversion of the monosaccharides into $<C_6$ acids is obtained.¹¹⁷⁻¹²⁰

Finally, concerning specifically the selective (electro)-catalytic oxidation of glucose to gluconic and glucaric acids, the process is subjected to the loss of selectivity in presence of strong oxidant species, i.e. radicals or OH^\cdot , which limit the control of the selectivity in the oxidation of the two terminal anomeric carbons (C1 and C6) in the glucose molecule. In particular, the limiting step is the further oxidation of gluconic acid to glucaric acid with the production of C6 by-products, as keto-2-gluconic and keto-5-gluconic acids, due to the oxidation of C2 or C5 carbons, respectively; moreover, the non-selective cleavage of C-C bonds leads to the formation of several $C < 6$ carboxylic acids as glyceric acid, oxalic acid, tartaric acid, glycolic acid, formic acid, etc.^{117,121}

More recently, Ibert et al. investigated the selective transformation of D-glucose to glucaric acid using the TEMPO (2,2,6,6-tetramethyl-1-piperidinyloxy free radical) mediator, reaching the full conversion of glucose with 20% faradaic excess (i.e., the reaction was stopped after collecting 20% excess of the theoretical charge value required for full conversion), obtaining glucaric acid in poor yield and a large amount of low-molecular by-products. Particularly, one of the main by-products detected was a tricarboxylic acid (Fig. 4.6) derived from a benzylic rearrangement at the C-4, C-5, and C-6 centers via the formation of a diketone intermediate, due to the over-oxidation of the secondary alcohols of glucaric acid.^{120,122}

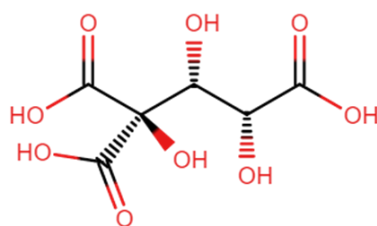


Figure 4.6. Tricarboxylic acid derived from benzylic rearrangement of glucaric acid.

However, the selectivity of electrochemical process depends on the reaction conditions, working potential or current density, and type of electrocatalysts employed. As example, Moggia et al. investigated the role of low temperature in the side reaction of electrochemical oxidation of glucose. Performing a long electrolysis of glucose 0.04 M in NaOH 0.1 M, for 65 h at 5°C, using a Pt or Au electrode, the formation of by-products was limited obtaining a total selectivity in gluconic and

glucaric acids higher than 80%; moreover, the selectivity toward one of these products can be modified by adjusting the electrochemical parameters.³³

The activity and efficiency of noble metal catalysts for glucose electro-oxidation reaction are well known from previous voltammetric studies derived from sensors and DGFCs applications.^{107,108,111,112} For instance, Kokoh et al. studied the glucose oxidation on pure Au and Pt anodes in basic medium (NaOH 0.1 M) and the effect of UPD Tl, Pb, and Bi adatoms. After long electrolysis, a 77% yield for Au and a 50% yield for Pt of gluconic acid were obtained, and glucaric acid in trace amounts. Modifying the surface of the electrode with adatoms an increase in the activity was reported with higher selectivity toward glucaric acid. In particular, Au-Pb adatom produced a significant amount of glucaric acid, and an increase in selectivity occurs when a higher potential was applied from 0.5 to 0.9 V vs RHE. However, as above reported, also degradation products were observed in small quantities.¹²¹

Bimetallic electrocatalysts were also investigated in NaOH solution (0.1 M). For instance, Rafaideen et al. recently reported the study of carbon-supported Pd_xAu_{10-x}/C for the electrochemical oxidation of glucose and xylose. It was observed that at low potential (<0.9 V vs. RHE), the activity of the catalyst increases with the increase of Au content up to 70%, with the Pd₃Au₇/C catalysts that showing the highest catalytic activity. After prolonged electrolysis of 6h at 0.4 V vs RHE, with the latter anode, 67% of glucose conversion was obtained with 87% of gluconate selectivity and very small amount of over-oxidation products could be detected.³⁴

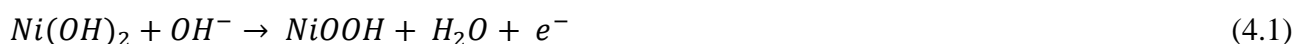
However, the scarcity and the high price of noble metals do not make the processes easily scalable, these issues encourage researchers to study alternative non-noble electrocatalysts.

Nickel is one of the most commonly used non-precious metal, largely studied for different electrochemical applications such as rechargeable batteries, supercapacitors and fuel cells. Its oxide and hydroxide forms were employed as active phase in several electro-oxidation processes (i.e ammonia and alcohol oxidation, OER, etc.)¹²³⁻¹²⁵ and, particularly, for glycerol oxidation,¹²⁶⁻¹²⁸ a C3 polyol containing three hydroxyl groups, with a molecular structure that has similarities to that of glucose.

Nickel-based electrodes have also been investigated by Parpot et al. for the electro-oxidation of monosaccharides as D-galactose and D-mannose in 0.1 M NaOH for the production of the corresponding galactonic and mannonic acids. A poor yield was obtained with the formation of various low molecular weight acids (formic, glycolic, oxalic acid), due to the C-C bond cleavage.⁹⁸

Recently, Liu et al.³⁵ proposed a NiFeO_x/Ni foam electrocatalyst, which showed a great activity and selectivity toward the electrochemical oxidation of D-glucose to gluconic and glucaric acids. The authors used the foam as a support, as a Ni source for the catalyst and to ensure a 3D structure to the electrode. Nickel open-cell foams were largely employed as support and/or catalyst for several electrochemical oxidation processes and fuel cells in alkaline media,^{129,130} to increase the surface area per unit of volume, enhance mass and electron transfer and mechanical strength.²⁵

The process developed by Liu et al. performs the electrolysis of a glucose 10 mM solution in 1M KOH as electrolyte at 1.30 V vs RHE, obtaining a 92% of gluconic and glucaric acid total yield and 87% faradaic efficiency. Moreover, Zhao et al. employed a Ni₃(BTC)₂/Ni foam electrocatalyst, to selectively convert sodium gluconate 1.0 M into glucaric acid in alkaline media (KOH 8.0 M).¹³¹ In both cases, the authors ascribed the catalytic activity to in-situ generated oxy-hydroxides species on surface. Many studies usually reported that the oxidation of organic species as glucose is mediated by the oxyhydroxide of Ni (III), the oxidized partner of the redox pair Ni(OH)₂/NiOOH (or Ni²⁺/Ni³⁺). These species are formed by a change in the oxidation state of Ni on the electrode surface, following the equation 4.1 in alkaline medium:^{132,133}



Electrodeposition of Ni(OH)₂ from nitrate solution and subsequent immersion into an alkaline electrolyte leads to the formation of two crystallographic species: the hydrated form, named as α-Ni(OH)₂, less crystalline and with water molecules intercalated between the layers of the Ni(OH)₂ crystal structure, and the anhydrous one, called β-Ni(OH)₂, with a structure of nickel octahedrally coordinated to eight oxygen atoms. Usually, β-Ni(OH)₂ is indicated as the catalytic active one, due to its high stability in strong alkaline electrolyte. During electrochemical oxidation processes α- and β-Ni(OH)₂ are transformed into γ-NiOOH and β-NiOOH, respectively, in a reversible process. It should be noted that the Ni(OH)₂ deposited phase contains the two species α- and β- in non-stoichiometric amount. When the electrodes is subjected to a cycles of variation of the potential in strong alkaline environment, an ageing of the material occurs, characterized by the shift of the potentials towards more anodic values, that indicates an enrichment of the β-Ni(OH)₂ species into the material.^{133,134}

The oxidation of all organic molecules (glucose in our case) at the Ni electrode takes place immediately after the formation of the Ni(III) species by hydrogen abstraction from C1 of glucose, forming a radical intermediate, with the regeneration of Ni(OH)₂; then, hydroxyl anions in the solution quickly react with the radical intermediate to form gluconolactone, which is subsequently hydrolyzed to gluconic acid in basic medium.¹⁰⁹

In this work, with the aim to favour the formation of NiOOH species on the Ni foam surface different procedures were used. Calcination of foams was carried out to produce a layer of NiO; while, electrodeposition and electro-base generation methods were performed to produce a layer of Ni particles or Ni(OH)₂, respectively.

4.3. Experimental Section

4.3.1. Materials and Chemicals

Ni commercial foam was supplied by Alantum. The chemicals used were sodium hydroxide ($\geq 98\%$, Sigma-Aldrich), nickel nitrate hexahydrate (99.9985%, Alfa Aesar), ammonium chloride ($>99.5\%$, Sigma-Aldrich), nickel chloride hexahydrate (Sigma-Aldrich), D-glucose anhydrous (99%, Alfa Aesar), D-gluconic acid sodium salt (97%, Sigma-Aldrich), D-fructose (99%, Alfa Aesar).

Analytical standard used for High Performance Liquid Chromatography (HPLC) analysis were: D-saccharic acid potassium salt (glucaric acid, 98%, Sigma-Aldrich), D-glucuronic acid ($>98\%$, Sigma-Aldrich), oxalic acid anhydrous (98%, Acros Organics), sodium mesoxalate monohydrate ($>98\%$, Sigma-Aldrich), D-arabinose (99%, Alfa Aesar), D-Mannose (99%, Alfa Aesar), 5-keto-D-gluconic acid potassium salt (98%, Alfa Aesar), 2-keto-D-gluconic acid hemicalcium salt monohydrate (99%, Alfa Aesar), DL-tartaric acid (99%, Alfa Aesar), tartronic acid ($>97\%$, Sigma-Aldrich), glycolic acid (98%, Alfa Aesar), L-glyceric acid hemicalcium salt monohydrate ($>97\%$, Sigma-Aldrich), formic acid pure (98+%, Acros Organics). All chemicals were used without further purification. Ultrapure water, UPW, (18 M Ω *cm) was used for the preparation of all aqueous solutions.

4.3.2. Synthesis of Electrocatalysts

Foam electrodes were prepared by cutting Ni foam panels of 1.6 mm thickness and 450 μm cell size into 10 mm \times 10 mm pieces (geometric surface area 2.64 cm²). Before the use, the electrodes were cleaned by washing with 2-propanol and ultrapure water, followed by immersing in 1 M HCl for 5 min to remove surface oxides, and water to remove residual HCl.

Nickel hydroxide (Ni(OH)₂/Ni) and nickel metallic particles (Ni/Ni) on Ni foam electrodes were prepared by electrodeposition.

The deposition of a nickel hydroxide layer on the nickel foam was performed in a home-made double-compartment flow electrochemical cell, already described in the paragraph 3.3.2, using a 0.1 M solution of Ni(NO₃)₂*6H₂O and applying a potential of -1.1 V vs SCE for 200 s, with a flow rate of 2 mL min⁻¹.

The electrodeposition of Ni metallic particles on Ni foam was carried out in a single-compartment three-electrode cell (see paragraph 3.3.2 for the setup of the cell) by applying a 100 s pulse at -1.2 V vs SCE, using 25 mL of 5.0 mM NiCl₂ in NH₄Cl 0.1 M aqueous solution electrolyte, under magnetic stirring of 500 rpm. After electrodeposition, the as prepared electrodes were rinsed gently with UPW and dried overnight at 50°C. The foams were weighted before and after synthesis to determine the amount of coating deposited.

Calcined electrodes were made by calcination of Ni foam at different temperatures (500°C, 650°C) and time (1h, 12h), using a heating ramp of 10°C/min⁻¹ for all the electrodes. The as-prepared catalysts are named as NiC500-1h, NiC500-12h and NiC650-1h.

4.3.3. Electrochemical Measurements

All electrochemical experiments were controlled by a potentiostat/galvanostat Metrohm Autolab PGSTAT204, equipped with NOVA software; a Pt wires were attached to the electrodes to enable connection to the potentiostat.

A three-electrode three-compartment cell, separated by glass frits, was used to perform the measurements. Working electrodes were bare and treated foams, placed in the central compartment. Counter electrodes were Pt wires placed in the side compartments. A saturated calomel electrode (SCE) was used as reference electrode. The RE was kept in electrolytic contact with the main compartment via a Luggin capillary.

All potentials from the next section were reported vs SCE and RHE (V vs RHE = V vs SCE + 0.244 V + 0.0591pH). The cell was immersed in a thermostated water bath at 25°C. The *i*R drop, determined by current interrupt approach, for all the CVs was compensated after measurements, assuming a constant *R*_u during the scans; instead the constant-potential electrolysis were performed without compensation.

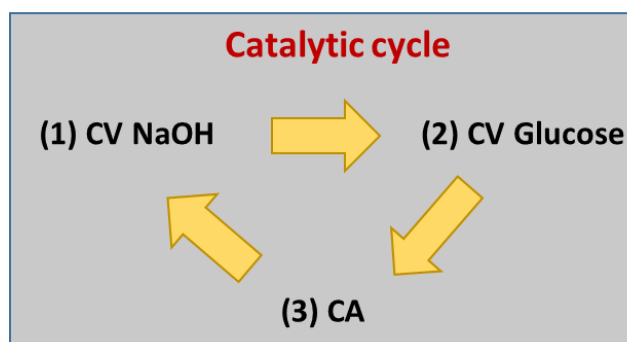
NaOH 0.05 M (pH 12.7), 0.10 M (pH 13) or 1.0 M (pH 14) aqueous electrolytes were used in both cathodic and anodic compartments. Anolyte was 25 mL of NaOH with and without D-glucose 0.01, 0.05, 0.10 and 0.50 M, Gluconate 0.005 and 0.01 M, or Fructose 0.01 M. To avoid the presence of dissolved oxygen, all the solutions were purged with N₂ before each electrochemical experiment, and a N₂ flow was kept in the open space of the cell during experiments.

Cyclic Voltammeteries (CVs) were recorded in NaOH with and without glucose, gluconate or fructose, for the electrochemical characterization of the catalysts. The potential was scanned from -0.4 to 0.8 V vs SCE at a scan rate of 5 mV s⁻¹.

Electrocatalytic oxidations were performed potentiostatically at different potentials from 0.6 to 0.9 V vs SCE (using deaerated electrolytes with different glucose, gluconate or fructose concentrations, as

above reported, and flushing N₂ in the overhead of the working electrode compartment). The experiments were performed under stirring of the solution with a magnetic bar at a rotating speed of 1000 rpm.

The catalytic cycle is composed by a sequence of CVs without and with glucose or gluconate, electrolysis at constant potential and then the first two CVs are repeated, to check for any change in the electrocatalysts after reaction. Once the first cycle was completed a new electrolysis could be immediately performed, starting a new catalytic cycle (see Scheme 4.1). This sequence was replicated for all investigated D-glucose and D-gluconate concentrations.



Scheme 4.1. Description of the catalytic cycle: after the preparation the catalyst undergoes a CV in NaOH (1), followed by a CV in NaOH+Glucose (2) and a chronoamperometry (CA) (3) in Glucose solution. After the CA, the first two CV are repeated, afterwards the cycle can stop or start again with another electrolysis.

The reactions were carried out under total conversion of reagent (glucose or gluconate), which were obtained through the transfer of the charge necessary to convert all glucose in solution to gluconic acid (through a 2 e⁻ process) or the complete conversion of gluconate to glucaric acid (through a 4 e⁻ process), assuming a 100 % Faradaic Efficiency. At the end, the solutions were collected and analysed with HPLC. The geometric surface areas of the electrodes were considered for calculating current densities.

4.3.4. Products Analyses

Quantitative analysis of the products in the electrolytes was conducted with a HPLC Agilent 1260 Infinity Series, provided with 2 columns Rezex ROA-Organic Acids H⁺ (8%) in series, operating at 80°C, equipped with an autosampler (injection volume 20 μL), a Diode-Array Detector set at 202 nm for the identification of organic acids and a refractive index detector (RID) thermostated at 40°C for the detection of monosaccharides. These columns are composed of non-polar resins consisting of styrene-divinylbenzene (SDVB) cross-linked at 8% and branched with long hydrophobic chains that end with acidic sulphonic groups (-H⁺). Sulfuric acid (H₂SO₄, 0.0025 M) was used as mobile phase with a constant flow rate of 0.5 mL min⁻¹.

Conversion, selectivity of gluconic/gluconic acid and by-products, faradaic efficiency (FE) for gluconic/gluconic acid were calculated with the following equations (4.2 – 4.4):

$$\chi_{reag}(\%) = \frac{mol_{reag\ consumed}}{mol_{reag\ initial}} \times 100 \quad (4.2)$$

$$S_{prod}(\%) = \frac{mol_{prod\ formed}}{mol_{reag\ consumed}} \times 100 \quad (4.3)$$

$$FE(\%) = \frac{mol_{prod\ formed}}{\frac{charge\ passed}{F \times ne^-}} \times 100 \quad (4.4)$$

where F is the Faraday constant; ne^- = number of electrons exchanged (2 for gluconic acid production and 6 for gluconic acid); reag = glucose, gluconate or fructose; prod = gluconic/gluconic acid or by-products.

It should be noted that, due the occurrence of isomerization of glucose, the presence of fructose was revealed in the solutions before and after reaction, therefore the amount of unreacted (consumed) glucose after electrolyses was corrected adding the amount of fructose detected.

In the chromatograms acquired, the overlap between the peaks of glucose and gluconic acid occurred on both RID and DAD detectors. However, glucose has a negligible response factor to DAD compared to gluconic acid, while the response factors to RID are of the same order of magnitude. Therefore, it was assumed that the peak visible at DAD detector can be exclusively attributed to gluconic acid. Hence, the amount of gluconic acid was easily obtained from DAD detector (eq 4.5):

$$C_{gluconic\ acid} = \frac{A_{GO,DAD}}{f_{GO,DAD}} \quad (4.5)$$

Then, its equivalent area on RID was calculated using the related response factor, $f_{GO,RID}$ (4.6):

$$A_{GO,RID} = C_{gluconic\ acid} * f_{GO,RID} \quad (4.6)$$

Finally, the area of glucose peak and therefore its residual concentration were obtained by subtracting $A_{GO,RID}$ from the peak containing the glucose+gluconic acid, A_{RID} , (eq. 4.7):

$$C_{glucose} = \frac{A_{RID} - A_{GO,RID}}{f_{glu,RID}} \quad (4.7)$$

where: C = concentration; $A_{GO,DAD}$ = area of gluconic acid peaks from DAD; $f_{GO,DAD}$ = response factor of gluconic acid at DAD; $A_{GO,RID}$ area of gluconic acid peaks from RID; $f_{GO,RID}$ = response factor of gluconic acid at RID; A_{RID} = total area of peak from RID (glucose+gluconic acid); $f_{glu,RID}$ = response factor of glucose at RID.

This procedure was validated by injecting different standard mixtures of glucose and gluconic acid at different concentrations and evaluating the difference between the sum of the individual areas and the peak recorded on the chromatogram.

Similarly, arabinose and glyceric acid showed the same retention time on chromatograms, with the negligible signal of arabinose at DAD compared to glyceric acid. Nevertheless, the procedure used above for glucose and gluconic acid did not bring any satisfactory result in this case. Hence, since the two compounds have a response of the same order of magnitude at RID, the quantification was carried out by making an average of the respective f , thus not distinguishing the contribution of the single compounds. Their concentration will be indicated below as $C_{arabinose+glyceric\ acid}$.

4.4. Study of the Selective Electrochemical Conversion of Glucose solutions with Ni foam-based electrocatalysts

4.4.1. Characterization of Ni-based Electrocatalysts

SEM images of Ni foam, shown in figure 4.7, reveal the macroporous configuration of the foam where the interconnection of the struts creates the structure of the open cell with a dimension of 450 μm (Fig. 4.7a, b). The surface of the Ni bare foam is smooth and regular (Fig. 4.7c) and the only visible structures are Ni grains delimited by grain boundaries. No particles associated with oxidised species are apparently visible, confirmed by EDS analyses, that do not reveal the presence of oxygen, and also by micro-Raman (not shown) and XRD (Figure 4.7d). The peaks observed at 44° , 52° and 75° are related to the (111)/(200)/(220) reflections, respectively, and indicate the presence of fcc Ni^0 . The sharp diffraction peaks suggest that it has a high crystallinity¹³⁵.

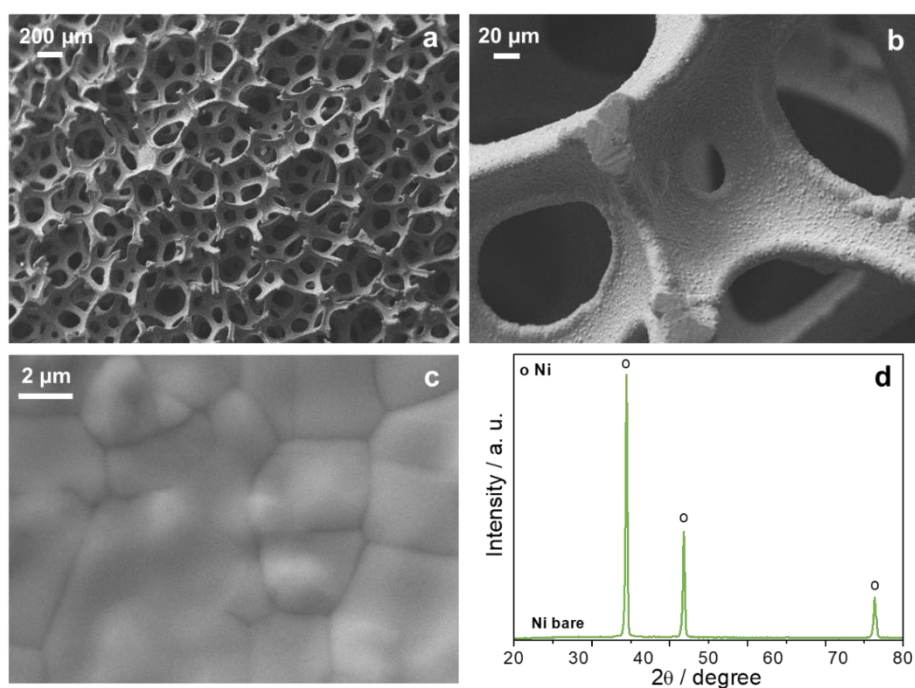


Figure 4.7. SEM images of Ni bare foam at different magnifications (a, b, c), XRD diffraction (d) of Ni bare foam.

After thermal treatment all foams increased the roughness of their surfaces (Fig. 4.8), with the growth of an oxide layer, confirmed by XRD and micro-Raman analyses (Fig. 4.9). The influence of calcination time and temperature can be observed. Indeed, after 1h at 500°C the coverage of the foams surface is very inhomogeneous (Fig. 4.8a) with a thickness of ca. 150 - 300 nm, the layer has irregular shape formed by randomly oriented particles (Fig. 4.8a1). After prolonged calcination of 12h at 500°C, no substantial differences were observed in terms of homogeneity of the layer, in fact the surface is already unevenly covered (Fig. 4.8b); however, the growth of the layer was observed with the shape that became more irregular (Fig. 4.8b1) and the layer slightly thicker (200-350 nm). Finally, increasing the calcination temperature up to 650°C the oxide layer covers the surface much more homogeneously and became thicker (400 – 500 nm) and more irregular (Fig. 4.8c, c1).

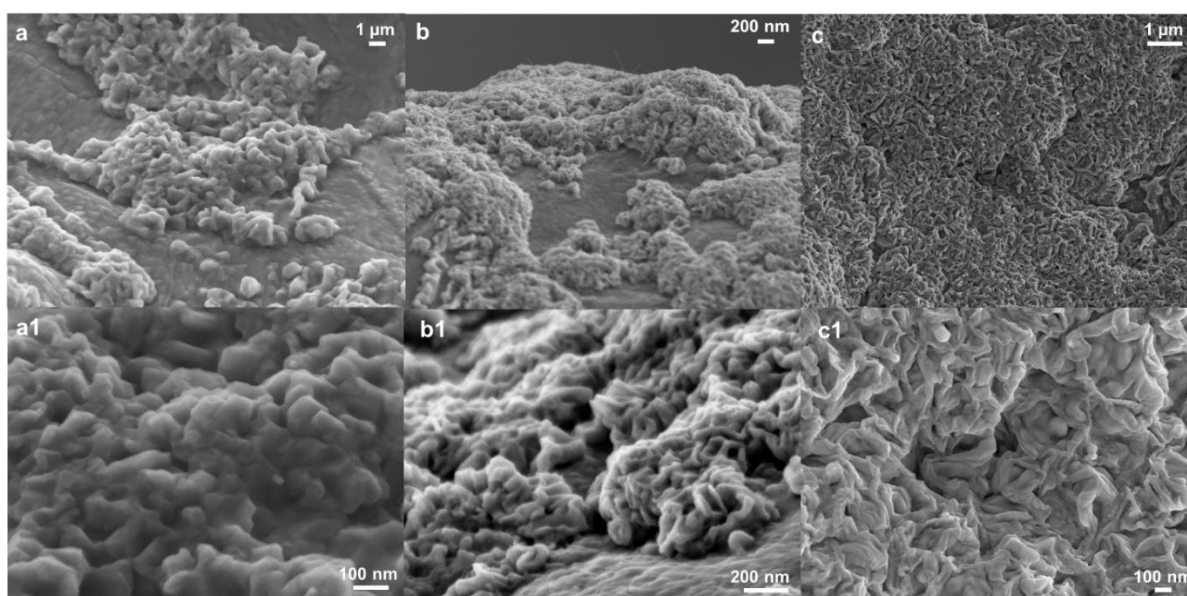


Figure 4.8. FE-SEM images of NiC500-1h (a, a1), NiC500-12h (b, b1), NiC650-1h (c, c1) electrocatalysts.

XRD patterns of the Ni electrocatalysts obtained at different calcination temperatures and time (Fig. 4.9a) show the diffraction peaks related to crystalline NiO at 37°, 43°, 63°, 75° and 79° that correspond to the (111), (200), (220), (311) and (222) planes of a fcc NiO structure.¹³⁶ It can be observed how the intensity and the sharpness of the peaks increase with the calcination temperature and time, it is due to the particle size enlargement and the increasing of NiO amount on surface, in accordance with SEM images previously observed.

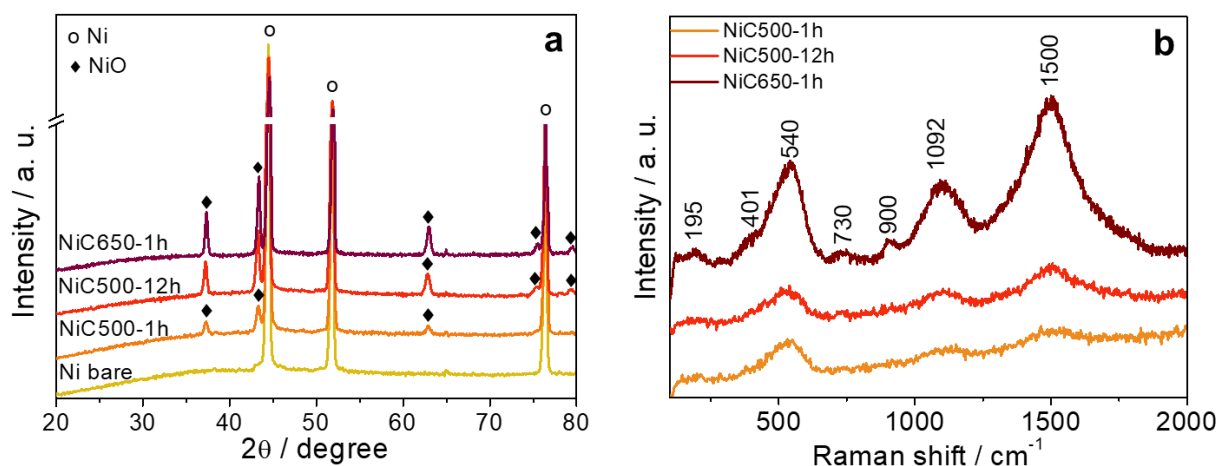


Figure 4.9. XRD patterns (a) and Raman spectra (b) of calcined foams electrocatalysts

The Raman spectra in Fig 4.9b exhibit the bands related to NiO. All the calcined samples reveal the peaks at 540, 1092 and 1500 cm^{-1} , which correspond to one-phonon (1P) longitudinal optical (LO), two-phonon (2P) LO of vibrational origin and two-magnon (2M) band associated with $\text{Ni}^{2+}-\text{O}^{2-}-\text{Ni}^{2+}$ superexchange interaction and due to an antiferromagnetic (AFM) state, respectively. The 1P-LO mode can be attributed to the disorder induced by defects, surface effects and imperfectness of the particles.¹³⁶ It should be noted that the intensity of these peaks increase with increasing the calcination temperature, this suggests a higher presence of surface defects with increasing the temperature, while the time does not seem to have a significant influence on this behaviour.

In the NiC650-1h catalyst the presence of low intensity peaks is also observed. The bands are: 195 cm^{-1} forbidden 1P scattering, 401 cm^{-1} - 1P transverse optical (TO) mode, 730 cm^{-1} - 2P TO mode, 900 cm^{-1} - 2P TO + LO mode.¹³⁶ In particular, the band at 195 cm^{-1} , not present in a perfect single crystal, is due to the presence of lattice defects and the non-stoichiometry of oxygen, that lower the symmetry around the atoms.¹³⁷

In order to enhance the formation of NiOOH species on foam surface and evaluate their contribution on catalytic activity, Ni^0 particles and $\text{Ni}(\text{OH})_2$ were deposited on Ni foams. SEM images after deposition are shown in figure 4.10.

Ni particles are homogeneously deposited on foam surface (Figure 4.10a) forming a slightly spherical agglomerated particle with a large dimensions range, from 20-30 to 140 nm and up to ca. 200 nm (Figure 4.10b). No phases related to presence of oxidised Ni were detected either by XRD (Fig. 4.11a) or by Raman (not shown).

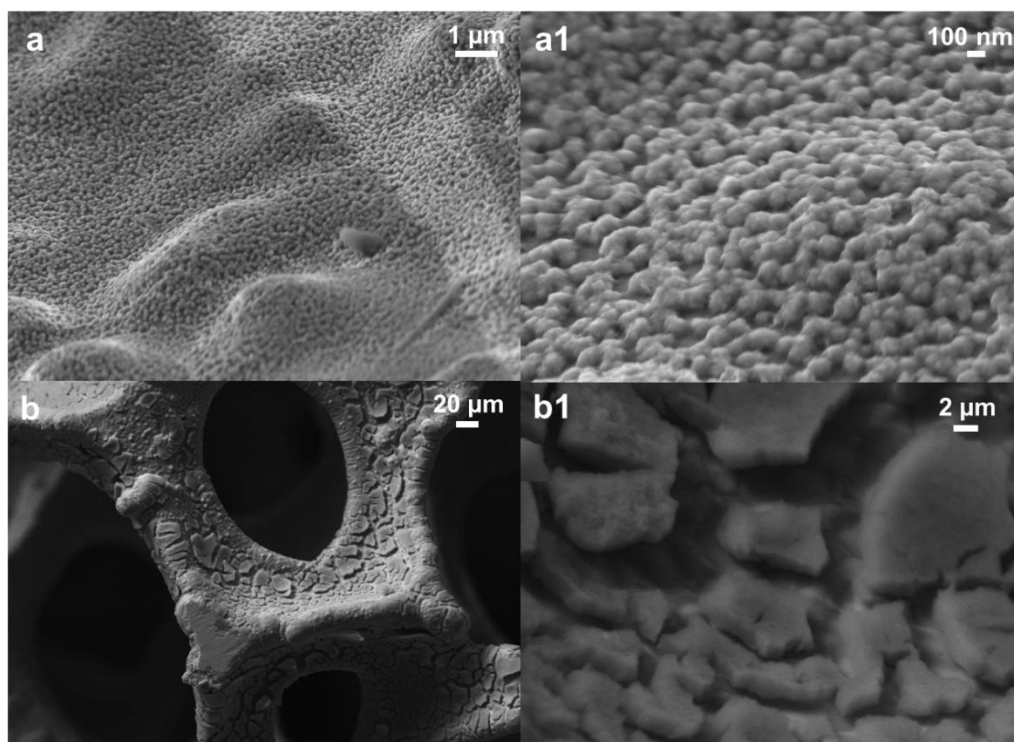


Figure 4.10. FE-SEM images of Ni particle electrodeposited on Ni foam (a, a1). SEM images of Ni hydroxide electrodeposited on Ni foam (b, b1).

After electrodeposition of $\text{Ni}(\text{OH})_2$ the formation of a thin hydroxide layer, of ca 1 - 2 μm , was obtained, which covers almost homogeneously the surface (Fig. 4.10b). However, in higher magnification images, large cracks can be observed, which are probably due to the formation of H_2 during electrodeposition or evaporation of water during drying in the oven.

As observed for Ni/Ni sample, also in this case XRD patterns do not show the presence of oxide or hydroxide crystalline phases, probably due to the low thickness of the layer; however, micro-Raman spectrum reveal the signal of Ni hydroxide in figure 4.11b.

Raman analysis showed the peaks at 440 and 463 cm^{-1} , which can be ascribed to the lattice mode of Ni hydroxide, in particular the stretching of the Ni-O(H) bond, these peaks are attributable to the β and α crystalline forms, respectively. The band at 3635 cm^{-1} is indicative of the stretching of isolated O-H in the α phase, where both the oxygen and hydrogen atoms move with respect to each other, the shoulder at 3517 can be attributable to the β phase.^{138,139}

Finally, the signal of nitrate-intercalated $\text{Ni}(\text{OH})_2$, with the most intense bands at 989 and 1045 cm^{-1} , related to the ν_1 mode and the weak peaks at 1292 cm^{-1} attributable to the ν_3 mode.^{138,140}

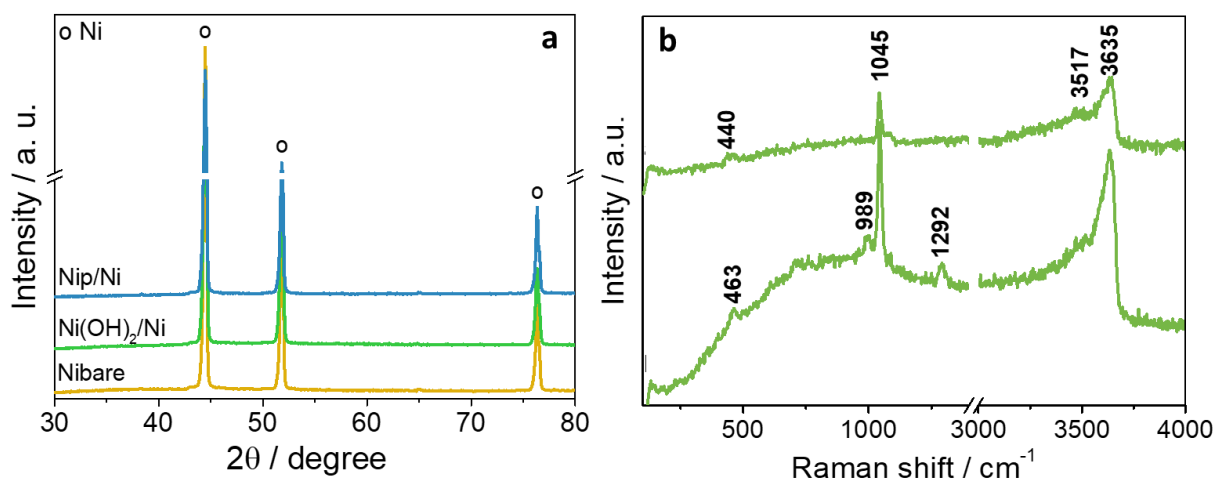


Figure 4.11. XRD patterns (a) of Ni/Ni and Ni(OH)₂/Ni compared with Nibare; Raman spectra (b) of Ni(OH)₂/Ni electrocatalysts.

4.4.2. Electrochemical Characterization of electrocatalysts

To evaluate the electrocatalytic activity of the calcined and electrodeposited Ni foams toward the selective production of gluconic and glucaric acids, the electro-oxidation of a 50 mM glucose solution in NaOH 0.1 M electrolyte was firstly investigated.

Firstly, CV experiments in NaOH 0.1 M and Glucose 50 mM + 0.1 M NaOH were performed to study the activity of the electrodes for the Oxygen Evolution Reaction (OER) and Glucose oxidation reaction (GOR), respectively (Fig. 4.12).

In Figure 4.12a and b the discharge related to OER starts between 0.5 - 0.7 V vs SCE (1.51 - 1.71 V vs RHE) for all the foams. Comparing the activity of Ni bare and calcined foams (Fig. 4.12a, a1), we can observe that the onset of the OER for Ni bare foam is at ca 0.52 V vs SCE (1.53 V vs RHE) and shifts toward more anodic potential of ca 30, 60 and 90 mV for the NiC500-1h, NiC650-1h, NiC500-12h, respectively. However, Ni bare and NiC500-1h develop a similar current density, but greater than to the two other calcined electrocatalysts.

The presence of Ni hydroxide or Ni particles deposited on surface enhance the activity of Ni foam toward the OER (Fig 4.12b, b1), in fact these foams, and in particular Ni(OH)₂/Ni, develop a very high current density (up to 50 mA cm⁻²), showing a less anodic onset of ca. 150 mV (35 mV for Ni/Ni electrode and ca 20 mA cm⁻² of current density) than Ni bare.

As expected, the activity of the electrocatalysts for OER is directly related to the formation of Ni oxide/hydroxide species, reported in the enlargement in figure 4.12a1 and 4.12b1, where the oxidation peaks of Ni²⁺ to Ni³⁺ and the reverse process in the reverse scan are shown, which occur in the potential range between 0.2 and 0.6 V vs SCE (1.21 to 1.61 V vs RHE).

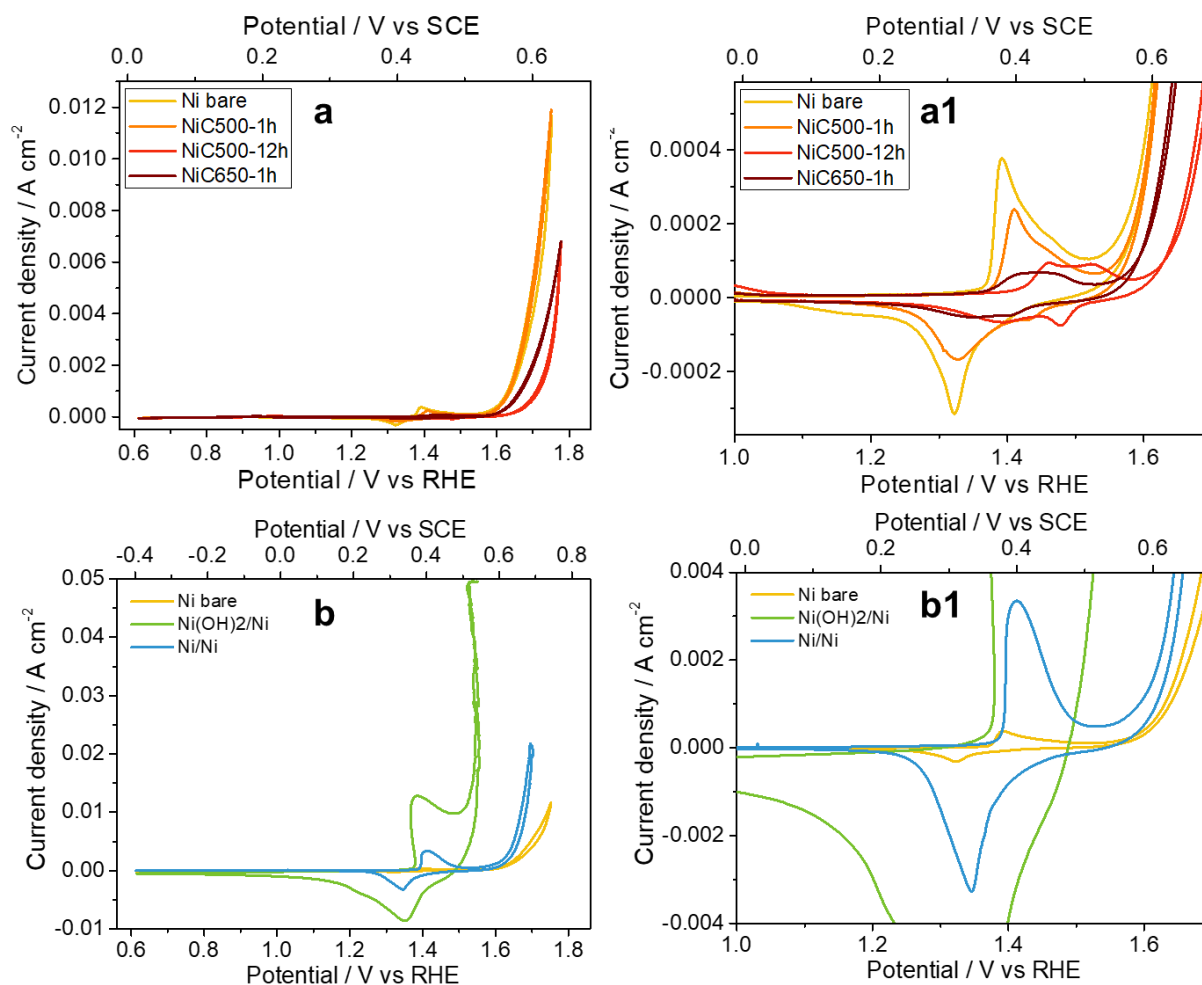


Figure 4.12. Cyclic voltammograms recorded in NaOH 0.1M over calcined foams (a, a1) and electrodeposited foams (b, b1) compared with the Ni bare electrode. Range: -0.4 to 0.8 V vs SCE (0.61 to 1.81 V vs RHE). Scan rate: 5 mV/s.

As can be seen from table 4.1, the integrated areas of the $\text{Ni}^{2+}/\text{Ni}^{3+}$ peaks can explain the trend previously observed for the OER; the electrodeposition of Ni hydroxide, but also Ni particles, on the foam surface allows to enhance the formation of the oxyhydroxide and, therefore, the OER activity of Ni foam. Conversely, the calcination has a negative effect, which worsens by increasing the time or the temperature of calcination process.

At the same time, no relation between Tafel slope, reported in table 4.1 and the two previous parameters investigated was found. The Tafel slopes are the same for both $\text{Ni}(\text{OH})_2/\text{Ni}$, Ni/Ni and NiC500-1h electrocatalysts ($67\text{-}68 \text{ mV dec}^{-1}$), meaning similar electron transfer kinetics, lower than Ni bare foam. Also in this case, a trend can be observed between calcined foam, with the Tafel slope gradually increasing for NiC650-h and NiC500-12h . However, we can consider $\text{Ni}(\text{OH})_2/\text{Ni}$ electrode as the electrocatalyst with the highest activity for OER.

Table 4.1. Tafel slopes measured from CVs recorded in NaOH 0.1 M and NaOH+Glucose 0.05 M; Area of the Ni²⁺/Ni³⁺ peaks observed in the CV in NaOH.

Sample	Slope NaOH 0.1 M / mV dec ⁻¹	Slope Glucose 0.05 M / mV dec ⁻¹	Ni ^{2+→3+} peaks area / mC cm ⁻²
Ni bare	78	138	0.031
NiC500-1h	68	130	0.019
NiC500-12h	83	136	0.013
NiC650-1h	72	133	0.009
Ni(OH) ₂ /Ni	68	118	1.397
Ni/Ni	67	115	0.240

After the addition of glucose in solution (Fig. 4.13a, b), the peak of glucose oxidation was observed at less anodic potentials than OER discharge. It should be remarked that the onsets of glucose oxidation discharge occur at less anodic potential compared to the peaks of Ni-oxyhydroxide formation and no substantial differences were detected between the onset of the different samples. No trends were observed for the calcined foams regarding the activity toward glucose oxidation, with the maximum of the current density developed that was recorded at ca 0.62 V vs SCE (1.3 V vs RHE) for all calcined foams. Remarkably, the presence of Ni hydroxide and Ni particles on Ni foam slightly increases the current density developed, with the maximum of the peak recorded at ca 40 and 90 mV lower anodic overpotential.

Despite the higher activity of the catalysts for glucose oxidation, in comparison to OER, the tafel slope values indicated a lower kinetics for the former process for all the foams, as shown in table 4.1. However, calcined foams exhibit similar slope compared to Ni bare foam, with a slight enhancement; while, the lower values exhibited from the electrodeposited samples indicating that the charge transfer occurs faster for these catalysts than Ni bare and calcined electrodes.

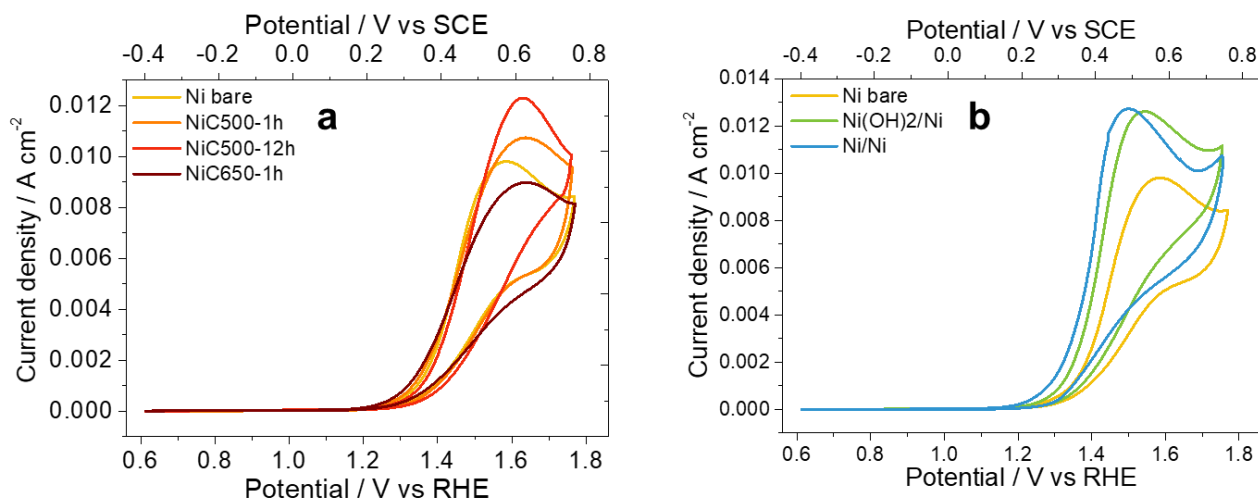


Figure 4.13. Cyclic voltammeteries recorded in Glucose 50 mM + NaOH 0.1M over calcined foams (a) and electrodeposited foams (b) compared with the Ni bare electrode. Range: -0.4 to 0.8 V vs SCE (0.61 to 1.81 V vs RHE). Scan rate: 5 mV/s.

4.4.3. Electrochemical Conversion of 50 mM Glucose in NaOH 0.1M electrolyte

After the CVs the electrolysis of a 50mM glucose solution were performed at 0.8 V vs SCE (1.81 vs RHE) over all the Ni-based electrocatalysts previously characterized. This potential was chosen from preliminary studies conducted by the research group on Ni plates.

The charge accumulated is 241.25 C, corresponding to theoretical charge required for the total and selective oxidation of 0.05M glucose to gluconic acid, considering a $2e^-$ process and 100% FE.

The results of glucose oxidation (Fig. 4.14) show that good performances are obtained for Ni bare foam, which achieves ca. 57-60% of glucose conversion and selectivity in gluconic acid (GO). The calcination has a slight beneficial effect on catalytic performances, indeed NiC500-1h improves the GO selectivity up to ca 66%. However, the increase of the calcination time or temperature reduces the activity of Ni foam, with the selectivity that decreases to ca. 51 - 52% in presence of NiC500-12h or NiC650-1h electrocatalysts.

The electrodeposition of hydroxide and also the nanostructuring of the foam with Ni particle worsen the activity and the selectivity (18%) of Ni bare, probably the increase of NiOOH on surface favours the OER instead of GOR, leading to a loss in FE (8-9%) compared to Ni bare and calcined foams (28 - 32 %).

Although the calcined foams showed a fair GO selectivity, the results indicate that all the investigated catalysts fail in the further oxidation of gluconic to glucaric acid (GA), leading to a GA selectivity < 5% and the formation of several by-products. However, it should be noted that the theoretical charge

provided during the process was not sufficient to allow the complete conversion of glucose to glucaric acid.

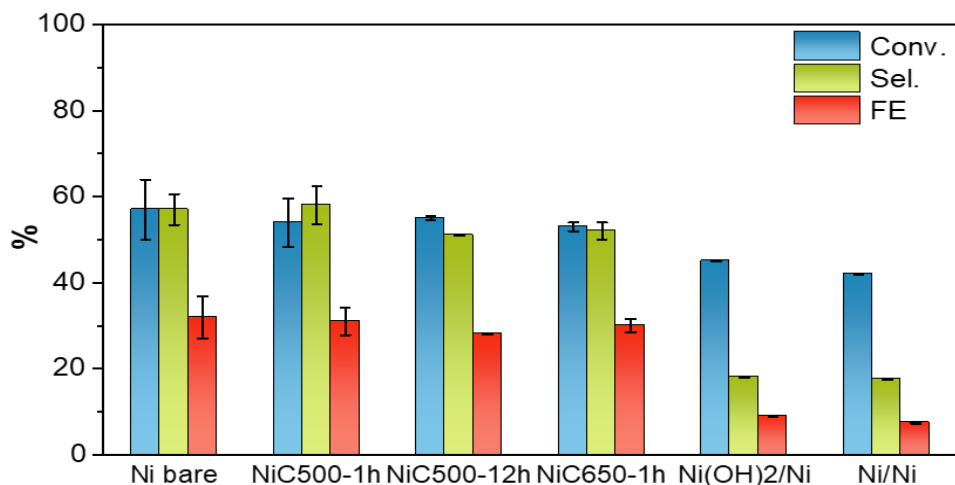


Figure 4.14. Results of electrolyses of a 0.05 M glucose solution in NaOH 0.1M performed at 0.8 V vs SCE (1.81 V vs RHE) over Ni bare, NiC500-1h, NiC500-12h, NiC650-1h, Ni(OH)₂/Ni and Ni/Ni electrocatalysts.

In order to understand how the investigated electrocatalysts affect the reaction pathways, a thorough analysis of the solutions after electrolysis was carried out, to identify and quantify the by-products formed during the reaction. The results in terms of selectivity were reported in table 4.2.

It is evident that, as reported by Kokoh et al.,¹²¹ glucose could follow two different pathways for the production of glucaric acid, passing through the formation of gluconic acid, by oxidation of C1 carbon of glucose, or glucuronic acid, by oxidation of C6 carbon of glucose (Fig. 4.15). In our case all Ni catalysts are active for the former pathway and only two catalysts (Ni bare and NiC500-1h) can follow the “glucuronic acid” way, nevertheless, the amount of glucuronic acid produced is very low. These results confirm that the electrodes are able to easily convert the C1 carbon of glucose, i.e. the aldehyde group, while they exhibit scarce or nothing activity for the selective oxidation of the alcoholic to acid group on the C6 carbon.

Unfortunately, the further oxidation of gluconic acid leads to the formation of over-oxidized species as 2KDG and 5KDG from the oxidation of C2 or C5 carbon, respectively. However, no substantial differences were reported in 2KDG selectivity, while low amounts of 5KDG are only produced on electrodeposited catalyst.

Table 4.2. Selectivity of by-products formed during the electrolyses of glucose 50mM solution at 0.8V vs SCE (1.81 V vs RHE) over the investigated Ni-based electrocatalysts.

Selectivity (%)						
Compound	Ni bare	NiC500-1h	NiC500-12h	NiC650-1h	Ni/Ni	Ni(OH)₂
Gluconic Ac.	53-59	56-66	51	48-52	17	18
Glucaric Ac.	1-3	2-5	4-7	1-2	3	3
Glucuronic Ac.	<1	0-2	-	-	-	-
Glycolic Ac.	2-4	1-2	2,5-3,5	1-3	6	5
Tartronic Ac.	<1	<1	<1	<1	<1	<1
Tartaric Ac.	<1	<1	<1	1-2	<1	<1
Oxalic Ac.	<1	1-3	1,5-2,5	<2	2	2
Lactic Ac.	1-2	1-4	2-3	<2	3	<1
2-keto-D-gluconic Ac. (2KDG)	4-5	0-3	4-5	3-4	4	3
5-keto-D-gluconic Ac. 5KDG	-	-	-	-	<1	1,5
Arabinose + Glyceric Ac.	6-7	3-7	13-14	5-7	27	14
Formic Ac.	6-8	4-9	10-11	7-10	27	24
Mesoxalic Ac.	<1	<1	-	<1	<1	<1
Total Sel.	~85	~96	~96	~81	~92	~71

A secondary compound produced in high yield is formic acid, obtained by decarboxylation processes. Interestingly, similar selectivity was reported for Arabinose/glyceric acid and formic acid, with the exception for the Ni(OH)₂/Ni catalyst. We can suppose that a secondary pathway can involve the direct oxidation of glucose to obtain arabinose and formaldehyde (not detected) quickly oxidised to formic acid (Fig. 4.16).

However, it must be emphasized that the impossibility of separating the real contribution of glyceric acid and arabinose makes it difficult to precisely define the real reaction path.

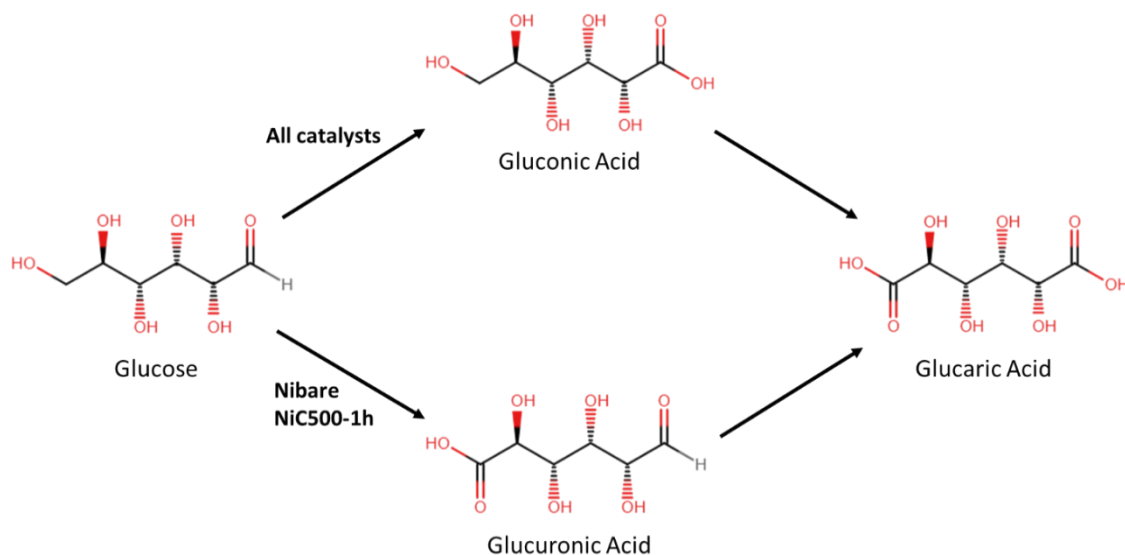


Figure 4.15. Reaction pathways for the conversion of glucose to Glucaric acid.

In fact, another reaction mechanism regards the formation of C4 – C2 by products with the formation of tartaric acid, glycolic and glyceric acids, oxalic acid, etc. until formic acid. It should be noted that these compounds do not necessarily derive from the electrocatalytic oxidation, but their production can be due to the chemical alkaline degradation of glucose or gluconic and glucuronic acid, through β -elimination and C-C cleavage/retro aldol processes^{121,141}.

Finally, a consideration on the carbon balance (expressed as total selectivity), that is below 100%. All the investigated catalysts has a carbon loss between 5 and 15% except NiC500-12h and especially Ni(OH)₂/Ni (ca. 30%). The carbon loss of the electrodes can be explained by considering that some products observed in the chromatograms have not yet been identified. Furthermore, there is the possibility that due the large amount of formic acid released, a part of it has formed CO₂, which it was not possible to detect and identify.

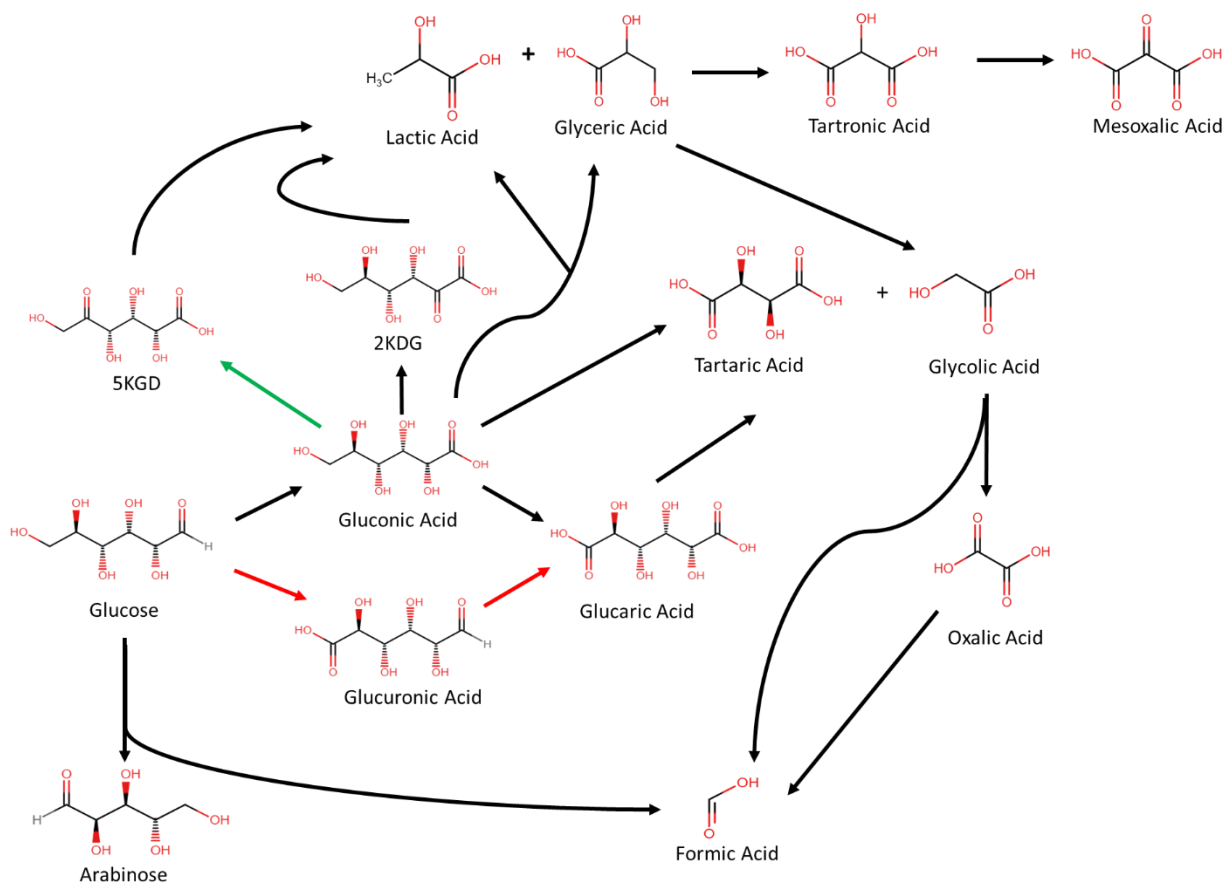


Figure 4.16. Reaction mechanism proposed for the by-products formation from the electrochemical oxidation of a 50 mM glucose solution in NaOH 0.1 M, over the Ni based catalysts investigated, at 0.8 V vs SCE (1.81 V vs RHE). Green arrow, pathways followed only by Ni/Ni and Ni(OH)₂/Ni electrode; Red arrow, secondary mechanism for glucoaric acid production exhibited by Nibare and NiC500-1h.

4.4.4. Effect of charge passed

In the next paragraphs different reaction parameters will be examined, studying how their variation influences the activity of the catalysts. Considering that NiC500-1h has shown the most promising results, only this catalyst will be further investigated.

Firstly, the effect of charge passed (or reaction time) during the electrolysis over a NiC500-1h sample was investigated. Aliquots of glucose 0.05 M in NaOH 0.10 M solutions (ca. 0.6 - 0.7 mL) were withdrawn with a syringe, assuming that the composition of the solution is homogeneous thanks to stirring. The withdrawals are set at certain amount of charge accumulated: 50, 100, 200, and 241 C. The results are shown in table 4.3.

As expected, the conversion of glucose increases with the charge. The selectivity towards gluconic acid shows a rapid increase already after 100 C passed, remaining relatively stable over time. The

selectivity in GA also increases during the electrolysis, however the maximum reached at 241C is very low.

Table 4.3. Evolution of glucose conversion, GO and by-products selectivity during the electrolyses of glucose 50mM solution at 0.8V vs SCE (1.81 V vs RHE) over the investigated Ni-based electrocatalysts.

Compounds	Charge (C)			
	50	100	200	241
Glucose Conv.	22	28	53	54
Gluconic Ac.	38	56	50	56-66
Glucaric Ac.	1.4	1.6	2.3	2-5
Glucuronic Ac.	-	-	-	0-2
Glycolic Ac.	1.4	2.5	0.8	1-2
Tartronic Ac.	0	0	0	<1
Tartaric Ac.	<1	<1	1	<1
Oxalic Ac.	<1	1.8	2	1-3
Lactic Ac.	1.8	3.3	2	1-4
2-keto-D-gluconic Ac. (2KDG)	3.2	4.4	4.3	0-3
5-keto-D-gluconic Ac. 5KDG	-	-	-	-
Arabinose + Glyceric Ac.	10	15	11	3-7
Formic Ac.	5	7.6	7	4-9
Mesoxalic Ac.	<1	1.3	1	<1
Total Sel.	~62	~95	~82	~96

It can be observed how the selectivity in the by-products decreases over time, with the increase of the selectivity in GO. The production of lower molecular weight molecules is higher at short time, reaching the maximum after 100 C. The results of electrolysis suggest that, in addition to the oxidation

of C1, the breaking of the C3-C4 bond of glucose or gluconic acid occurs, probably through a retro aldol process or C-C cleavage, with the formation of glyceric, lactic, glycolic and formic acids.

We can suppose that, initially, the signal associated with arabinose/glyceric acid is mostly composed by the latter, whose production decreases over long reaction times, forming formic acid. While the formation of arabinose could be low and about stable over time.

The mechanism seems to be consistent with what is reported in the figure 4.3. It should be noted that the low total selectivity reported after 50 C passed indicate the presence of other by-products not identified yet.

To understand how the efficiency of the process changes over time, the required effective charge to achieve the glucose conversion, experimentally observed for each step, was calculated.

Initially, glucose is efficiently converted, indeed after 50 C the ratio between the effective and the theoretical charge is ca. 1. Subsequently, there is a marked reduction in efficiency over time, passing from about 0.67 after 100 C to about 0.61 at the end of the reaction. This behaviour suggests that during the time the higher occurrence of OER reduces the efficiency of the glucose oxidation. Indeed, considering the reduction of over-oxidized products and the increase in GO and GA selectivity, we can suppose that most of the charge is lost due to the effect of the OER that produces gaseous O₂.

4.4.5. Effect of glucose concentration

The effect of glucose concentration was investigated using the same reaction condition previously reported, comparing the results achieved from the electrolysis of 0.01, 0.50 and 0.10 M glucose solution over a NiC500-1h sample.

The CVs reported in figure 4.17 show how the peaks related to the GOR change with the concentration of glucose. The onset of the process is quite similar in presence of glucose 0.01 and 0.50 M, while it occurs at a lower anodic potential of 60-70 mV in the presence of glucose 0.10 M. It should be noted that the discharge of OER is strongly influenced by glucose concentration in solution, indeed it can be observed as the shape of the curve and the current density developed suffer a dramatic change increasing the concentration of glucose. The shape of the curves could suggest that high glucose concentrations could partially suppress or limit the oxygen evolution reaction.

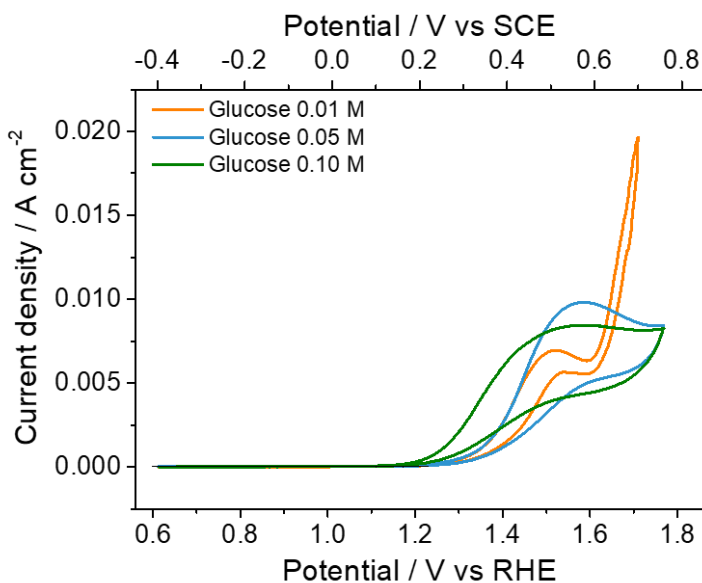


Figure 4.17. Cyclic voltammeteries recorded in Glucose 0.01, 0.05 and 0.10 M + NaOH 0.1M over NiC5001h foam. Range: -0.4 to 0.8 V vs SCE (0.61 to 1.81 V vs RHE). Scan rate: 5 mV/s.

The results obtained from glucose electrolysis at 0.01, 0.50 and 0.10 M (Table 4.4) evidenced that the conversion of glucose is not apparently affected by the change in glucose concentration, with the values quite stable around 50-55 %. Nevertheless, it must be considered that due to the long reaction time necessary to collect the charge required for the total conversion of a 0.10 M glucose solution, only ~360 C were actually collected instead of 482 C. Therefore, under conditions of total theoretical conversion, the actual final conversion would certainly be higher.

The selectivity does not follow a clear trend; with 0.05 M glucose the higher values are reached, while it decreases both at higher and lower concentrations. In particular, with glucose 0.01 M the selectivity is relatively close to that observed at 0.05 M, with a difference of less than 10%, while at 0.10 M a difference of up to 20% is reached. No enhancement can be observed concerning the GA selectivity, in addition the low selectivity recorded, 3 – 6 %, does not allow to clarify the presence of beneficial effect of an increase of glucose concentration.

Regarding the by-products formation, by lowering the glucose concentration, it appears that the formation of over-oxidised C1-C4 molecules increases (glycolic, oxalic and formic acids). This behaviour could be explained considering that from the CVs in glucose it seems that the presence of concentrated glucose limits the occurrence of OER. On the other hand, in presence of very concentrated solutions (100 mM), the lower presence of oxidizing species produced by OER favours the occurrence of C-C cleavage and rearrangement processes that lead to the formation of arabinose and 2KDG, respectively, limiting further oxidation.

Table 4.4. Glucose conversion (%) and distribution of the reaction products (in terms of selectivity %) resulting from the electrolyses of glucose 0.01 - 0.05 – 0.10 M in NaOH 0.1 M at 0.8 V vs SCE (1.81 V vs RHE) over a NiC500-1h electrocatalyst.

Compound	Glucose Concentration		
	0.01 M	0.05 M	0.10 M
Glucose conv.	51	54	51
Gluconic Ac.	52	56-66	44
Glucaric Ac.	3.7	2-5	6
Glucuronic Ac.	-	0-2	-
Glycolic Ac.	4.3	1-2	1.4
Tartronic Ac.	3.1	<1	<1
Tartaric Ac.	2.6	<1	<1
Oxalic Ac.	7.3	1-3	<1
Lactic Ac.	1	1-4	1.2
2-keto-D-gluconic Ac. (2KDG)	3.4	0-3	4.5
5-keto-D-gluconic Ac. 5KDG	-	-	-
Arabinose + Glyceric Ac.	6	3-7	13
Formic Ac.	9	4-9	6.5
Mesoxalic Ac.	-	<1	0
Total Sel.	~93	~96	~77

It should be remarked that by modifying the glucose concentration, keeping constant the amount of NaOH in solution, the glucose/NaOH ratio in solution is varied. Hence, in the next section, the variation of this ratio was investigated by modifying the concentration of NaOH in solution and keeping constant the concentration of glucose.

4.4.6. Effect of the Glucose/NaOH ratio

The CVs carried out using different ratio between glucose and NaOH are shown in figure 4.18. Increasing the amount of NaOH in solution the current density developed by OER discharge is linearly enhanced (Fig. 4.18a). The onset potential became less anodic by moving from lower to higher NaOH concentration, however slight differences of ca. 15 - 20 mV were recorded.

Tafel slope values in table 4.5 confirm that the OER activity is favoured at higher concentration of NaOH, i.e. increasing the pH, showing lower values from 0.05 M to 1.0 M concentration. This is in accordance with what is reported in the literature.¹⁴²

Instead, there is no apparent correlation between the area of the $\text{Ni}^{2+}/\text{Ni}^{3+}$ peaks and the current density developed by OER. This is visible both from the enlargement in figure 4.18a1 and from the area of the peaks reported in table 4.5.

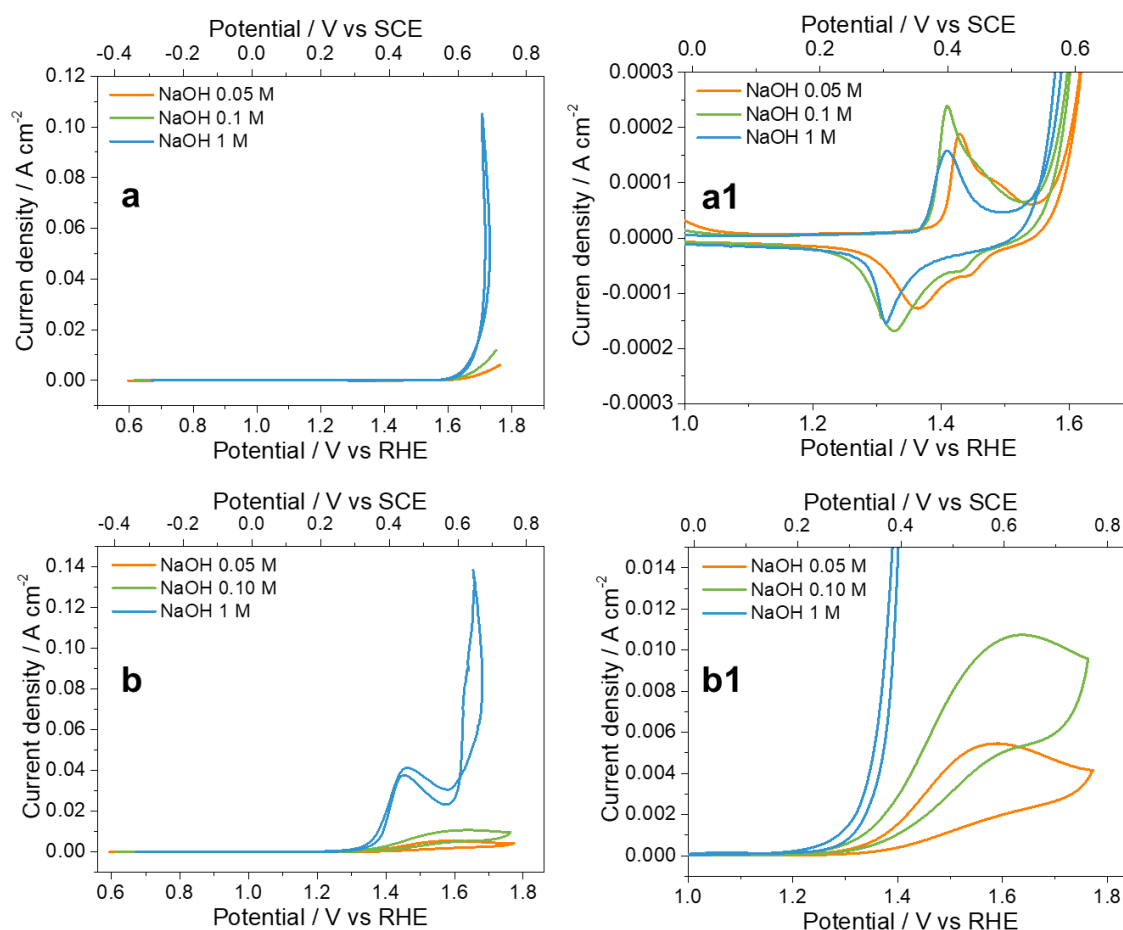


Figure 4.18. Cyclic voltammeteries recorded in NaOH (a, a1) 0.05 – 0.10 and 1.0 M and Glucose 50 mM+NaOH (b, b1) over NiC500-1h electrocatalyst.

However, it should be remarked that there are several species of NiOOH which have different catalytic activity,¹³³ whose presence can be suggested by the different forms observable in the peaks

in figures 4.18a1. Therefore, a greater area of the peaks is not always synonymous with the presence of a greater number of more active species.

The CVs recorded in glucose+NaOH solution (Fig 4.18b) show a similar trend to that observed in the CVs without glucose. Indeed, a higher current density developed and a less anodic onset, with a difference of ca. 45 - 55 mV, can be observed by increasing the concentration of NaOH in solution. Also Tafel slopes showed the same behaviour observed in the previous section, indeed the values increase in presence of glucose 50mM, regardless the amount of NaOH. Nevertheless, NaOH concentration affects the slope, with a large decrease by moving from 0.10 to 1.0 M of NaOH (130 vs 87 mV dec⁻¹, respectively) in presence of glucose, thus favouring the charge transfer kinetics. Instead, moving from 0.05 to 0.10 M the CVs have a similar shape, with the suppression of the OER discharge, and similar value of tafel slopes are recorded, indicating no substantial difference in charge transfer kinetics.

Table 4.5. Tafel slopes measured from CVs recorded in NaOH 0.05, 0.01 and 1.0 M with and without glucose 50 mM; integrated area of Ni²⁺/Ni³⁺ redox couple peaks at different NaOH concentrations.

NaOH	Slope NaOH / mV dec ⁻¹	Slope Glucose 0.05 M / mV dec ⁻¹	Ni ²⁺ → ³⁺ peaks area / mC cm ⁻²
0.05M	78	128	0.016
0.10 M	68	130	0.019
1.0 M	58	87	0.014

The results of the electrolysis of glucose 0.05 M, performed in solutions at different concentrations of NaOH, are shown in table 4.6. The contribution of NaOH is important to enhance the selectivity in GO, probably thanks to the improved activity of OER with the increase of NaOH concentration in solution. Nevertheless, the best GO selectivity value is observed in presence of NaOH 0.10 M. In lower NaOH containing solutions, the major by-products formed are probably arabinose and formic acid, due the C-C cleavage of C1-C2 bond.

Instead, it should be considered that the degradation of glucose in alkaline media is pH dependent, then a higher pH could enhance the occurrence of side reactions. Indeed, in these conditions, a great formation of over-oxidised products is observed, as lactic acid, glyceric acid and formic acid, which could be produced by either chemical or electrochemical processes.

Remarkably, the GA selectivity is apparently improved in NaOH concentrated solutions; probably, these stronger oxidant conditions favour the activation and further oxidation of C6 carbon of glucose.

However, the actual increase of GA selectivity is scarce, while a strong decrease in GO selectivity is reported.

Table 4.6. Glucose conversion (%) and distribution of the reaction products (in terms of selectivity %) resulting from the electrolyses of glucose 0.05 M in NaOH 0.05, 0.01 and 1.0 M at 0.8 V vs SCE over a NiC500-1h electrocatalyst.

Glucose Concentration			
Compound	NaOH 0.05 M	NaOH 0.10 M	NaOH 1.0 M
Glucose Conv.	42	54	32
Gluconic acid	26	56-66	39
Glucaric Ac.	-	2-5	8
Glucuronic Ac.	-	0-2	-
Glycolic Ac.	3.6	1-2	3
Tartronic Ac.	-	<1	2.1
Tartaric Ac.	-	<1	-
Oxalic Ac.	<1	1-3	7
Lactic Ac.	3.2	1-4	4.7
2-keto-D-gluconic Ac. (2KDG)	-	0-3	-
5-keto-D-gluconic Ac. 5KDG	-	-	-
Arabinose + Glyceric Ac.	26	3-7	15
Formic Ac.	17	4-9	9
Mesoxalic Ac.	-	<1	-
Total Sel.	76	~96	88

Finally, by comparing the results obtained with same glucose/NaOH ratio, 0.1 / 0.1 (table 4.4) and 0.05 / 0.05 (table 4.6), it can be observed how the production of GO and by-products are completely different. Indeed, reducing both glucose and NaOH concentrations in solution, a worsening of the

process efficiency was observed, with a strongly reduction of GO selectivity and thus obtaining a different pattern of by-products, with the presence of many over-oxidation compounds.

4.4.7. Influence of Fructose Electrolysis in Glucose Oxidation

As previously reported in section 4.3.4, the presence of fructose in the post-electrolyses solution was considered as unreacted glucose, instead of a by-product, due to the occurrence of isomerization process in alkaline media.¹¹⁶ Indeed, the HPLC analysis of glucose solution before the electrochemical tests shows an initial concentration of fructose equal to about 10% of the total, regardless of the glucose concentration used.

In order to verify the activity of fructose toward electrochemical oxidation a catalytic test was performed using a 0.01 M fructose solution in NaOH 0.10 M over a NiC500-1h electrocatalyst. The CVs performed were reported in figure 4.19 and compared with the results previously reported using a glucose solution at the same concentration.

We can observe that the catalyst used is also active for the oxidation of fructose, which shows an onset similar to that observed for glucose at ca. 0.21 V vs SCE (1.22 V vs RHE). The maximum of the peak is at more anodic potential of ca. 30 mV and a quite lower current density was developed; nevertheless, the peak of the OER is less intense, developing almost half of the current density than the test in the presence of glucose. Probably the presence of fructose limits the occurrence of OER.

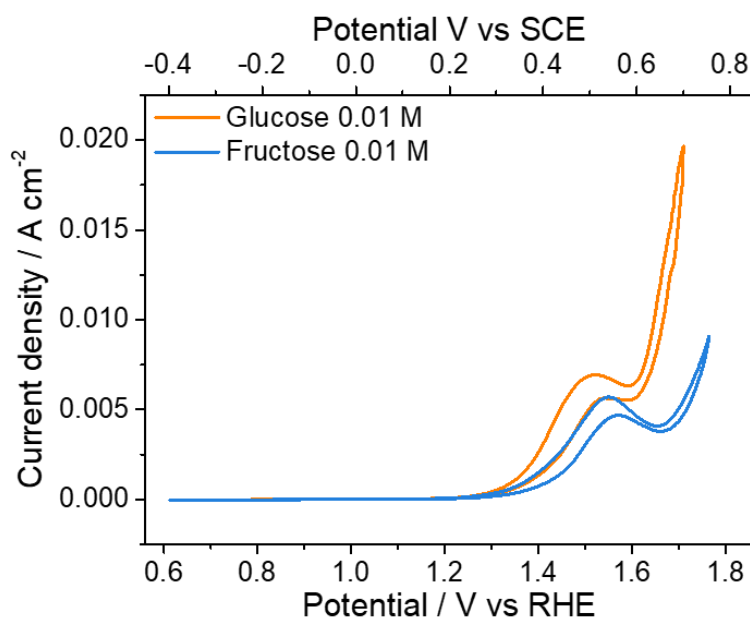


Figure 4.19. Cyclic voltammeteries recorded in Glucose and Fructose 0.01 M + NaOH 0.10 M over NiC5001h foam. Range: -0.4 to 0.8 V vs SCE (0.61 to 1.81 V vs RHE). Scan rate: 5 mV/s.

The data reported in table 4.7 show a similar conversion obtained for glucose and fructose, 51 vs 54 % respectively, but it should be noted that the conversion of fructose also includes the presence of

glucose in solution, which is ca 0.45 mM before and 1.2 mM after electrolysis. However, some differences are reported with respect to the formation of the products.

Table 4.7. Glucose and Fructose conversion (%) and distribution of the reaction products (in terms of selectivity %) resulting from the electrolyses of glucose and fructose 0.01 M solution in NaOH 0.10 M electrolyte at 0.8 V vs SCE (1.81 V vs RHE) over a NiC500-1h electrocatalyst.

Compound	Glucose 0.10 M	Fructose 0.10 M
Conversion	51	54
Gluconic Ac.	52	8
Glucaric Ac.	3.7	-
Glucuronic Ac.	-	3
Glycolic Ac.	4.3	17
Tartronic Ac.	3.1	-
Tartaric Ac.	2.6	1.6
Oxalic Ac.	7.3	2.3
Lactic Ac.	1	20
2-keto-D-gluconic Ac. (2KDG)	3.4	1.7
5-keto-D-gluconic Ac. 5KDG	-	-
Arabinose + Glyceric Ac.	6	23
Formic Ac.	9	10
Mesoxalic Ac.	-	1.8
Total Sel.	~93	~89

Surely, the gluconic acid produced during the reaction can be assigned to the oxidation of glucose formed by the isomerization of fructose, in fact this process is described as an equilibrium reaction that allows, for long times, to obtain the same ratio between glucose and fructose¹¹⁶ (in no case the production of mannose is observed, probably due to the too short times).

Observing the table 4.7, we can suppose that the formation of fructose is responsible for a part of 2KDG and the C1-C4 over-oxidation products observed during the glucose electrochemical oxidation, such as the presence of glyceric, glycolic, lactic and formic acids.

At this point we can complete the hypothetical reaction mechanism (Fig. 4.20), which includes the isomerization of glucose to fructose and its oxidation (blue arrows).

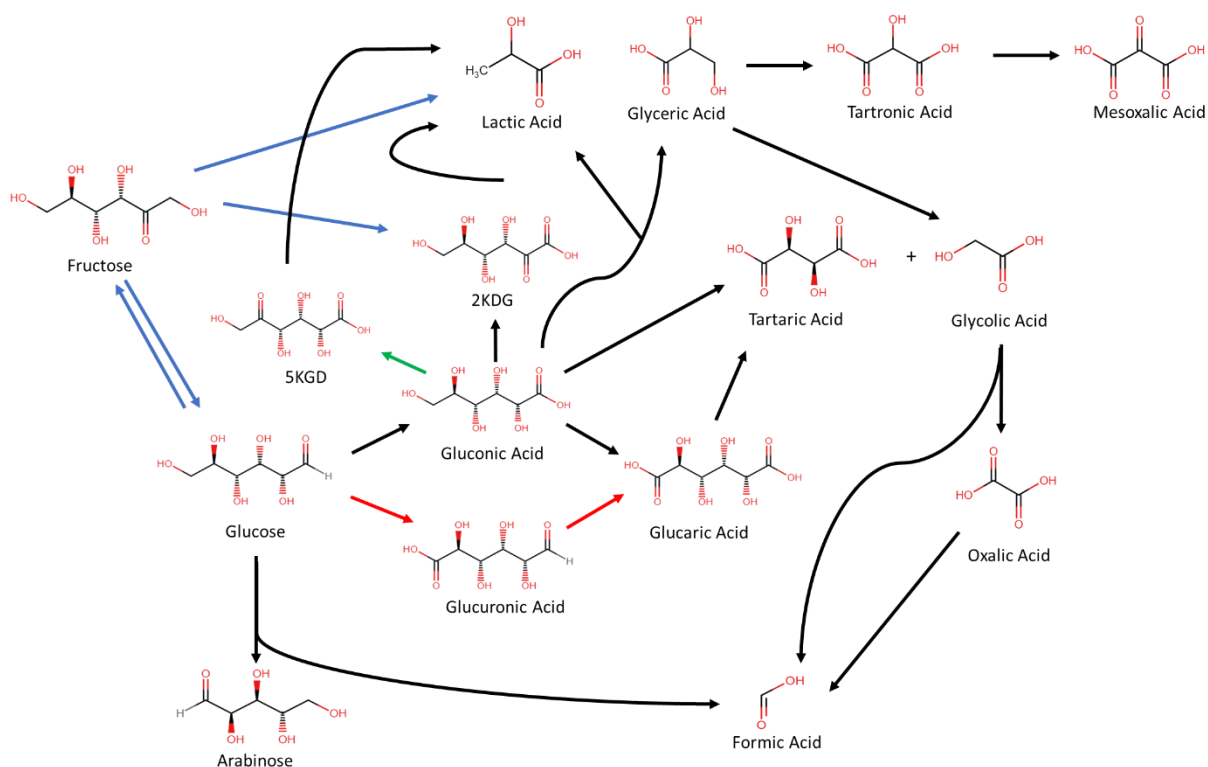


Figure 4.20. Reaction mechanism proposed for the electrochemical oxidation of glucose, adding the “fructose way”, blue arrows.

4.4.8. Effect of applied potential in glucose 0.50 M solutions with NaOH 0.1 M

It is well known that the potential used for glucose electrolysis influences the selectivity toward gluconic and glucaric acid and rules the occurrence of side reactions.^{33,121} In this work the glucose oxidation on NiC500-1h was carried out varying the potential from 0.6 to 0.9 V vs SCE (1.51 to 1.91 V vs RHE), the solution had a concentration of 0.05 M and the results are shown in table 4.8. No significant variation of glucose conversion was recorded, indicating that the potential has a slight effect on this parameter. Instead, important changes on the GO-GA selectivity and the by-products formation were detected.

The data in table 4.8 reveal that the GO selectivity increases with the potential, passing from the 25 % recorded at 0.6 V (1.61 V vs RHE) to the 67 % reached at 0.9 V vs SCE (1.91 V vs RHE).

Nevertheless, it must be remarked that in our case the loss in GO selectivity at less anodic potential is not compensated by an increase in GA selectivity, which remains very low, with the maximum (~5%) recorded between 0.7 and 0.8 V vs SCE.

Table 4.8. Glucose conversion (%) and distribution of the reaction products (in terms of selectivity %) resulting from the electrolyses of glucose 0.05 M in NaOH 0.1 M at potential from 0.6 V to 0.9 V vs SCE (1.61 V to 1.91 V vs RHE) over a NiC500-1h electrocatalyst.

Compound	Potential / V vs SCE			
	0.6 V	0.7 V	0.8 V	0.9 V
Glucose conv.	52	55	54	57
Gluconic Ac.	25	40.5	56-66	67
Glucaric Ac.	2.6	4.8	2-5	1.4
Glucuronic Ac.	-	-	0-2	13
Glycolic Ac.	2.4	3.9	1-2	2.2
Tartronic Ac.	<1	1.6	<1	1.2
Tartaric Ac.	<1	<1	<1	2.3
Oxalic Ac.	<1	<1	1-3	2.4
Lactic Ac.	4.4	-	1-4	-
2-keto-D-gluconic Ac. (2KDG)	2.5	4.4	0-3	-
5-keto-D-gluconic Ac. 5KDG	-	1.5	-	-
Arabinose + Glyceric Ac.	25.6	10	3-7	4.8
Formic Ac.	20	16	4-9	4.8
Mesoxalic Ac.	<1	<1	<1	<1
Total Sel.	~86	~86	~96	~100

Furthermore, applying a more cathodic potential, it is observed a rapid increase of glucuronic acid selectivity between 0.8 and 0.9 V vs SCE. This could suggest that at higher potential also the

activation of C6 carbon can occur (figure 4.20 – red arrows), however the catalyst fails to further selectively convert glucuronic acid to GA.

A variation in the reaction mechanism is also observed in the side reaction. It is interesting to note that the most important changes occurred in the formation of arabinose and formic acid, whose selectivities decrease at the same pace as the potential increases, while the other C4-C2 degradation products remain almost constant.

This could suggest that the mechanism involves the activation of glucose C1, which forms gluconic acid in the presence of oxidizing species. It is possible that at less anodic potentials, the formation of oxidant species produced from water (as O*, OH*, etc.) by OER are partially lost, so the reaction also proceeds towards C-C cleavage between C1 and C2.

A further minority route instead involves the formation of 2KDG, which in fact reaches the maximum at 0.7 V vs SCE and decreases until it disappears at higher potentials.

At the same time, with the increased contribution of OER, the C6 carbon is apparently also activated, with higher formation of glucaric acid and also 5KDG. However, as already observed the final oxidation step of gluconic and glucuronic acids oxidation to glucaric acid, remains the limiting step.

4.4.8.1. Effect of the Potential on the Selective Electro-oxidation of Gluconic Acid to Glucaric Acid

To verify the best conditions for the selective production of glucaric acid, the electrochemical oxidation of a gluconic acid over a NiC500-1h electrocatalyst was investigated. The reaction was conducted modifying the potential between 0.6 and 0.8 V vs SCE (1.61 – 1.81 V vs RHE), the solution has a concentration of 0.01 M of sodium gluconate in NaOH 0.10 M.

Comparing the CVs in glucose and gluconate (Fig. 4.21) the oxidation peaks of both reagents can be observed, between 0.3 and 0.7 V vs SCE (1.31 - 1.71 V vs RHE), without remarkably difference in the onset and the shape of the peaks. The main difference regards the OER discharge, which starts at less anodic potential, reaching a higher current density in presence of glucose. These results could suggest that the presence of gluconate in solution partially inhibits this process.

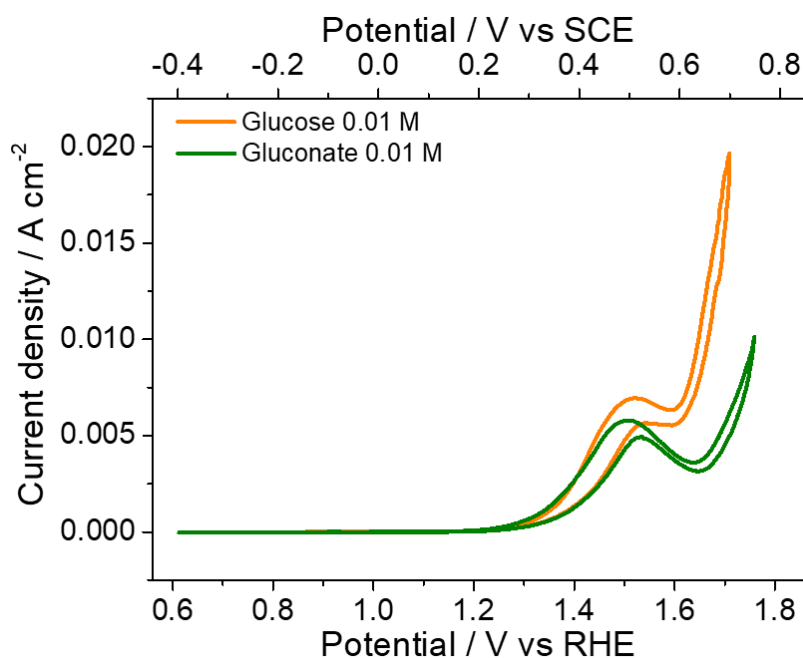


Figure 4.21. Cyclic voltammograms recorded in Glucose and Gluconate 0.01 M + NaOH 0.1M over NiC5001h foam. Range: -0.4 to 0.8 V vs SCE (0.61 to 1.81 V vs RHE). Scan rate: 5 mV/s.

The results of gluconate electrolysis (Table 4.9) showed that to achieve a more selective oxidation of glucose to gluconic acid a lower potential must be used (between 0.6 - 0.7 V vs SCE; 1.61 - 1.71 V vs RHE). It should be remembered that all the tests for the oxidation of glucose were conducted providing the charge necessary for the total and selective conversion into GO, therefore it is possible that a longer reaction time is required to obtain a better selectivity in GA.

The outcomes obtained from the electrochemical oxidation of gluconate are in line with those observed from glucose and indicate that both GO itself and probably the gluconic acid are subjected to further oxidation reactions, with the formation of low molecular weight C1- C4.

The mechanism seems to be in accordance with what previously reported in figure 4.20. Gluconate, in addition to give GA, is converted into 5KDG and 2KDG and then undergoes further oxidation processes to form discrete quantities of tartronic and glyceric acid (by C-C cleavage/retro-aldol reaction on C3 carbon of GO). The latter products evolve towards the formation of mesoxalic acid and glycolic acid, respectively, to obtain oxalic and large quantities of formic acid. However, the formation of low amount of arabinose, by decarboxylation of C1 carbon of gluconic acid, cannot be excluded.

Table 4.9. Gluconic acid conversion (%) and distribution of the reaction products (in terms of selectivity %) resulting from the electrolyses of gluconate 0.01 M in NaOH 0.1 M at potential from 0.6 V to 0.8 V vs SCE (1.61 V to 1.81 V vs RHE) over a NiC500-1h electrocatalyst.

Compound	Potential / V vs SCE		
	0.6 V	0.7 V	0.8 V
Gluconic Ac. Conv.	49	43	25
Glucaric Ac.	29	31	25
Glucuronic Ac.	-	-	-
Glycolic Ac.	5	9	6
Tartronic Ac.	8	9	7
Tartaric Ac.	-	-	-
Oxalic Ac.	7	10	12
Lactic Ac.	-	<1	<1
2-keto-D-gluconic Ac. (2KDG)	8	11	9
5-keto-D-gluconic Ac. 5KDG	4	9	6
Arabinose + Glyceric Ac.	3	6	6
Formic Ac.	22	15	10
Mesoxalic Ac.	4	5	6
Total Sel.	~91	~100	~88

Finally, it should be noted that increasing the potential a decrease in gluconate conversion is observed, probably due to the parallel occurrence of OER that lower the efficiency of the oxidation process. Moreover a change in selectivity of by-products can be observed, with a higher homogeneous production of C2-C3 and a decreases of formic acid. It is possible that the latter compound is further oxidised to CO₂ as the applied potential increases.

4.4.8.2. Effect of Gluconic Acid Concentration

In this section it has been investigated how the variation in the concentration of gluconic acid affects the electrochemical oxidation process. For this purpose, the electrochemical oxidation of a 5mM solution of gluconic acid (as sodium gluconate) in 0.1M NaOH was carried out at 0.7 V vs SCE.

It can be observed that by decreasing the concentration of gluconic acid the conversion drastically decreases, however the selectivity in GA remains high, with a slight increase recorded (Table 4.10).

Table 4.10. Gluconic acid conversion (%) and distribution of the reaction products (in terms of selectivity %) resulting from the electrolyses of gluconate 5 and 10mM in NaOH 0.1 M at 0.7 V vs SCE (1.71 V vs RHE) over a NiC500-1h electrocatalyst.

Compound	Gluconic Acid Concentration	
	5mM	10mM
Gluconic Ac. Conv.	20	43
Glucaric Ac.	34	31
Glucuronic Ac.	-	-
Glycolic Ac.	-	9
Tartronic Ac.	11	9
Tartaric Ac.	-	-
Oxalic Ac.	16	10
Lactic Ac.	14	<1
2-keto-D-gluconic Ac. (2KDG)	9	11
5-keto-D-gluconic Ac. 5KDG	-	9
Arabinose + Glyceric Ac.	-	6
Formic Ac.	-	15
Mesoxalic Ac.	20	5
Total Sel.	~100	~100

The production of by-products changes, with the preferential formation of 2KDG and C3-C4 molecules, such as tartaric, mesoxalic and lactic acid. While, there are practically no products with a very low molecular weight due the over-oxidation, such as glycolic and formic acid.

In this case, the low concentration and the consequent lower conversion occurred suggests a low efficiency of the gluconic acid oxidation and, especially, the further oxidation process in favour of OER, which avoids the formation of C2 and C1 species.

4.4.9. Stability Test for glucose electro-oxidation over NiC500-1h foam

Finally, the stability of the catalytic performances of the NiC500-1h electrocatalyst was investigated performing three consecutive electrolysis of glucose 0.50 M solution in NaOH 0.1 M (Table 4.11).

The results confirm the stability of the catalyst with the catalytic cycle, with a constant conversion of ca. 55%, with except a lower value in the first run, and also a quite constant GO selectivity between 62 and 66%. Conversely, a decrease of GA selectivity was observed, passing from 5.5 to 2.5 %.

The mechanism can be supposed rather constant over the catalytic cycles, indeed also the production of by-products is constant during the different run, with exception of formic acid and arabinose/glyceric acid. For these latter products the lower selectivity in the second run was recorded when the higher GO selectivity is observed.

It can be supposed that during the first and third electrolysis, a slightly higher amount of arabinose could be formed. However, glyceric acid is probably also present, suggested by the formation of different C2-C3 products derived from its oxidation, such as glycolic, tartronic and oxalic acids.

Hence, formic acid results from the decarboxylation of C1 of glucose or gluconic acid to give arabinose, or from the subsequent oxidation of the degradation C2-C4 products.

Table 4.11. Glucose conversion (%) and distribution of the reaction products (in terms of selectivity %) resulting from three consecutive electrolyses performed over a NiC500-1h electrocatalyst, using a glucose 0.05 M solution in NaOH 0.1 M at 0.8 V vs SCE (1.81 V vs RHE)

Compound	1st run	2nd run	3rd run
Glucose conv.	45	55	54
Gluconic Ac.	63	66	62
Glucaric Ac.	5.5	4.7	2.5
Glucuronic Ac.	-	-	-
Glycolic Ac.	2.2	2.7	3
Tartronic Ac.	1.5	1.1	1.2
Tartaric Ac.	<1	<1	<1
Oxalic Ac.	3	3	2.7
Lactic Ac.	3.7	2.2	2.3
2-keto-D-gluconic Ac. (2KDG)	-	-	-
5-keto-D-gluconic Ac. 5KDG	-	-	-
Arabinose + Glyceric Ac.	7	4	10
Formic Ac.	9	6	8
Mesoxalic Ac.	-	-	-
Total Sel.	~96	~90	~92

4.4.10. Electrochemical Characterization of used catalysts

After the electrolyses changes in the CVs in NaOH and glucose+NaOH occurred. It should be noted that all the catalysts used exhibit the same trend before and after the electrocatalytic tests, and also no differences were observed regardless the concentration of glucose or NaOH used and the potential

applied during the electrolysis, except $\text{Ni}(\text{OH})_2/\text{Ni}$ catalyst; thus, in figure 4.22 the CVs recorded on NiC500-1h, as illustrative purpose, and $\text{Ni}(\text{OH})_2/\text{Ni}$ electrocatalysts are reported.

A greater activity towards the OER is observed for the calcined foam (Fig. 4.22a), with the onset recorded at less anodic potential of ca 500 mV and an almost double current density developed, however similar tafel slopes are reported in table 4.12 between before and after the catalytic tests.

The increases of the catalytic activity may be due to changes occurred in the oxide species present on the surface, which can lead to the formation of more active Ni^{3+} species in the electrochemical oxidation process. This can be suggested by observing a slight variation in the shape of the peaks in the inset of figures 4.22a.

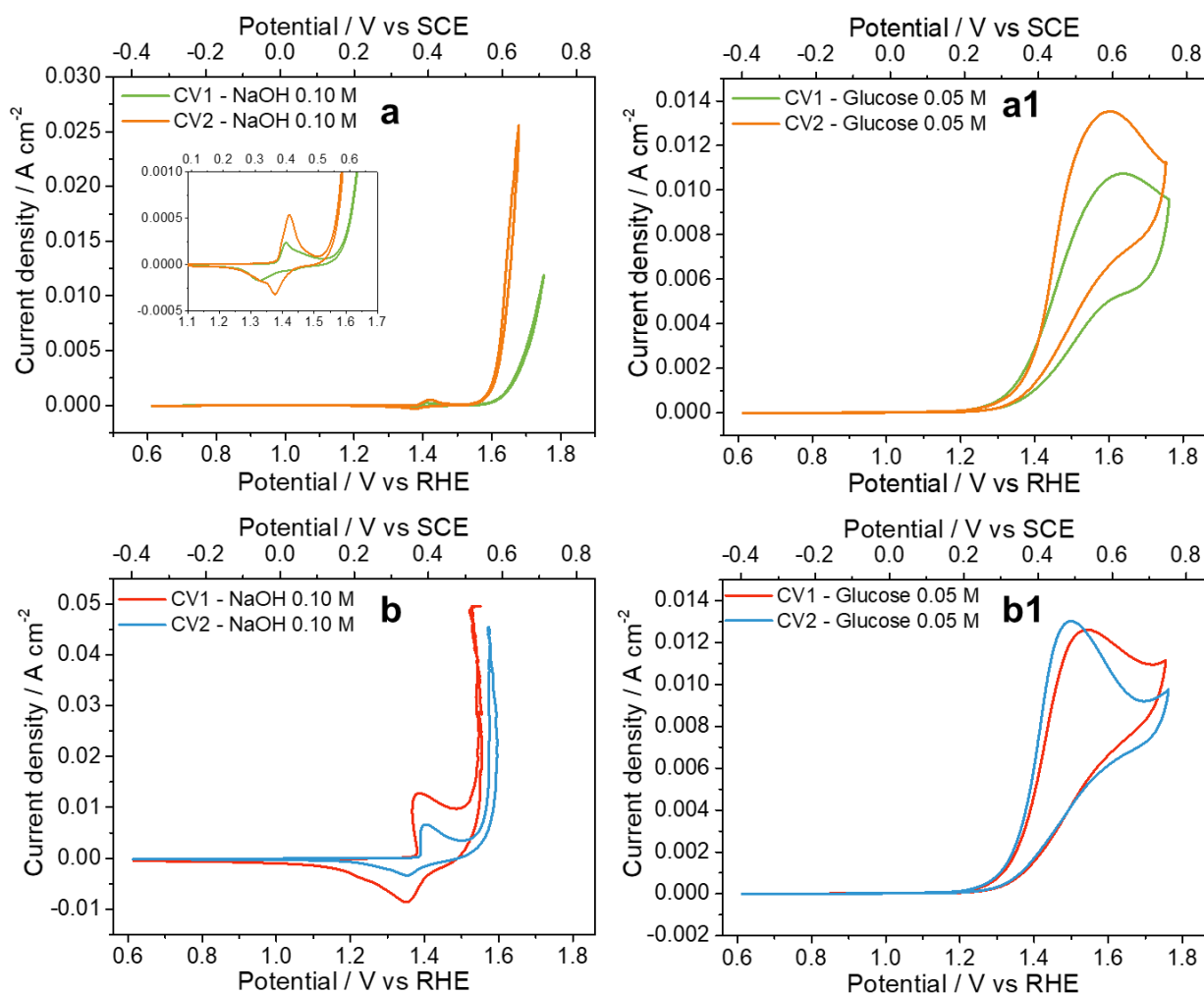


Figure 4.22. Cyclic voltammeteries recorded in NaOH 0.1M and glucose 0.05 M before and after catalytic tests over NiC500-1h (a, a1) and $\text{Ni}(\text{OH})_2/\text{Ni}$ foams (b, b1). Range: -0.4 to 0.8 V vs SCE (0.61 to 1.81 V vs RHE). Scan rate: 5 mV/s.

Conversely, the foam with $\text{Ni}(\text{OH})_2$ electrodeposited shows a deactivation toward OER. Indeed, the onset was recorded at more anodic potential, and an increase in tafel slope is reported (Fig. 4.22b, Table 4.12) due to the worsen kinetics charge transfer. In this case, considerable differences can be

observed between the peaks due to the oxidation of Ni^{2+} to Ni^{3+} , observable between 0.2 and 0.6 V vs SCE (1.21 and 1.61 V vs RHE).

Table 4.12. Tafel slopes measured from CVs recorded in NaOH 0.1 M and NaOH+Glucose 0.05 M over fresh and used NiC500-1h and $\text{Ni}(\text{OH})_2/\text{Ni}$ electrocatalyst; Area of the $\text{Ni}^{2+}/\text{Ni}^{3+}$ peaks observed in the CV in NaOH.

Sample	Slope NaOH 0.1 M / mV dec ⁻¹	Slope Glucose 0.05 M / mV dec ⁻¹	$\text{Ni}^{2+ \rightarrow 3+}$ peaks area / mC cm ⁻²
NiC500-1h fresh	68	130	0.019
NiC500-1h used	65	158	0.034
$\text{Ni}(\text{OH})_2/\text{Ni}$ fresh	68	118	1.397
$\text{Ni}(\text{OH})_2/\text{Ni}$ used	75	126	0.599

Adding glucose 0.05 M in solution no particular differences are noted in the onsets of the reaction, but some changes can be observed in the shape of the curves. Higher tafel slopes of both NiC500-1h and $\text{Ni}(\text{OH})_2/\text{Ni}$ samples are reported, nevertheless the former catalyst develops a slightly higher current density (Fig. 4.22a1), while the latter shows the maximum of the peak recorded at less anodic potential (Fig.4.22b1).

In both samples the behaviours observed toward the OER and glucose oxidation could indicate that changes occurred in the morphology and the species present on their surfaces modified the catalytic activity. These lead to an increase in the glucose conversion, observed in the stability tests for the NiC500-1h catalyst, while keeping the selectivity in GO almost unchanged. Instead, a worsening of oxidation following GA is observed, with an increase in the quantity of oxidation by-products.

4.4.11. Characterization of used Ni-based Electrocatalysts

No relevant differences were observed after the catalytic tests for the samples studied in this work, with the exception for the foam electrodeposited with nickel hydroxide. Hence, only the images relating to the NiC500-1h and $\text{Ni}(\text{OH})_2/\text{Ni}$ electrocatalysts are shown in figure 4.23.

The FE-SEM images of the calcined foam (Fig. 4.23a, a1) do not show significant variations in the morphology of the catalyst. As already observed before the reaction, the foam is covered by an inhomogeneous oxide layer with irregularly shaped particles. However, the XRD patterns in figure 4.24a reveal that the intensity of the peaks related to NiO phase decreases after the electrocatalytic tests for all the calcined foams, which is probably due to a lower crystallinity of NiO.

Also micro-Raman spectra of calcined foams are modified after reaction. The spectra in Fig 4.24c exhibit the main bands of NiO at 540 (1P-LO), 1092 (2P-LO) and 1500 cm^{-1} (2M), with the increase of the intensity of the 1P-LO mode, attributable to the presence of surface defects.¹³⁶

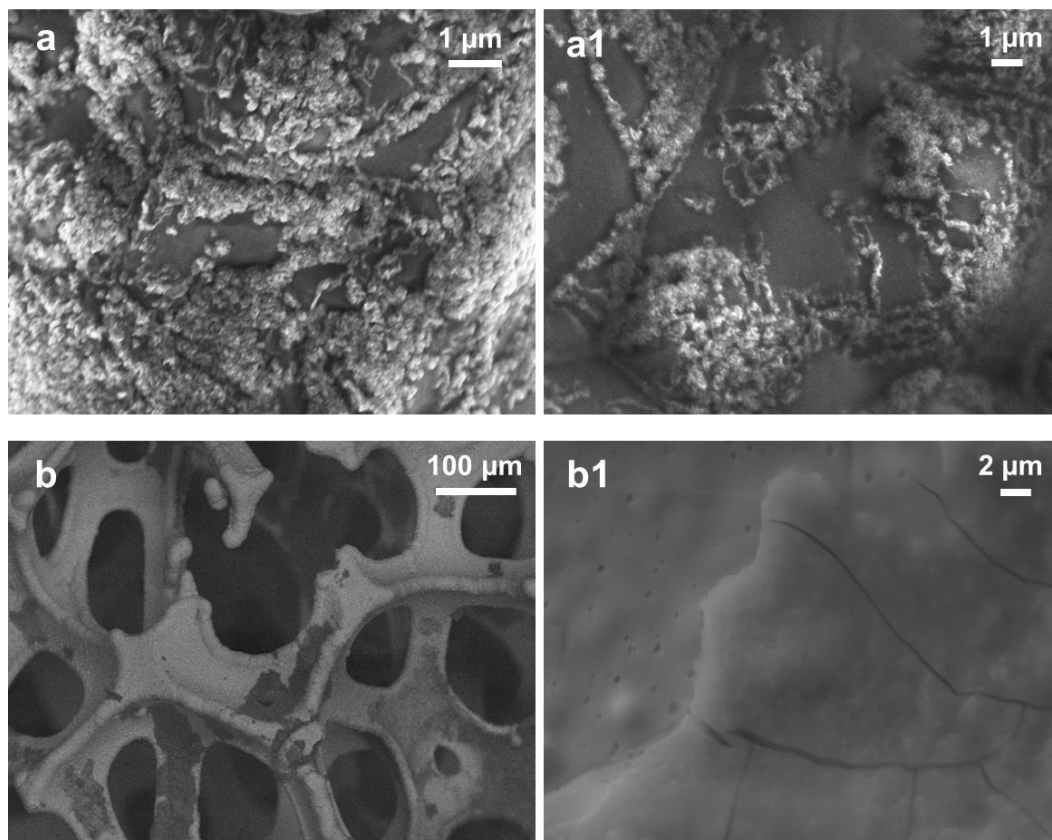


Figure 4.23. FE-SEM images of NiC500-1h (a, a1) catalyst and SEM images of Ni(OH)₂/Ni (b, b1) catalyst after electrolysis of glucose.

The SEM images in figure 4.23b and b1 show the detachment of the Ni-hydroxide layer from the foam surface, which can explain the lower activity exhibited by the electrode after the electrochemical test and the dramatic decreases of the peaks area of the Ni^{2+/3+} redox couple.

The Raman spectra in figure 4.24d show that after reaction the β -Ni(OH)₂ species is the crystallographic form most present in the residual hydroxide layer, identified by the characteristic bands at 314 (E_g lattice mode), 453 (A_{1g} lattice mode) and 3580 (A_{1g} O–H stretch) cm^{-1} .^{138,139} This is due to the aging process that the hydroxide undergoes when subjected to the application of a potential, which leads to the dehydration of the less crystalline α -phase and the enrichment in the more crystalline β -phase.¹⁴³ However, the presence of the residual signals at 1047 and 3646 cm^{-1} reveals that even the α -Ni(OH)₂ form is still present although in smaller quantities than previously observed in figure 4.11.

Finally, no changes in Nibare and Ni/Ni foams can be observed from XRD and Raman spectra.

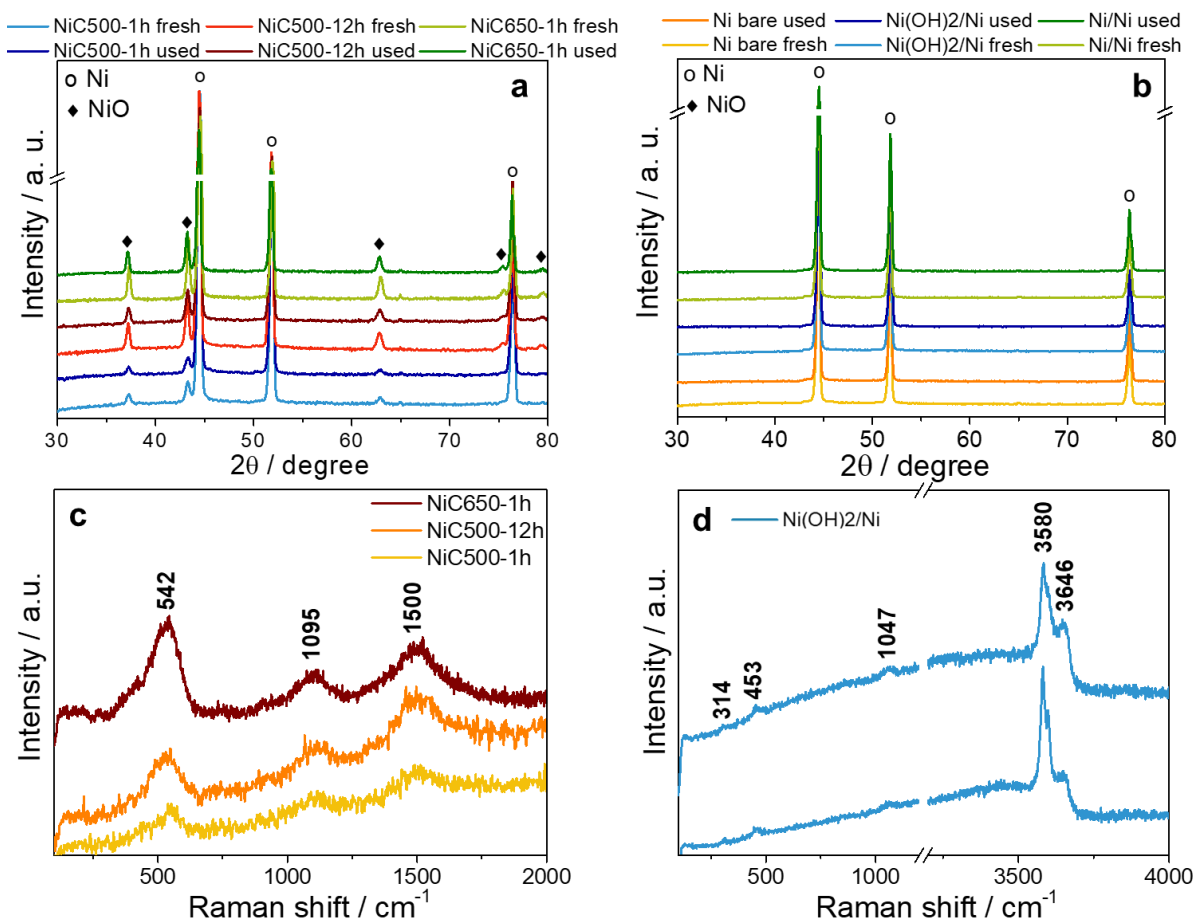


Figure 4.24. XRD patterns (a, b) and Raman spectra (c, d) of calcined and electrodeposited foams.

4.5. Conclusions

The glucose electrooxidation in alkaline media over Ni foam-based catalysts here investigated follows a complex reaction pathway that leads to a decrease in the selective conversion of glucose to gluconic and glucaric acid. These pathways depend on both the type and amount of Ni species and the reaction conditions.

A simple calcination of the bare foams at 500 °C for 1 h generates a well adhered NiO layer that presents the best balance between glucose conversion and selectivity. A longer or higher temperature thermal treatment, at 500°C-12 h or 650°C-1h, increases the thickness of the layer, producing a lower selectivity toward gluconic acid. While a large increase in the amount of Ni species in the coating both by deposition of Ni metallic particles or Ni(OH)₂ layers worsen the performances of the catalyst, showing lower conversion and selectivity of glucose. Moreover, the hydroxide layer is unstable, with large detachments observed after the electrochemical test.

The catalyst calcined at 500 °C for 1 h is able to activate the C1 carbon of glucose, however, the non-selective conversion of glucose to 2KDG, from C2 oxidation, or arabinose and formic acid, from C-C cleavage, decreases the selectivity. While the formation of C2-C4 by-products of over-oxidation

and retro-aldol processes only has a low impact. These latter could be related to the alkalinity of the electrolyte and to the electrochemical conversion of fructose, in situ formed by glucose isomerization. The conversion and the selectivity increase with the time, and after 100 C passed the maximum formation of by-product was observed.

High glucose/NaOH ratio limit the occurrence of OER, and consequently the selectivity in GO decreases; on the contrary, at low glucose/NaOH ratios the occurrence of OER favour the formation of GO and over-oxidised by-products. The best performances were obtained for a glucose/NaOH ratio at ca. 0.5 - 0.1.

By modifying the applied potential an effect similar to the variation of the glucose/NaOH ratio can be obtained; indeed, the GO and GA selectivities increase with increasing the potential, with a modest increase in conversion observed. It should be noted that the presence of glucuronic acid at higher potential, could suggest the occurrence of an alternative pathway for the formation of GA, however the final oxidation of gluconic and glucuronic acid to glucaric acid is still the limiting step. To enhance the GA selectivity, less anodic potentials must be used (0.6 – 0.7V vs SCE), as observed by the tests carried out on gluconic acid. However, the maximum selectivity reached is around 30-35%.

After several catalytic cycles, the catalyst maintains good performances during the electrolysis. However, the post reaction characterization shows changes occurred to the catalyst that need further investigation to be clarified.

5. Conclusion Remarks and Outlook

The electrochemical conversion is a promising way for the sustainable exploitation of biomass-derived platform molecules for the production of high-added value products. For this purpose, the use of open-cell foams allows to enhance the activity compared to the 2D electrodes.

Galvanic displacement and electrodeposition are facile and cheap methods useful to synthesize an Ag nanostructured electrocatalyst composed by a homogenous thin layer of nanoparticles or hierarchical structure, with different dimensions and shapes, obtained by varying the deposition conditions on Cu open-cell foam. This type of structure allows a large increase in the surface area, mass and charge transfer in the Ag/Cu catalysts, compared to Cu and Ag bare foam, through the synergistic effect given by the formation of bimetallic AgCu particles.

The Ag/Cu bimetallic 3D electro-catalysts synthesized in this work, have proved efficient and selective in the catalytic hydrogenation of HMF to BHMF, showing a higher productivity in BHMF compared to the 2D electrodes reported in the literature. However, the increase in electroactive surface area and the beneficial effect of nanostructuration were not enough to selectively convert concentrated HMF solutions, due the occurrence of side reactions and in particular the production of hydrofuronin dimer.

The catalyst was quite stable during several catalytic cycles, some changes on its surface occurred, but the performance was not significantly affected. Thus, Ag/Cu electrodes can be considered promising catalysts, but it is mandatory to be able to implement the efficient conversion of more concentrated HMF solutions, then that they could be used in large-scale applications.

The electrochemical deposition of Ni⁰ particles and Ni(OH)₂ has proved to be an excellent method to enhance the formation of Ni³⁺ species on surface, considered the active species in electrochemical oxidation reactions.

In this study we have seen how the formation of NiOOH favours the occurrence of oxygen evolution reaction and leads to the degradation of glucose in solution, with the formation of low molecular weight over-oxidation products.

On the other hand, by means of thermal treatment, the formation of the Ni-oxide has shown better results for the electrochemical oxidation of glucose. Nevertheless, the selective electrochemical oxidation of glucose to gluconic and glucaric acids is a very challenging process, and the selection of correct reaction parameters is very important to maximize GA selectivity and limits side reaction.

The study of the reaction parameters showed that the glucose/NaOH ratio and the applied potential play an important role in the process, with similar effects on the mechanism.

Indeed, the presence of low potentials or high glucose/NaOH ratio limit the OER and leads to the formation of partial oxidation products, through non-selective activation of C1, with the formation of arabinose and 2KDG. Lowering the glucose/NaOH ratio, or raising the potential, the contribution of OER and gluconic selectivity was increased. Also, the presence of low molecular weight products is observed, obtained by breaking intermediate C-C bonds or retro-aldol processes. However, studies conducted on gluconate have shown that lower potentials are needed to increase the selectivity in glucaric acid, while the greater selectivities in gluconic acid were achieved with glucose/NaOH ratio between 0.5 and 0.1.

These outcomes can be used as starting points to find the best reaction conditions. At the same time, the activity and the stability shown by the calcined catalyst during the catalytic cycle, indicate that it is a good candidate to be used as a support, for the deposition of an active phase and the development of an efficient and selective catalyst.

Bibliography

1. Cherubini, F., Jungmeier, G., Germany, T. W., Ireland, P. W. *IEA Bioenergy Task 42 – Countries Report*. (2009).
2. Sheldon, R. A. Green and sustainable manufacture of chemicals from biomass: State of the art. *Green Chem.* **16**, 950–963 (2014).
3. Ekman, A., Börjesson, P. Environmental assessment of propionic acid produced in an agricultural biomass-based biorefinery system. *J. Clean. Prod.* **19**, 1257–1265 (2011).
4. de Jong, E., Jungmeier, G. Biorefinery Concepts in Comparison to Petrochemical Refineries. in *Industrial Biorefineries and White Biotechnology* 3–33 (Elsevier B.V., 2015).
5. Cherubini, F. The biorefinery concept: Using biomass instead of oil for producing energy and chemicals. *Energy Convers. Manag.* **51**, 1412–1421 (2010).
6. From refinery to bio-refinery. <https://www.eni.com/en-IT/operations/biorefineries.html>.
7. Ioannidou, S. M., Paterakia, C., Ladakisa, D., Papapostolou, H., Tsakonaa, M., Vlysidisa, A., Kookosb, I. K., Koutinas. A. Sustainable production of bio-based chemicals and polymers via integrated biomass refining and bioprocessing in a circular bioeconomy context. *Bioresour. Technol.* **307**, 123093 (2020).
8. Takkellapati, S., Li, T. Gonzalez, M. A. An overview of biorefinery-derived platform chemicals from a cellulose and hemicellulose biorefinery. *Clean Technol. Environ. Policy* **20**, 1615–1630 (2018).
9. Palmeros Parada, M., Osseweijer, P., Posada Duque, J. A. Sustainable biorefineries, an analysis of practices for incorporating sustainability in biorefinery design. *Ind. Crops Prod.* **106**, 105–123 (2017).
10. Callegari, A., Bolognesi, S., Ceconet, D., Capodaglio, A. G. Production technologies, current role, and future prospects of biofuels feedstocks: A state-of-the-art review. *Crit. Rev. Environ. Sci. Technol.* **50**, 384–436 (2020).
11. Paone, E., Tabanelli, T., Mauriello, F. The rise of lignin biorefinery. *Curr. Opin. Green Sustain. Chem.* **24**, 1–6 (2020).
12. Ubando, A. T., Felix, C. B., Chen, W. H. Biorefineries in circular bioeconomy: A comprehensive review. *Bioresour. Technol.* **299**, (2020).
13. Kamm, B., Kamm, M. Principles of biorefineries. *Appl. Microbiol. Biotechnol.* **64**, 137–145 (2004).
14. Mussatto, S. I., Dragone, G. M. *Biomass Pretreatment, Biorefineries, and Potential Products for a Bioeconomy Development. Biomass Fractionation Technologies for a Lignocellulosic*

Feedstock Based Biorefinery (Elsevier Inc., 2016).

15. Palkovits, S., Palkovits, R. The Role of Electrochemistry in Future Dynamic Bio-Refineries: A Focus on (Non-)Kolbe Electrolysis. *Chemie-Ingenieur-Technik* **91**, 699–706 (2019).
16. Harnisch, F., Urban, C. Electrobiorefineries: Unlocking the Synergy of Electrochemical and Microbial Conversions. *Angew. Chemie - Int. Ed.* **57**, 10016–10023 (2018).
17. Hegner, R., Neubert, K., Kroner, C., Holtmann, D., Harnisch, F. Coupled Electrochemical and Microbial Catalysis for the Production of Polymer Bricks. *ChemSusChem* **13**, 5295–5300 (2020).
18. IRENA. Power-to-X solutions. *Innovation landscape for a renewable-powered future: Solutions to integrate variable renewables* 1–8 https://irena.org/-/media/Files/IRENA/Agency/Topics/Innovation-and-Technology/IRENA_Landscape_Solution_11.pdf?la=en&hash=2BE79AC597ED18A96E5415942E0B93232F82FD85 (2019).
19. Seh, Z. W., Kibsgaard J., Dickens, C. F., Chorkendorff, I., Nørskov, J. K., Jaramillo, T. F. Combining theory and experiment in electrocatalysis: Insights into materials design. *Science*. **355**, 146 (2017).
20. Botte, G. G. Electrochemical Manufacturing in the Chemical Industry. *Electrochem. Soc. Interface* **23**, 47 (2014).
21. Kwon, Y., Schouten, K. J. P., Van Der Waal, J. C., De Jong, E., Koper, M. T. M. Electrocatalytic Conversion of Furanic Compounds. *ACS Catal.* **6**, 6704–6717 (2016).
22. Li, Y., Sun, Y., Qin, Y., Zhang, W., Wang, L., Luo, M., Yang, H., Guo, S. Recent Advances on Water-Splitting Electrocatalysis Mediated by Noble-Metal-Based Nanostructured Materials. *Adv. Energy Mater.* **10**, 1–20 (2020).
23. Dubouis, N., Grimaud, A. The hydrogen evolution reaction: From material to interfacial descriptors. *Chem. Sci.* **10**, 9165–9181 (2019).
24. Ge, Z., Fu, B., Zhao, J., Li, X., Ma, B., Chen, Y. A review of the electrocatalysts on hydrogen evolution reaction with an emphasis on Fe, Co and Ni-based phosphides. *J. Mater. Sci.* **55**, 14081–14104 (2020).
25. Zhu, W., Zhang, R., Qu, F., Asiri, A. M., Sun, X. Design and Application of Foams for Electrocatalysis. *ChemCatChem* **9**, 1721–1743 (2017).
26. Li, X., Hao, X., Abudula, A., Guan, G. Nanostructured catalysts for electrochemical water splitting: Current state and prospects. *J. Mater. Chem. A* **4**, 11973–12000 (2016).
27. Van Drunen, J., Pilapil, B. K., Makonnen, Y., Beauchemin, D., Gates, B. D., Jerkiewicz, G. Electrochemically active nickel foams as support materials for nanoscopic platinum

- electrocatalysts. *ACS Appl. Mater. Interfaces* **6**, 12046–12061 (2014).
28. Suen, N. T., Hung, S. F., Quan, Q., Zhang, N., Xu, Y. J., Chen, H. M. Electrocatalysis for the oxygen evolution reaction: Recent development and future perspectives. *Chem. Soc. Rev.* **46**, 337–365 (2017).
 29. Möhle, S., Zirbes, M., Rodrigo, E., Gieshoff, T., Wiebe, A., Waldvogel, S. R. Modern Electrochemical Aspects for the Synthesis of Value-Added Organic Products. *Angew. Chemie - Int. Ed.* **57**, 6018–6041 (2018).
 30. Orella, M. J., Román-Leshkov, Y., Brushett, F. R. Emerging opportunities for electrochemical processing to enable sustainable chemical manufacturing. *Curr. Opin. Chem. Eng.* **20**, 159–167 (2018).
 31. Carneiro, J., Nikolla, E. Electrochemical conversion of biomass-based oxygenated compounds. *Annu. Rev. Chem. Biomol. Eng.* **10**, 85–104 (2019).
 32. Du, L., Shao, Y., Sun, J., Yin, G., Du, C., Wang, Y. Electrocatalytic valorisation of biomass derived chemicals. *Catal. Sci. Technol.* **8**, 3216–3232 (2018).
 33. Moggia, G., Kenis, T., Daems, N., Breugelmans, T. Electrochemical Oxidation of d-Glucose in Alkaline Medium: Impact of Oxidation Potential and Chemical Side Reactions on the Selectivity to d-Gluconic and d-Glucaric Acid. *ChemElectroChem* **7**, 86–95 (2020).
 34. Rafaïdeen, T., Baranton, S., Coutanceau, C. Highly efficient and selective electrooxidation of glucose and xylose in alkaline medium at carbon supported alloyed PdAu nanocatalysts. *Appl. Catal. B Environ.* **243**, 641–656 (2019).
 35. Liu, W. J., Xu, Z., Zhao, D., Pan, X. Q., Li, H. C., Hu, X., Fan, Z. Y., Wang, W. K., Zhao, G. H., Jin, S., Huber, G. W. Yu, H. Q. Efficient electrochemical production of glucaric acid and H₂ via glucose electrolysis. *Nat. Commun.* **11**, 1–11 (2020).
 36. Bin, D., Wang, H., Li, J., Wang, H., Yin, Z., Kang, J., He, B., Li, Z. Controllable oxidation of glucose to gluconic acid and glucaric acid using an electrocatalytic reactor. *Electrochim. Acta* **130**, 170–178 (2014).
 37. Dos Santos, T. R., Nilges, P., Sauter, W., Harnisch, F., Schröder, U. Electrochemistry for the generation of renewable chemicals: Electrochemical conversion of levulinic acid. *RSC Adv.* **5**, 26634–26643 (2015).
 38. Stiefel, S., Schmitz, A., Peters, J., Di Marino, D., Wessling, M. An integrated electrochemical process to convert lignin to value-added products under mild conditions. *Green Chem.* **18**, 4999–5007 (2016).
 39. Schmitt, D., Regenbrecht, C., Hartmer, M., Stecker, F., Waldvogel, S. R. Highly selective generation of vanillin by anodic degradation of lignin: A combined approach of

- electrochemistry and product isolation by adsorption. *Beilstein J. Org. Chem.* **11**, 473–480 (2015).
40. Chen, S., Wojcieszak, R., Dumeignil, F., Marceau, E., Royer, S. How Catalysts and Experimental Conditions Determine the Selective Hydroconversion of Furfural and 5-Hydroxymethylfurfural. *Chem. Rev.* **118**, 11023–11117 (2018).
 41. Zhao, H., Zhu, Y. P., Yuan, Z. Y. Three-Dimensional Electrocatalysts for Sustainable Water Splitting Reactions. *Eur. J. Inorg. Chem.* **2016**, 1916–1923 (2016).
 42. Fang, Y., Yu, X. Y., Lou, X. W. (David). Nanostructured Electrode Materials for Advanced Sodium-Ion Batteries. *Matter* **1**, 90–114 (2019).
 43. Qian, X., Hang, T., Shanmugam, S., Li, M. Decoration of Micro-/Nanoscale Noble Metal Particles on 3D Porous Nickel Using Electrodeposition Technique as Electrocatalyst for Hydrogen Evolution Reaction in Alkaline Electrolyte. *ACS Appl. Mater. Interfaces* **7**, 15716–15725 (2015).
 44. Alia, S. M., Yan, Y. S., Pivovar, B. S. Galvanic displacement as a route to highly active and durable extended surface electrocatalysts. *Catal. Sci. Technol.* **4**, 3589–3600 (2014).
 45. Fu, L., Tamanna, T., Hu, W. J., Yu, A. Chemical preparation and applications of silver dendrites. *Chem. Pap.* **68**, 1283–1297 (2014).
 46. Chen, A., Holt-Hindle, P. Platinum-based nanostructured materials: Synthesis, properties, and applications. *Chem. Rev.* **110**, 3767–3804 (2010).
 47. Ustarroz, J., Hammons, J. A., Altantzis, T., Hubin, A., Bals, S., Terryn, H. A generalized electrochemical aggregative growth mechanism. *J. Am. Chem. Soc.* **135**, 11550–11561 (2013).
 48. Ho, P. H., Ospitali, F., Sanghez de Luna, G., Fornasari, G., Vaccari, A., Benito, P. Electrodeposition of Rh/Mg/Al hydroxides with different Mg-contents on metallic foams as catalyst precursors. *Appl. Clay Sci.* **191**, 105599 (2020).
 49. Ho, P. H., Ambrosetti, M., Groppi, G., Tronconi, E., Palkovits, R., Fornasari, G., Vaccari, A., Benito, P. Structured Catalysts-Based on Open-Cell Metallic Foams for Energy and Environmental Applications. in *Studies in Surface Science and Catalysis* vol. 178 303–327 (Elsevier B.V., 2019).
 50. Dinamani, M., Kamath, P. V. Electrosynthesis of Mg(OH)₂ coatings on stainless steel substrates. *J. Appl. Electrochem.* **34**, 899–902 (2004).
 51. Monti, M., Benito, P., Basile, F., Fornasari, G., Gazzano, M., Scavetta, E., Tonelli, D., Vaccari, A. Electrosynthesis of Ni/Al and Mg/Al Layered Double Hydroxides on Pt and FeCrAlloy supports: Study and control of the pH near the electrode surface. *Electrochim. Acta* **108**, 596–604 (2013).

52. Ho, P. H., Ambrosetti, M., Groppi, G., Tronconi, E., Fornasari, G., Vaccari, A., Benito, P. Electrodeposition of CeO₂ and Pd-CeO₂ on small pore size metallic foams: Selection of deposition parameters. *Catal. Today* **334**, 37–47 (2019).
53. Therese, G. H. A., Kamath, P. V. Electrochemical synthesis of metal oxides and hydroxides. *Chem. Mater.* **12**, 1195–1204 (2000).
54. Van Putten, R. J., Van Der Waal, J. C., De Jong, E., Rasrendra, C. B., Heeres, H. J., De Vries, J. G. Hydroxymethylfurfural, a versatile platform chemical made from renewable resources. *Chem. Rev.* **113**, 1499–1597 (2013).
55. Chadderdon, X. H., Chadderdon, D. J., Pfennig, T., Shanks, B. H., Li, W. Paired electrocatalytic hydrogenation and oxidation of 5-(hydroxymethyl)furfural for efficient production of biomass-derived monomers. *Green Chem.* **21**, 6210–6219 (2019).
56. Holzhäuser, F. J., Janke, T., Öztas, F., Broicher, C., Palkovits, R. Electrocatalytic Oxidation of 5-Hydroxymethylfurfural into the Monomer 2,5-Furandicarboxylic Acid using Mesostructured Nickel Oxide. *Adv. Sustain. Syst.* **4**, 2–6 (2020).
57. Huang, X., Zhang, L., Li, C., Tan, L., Wei, Z. High Selective Electrochemical Hydrogenation of Cinnamaldehyde to Cinnamyl Alcohol on RuO₂-SnO₂-TiO₂/Ti Electrode. *ACS Catal.* **9**, 11307–11316 (2019).
58. Chadderdon, X. H., Chadderdon, D. J., Matthiesen, J. E., Qiu, Y., Carraher, J. M., Tessonnier, J. P., Li, W. Mechanisms of Furfural Reduction on Metal Electrodes: Distinguishing Pathways for Selective Hydrogenation of Bioderived Oxygenates. *J. Am. Chem. Soc.* **139**, 14120–14128 (2017).
59. Bondue, C. J., Koper, M. T. M. Electrochemical Reduction of the Carbonyl Functional Group: The Importance of Adsorption Geometry, Molecular Structure, and Electrode Surface Structure. *J. Am. Chem. Soc.* **141**, 12071–12078 (2019).
60. Sanyal, U., Lopez-Ruiz, J., Padmaperuma, A. B., Holladay, J., Gutiérrez, O. Y. Electrocatalytic Hydrogenation of Oxygenated Compounds in Aqueous Phase. *Org. Process Res. Dev.* **22**, 1590–1598 (2018).
61. Cantu, D. C., Padmaperuma, A. B., Nguyen, M. T., Akhade, S. A., Yoon, Y., Wang, Y. G., Lee, M. S., Glezakou, V. A., Rousseau, R., Lilga, M. A. A Combined Experimental and Theoretical Study on the Activity and Selectivity of the Electrocatalytic Hydrogenation of Aldehydes. *ACS Catal.* **8**, 7645–7658 (2018).
62. Li, S., Sun, X., Yao, Z., Zhong, X., Cao, Y., Liang, Y., Wei, Z., Deng, S., Zhuang, G., Li, X., Wang, J. Biomass Valorization via Paired Electrosynthesis Over Vanadium Nitride-Based Electrocatalysts. *Adv. Funct. Mater.* **29**, 1–9 (2019).

63. Roylance, J. J., Kim, T. W., Choi, K. S. Efficient and Selective Electrochemical and Photoelectrochemical Reduction of 5-Hydroxymethylfurfural to 2,5-Bis(hydroxymethyl)furan using Water as the Hydrogen Source. *ACS Catal.* **6**, 1840–1847 (2016).
64. Hu, L., Lin, L., Wu, Z., Zhou, S., Liu, S. Recent advances in catalytic transformation of biomass-derived 5-hydroxymethylfurfural into the innovative fuels and chemicals. *Renew. Sustain. Energy Rev.* **74**, 230–257 (2017).
65. Kwon, Y., De Jong, E., Raoufmoghaddam, S., Koper, M. T. M. Electrocatalytic hydrogenation of 5-hydroxymethylfurfural in the absence and presence of glucose. *ChemSusChem* **6**, 1659–1667 (2013).
66. Kwon, Y., Birdja, Y. Y., Raoufmoghaddam, S., Koper, M. T. M. Electrocatalytic hydrogenation of 5-hydroxymethylfurfural in acidic Solution. *ChemSusChem* **8**, 1745–1751 (2015).
67. Nilges, P., Schröder, U. Electrochemistry for biofuel generation: Production of furans by electrocatalytic hydrogenation of furfurals. *Energy Environ. Sci.* **6**, 2925–2931 (2013).
68. Yu, X., Wen, Y., Yuan, T., Li, G. Effective Production of 2,5-Dimethylfuran from Biomass-derived 5-Hydroxymethylfurfural on ZrO₂-doped Graphite Electrode. *ChemistrySelect* **2**, 1237–1240 (2017).
69. Zhang, Y., Wang, B., Qin, L., Li, Q., Fan, Y. A non-noble bimetallic alloy in the highly selective electrochemical synthesis of the biofuel 2,5-dimethylfuran from 5-hydroxymethylfurfural. *Green Chem.* **21**, 1108–1113 (2019)
70. Roylance, J. J., Choi, K. S. Electrochemical reductive biomass conversion: Direct conversion of 5-hydroxymethylfurfural (HMF) to 2,5-hexanedione (HD): Via reductive ring-opening. *Green Chem.* **18**, 2956–2960 (2016).
71. Zhang, L., Zhang, F., Michel, F. C., Co, A. C. Efficient Electrochemical Hydrogenation of 5-Hydroxymethylfurfural to 2,5-Bis(hydroxymethyl)furan on Ag-Displaced Nanotextured Cu Catalysts. *ChemElectroChem* **6**, 4739–4749 (2019).
72. Urbain, F., Tang, P., Carretero, N. M., Andreu, T., Arbiol, J., Morante, J. R. Tailoring Copper Foam with Silver Dendrite Catalysts for Highly Selective Carbon Dioxide Conversion into Carbon Monoxide. *ACS Appl. Mater. Interfaces* **10**, 43650–43660 (2018).
73. Meng, X. K., Tang, S. C., Vongehr, S. A Review on Diverse Silver Nanostructures. *J. Mater. Sci. Technol.* **26**, 487–522 (2010).
74. López, C. M., Choi, K. S. Electrochemical synthesis of dendritic zinc films composed of systematically varying motif crystal. *Langmuir* **22**, 10625–10629 (2006).
75. Choi, J., Kim, M. J., Ahn, S. H., Choi, I., Jang, J. H., Ham, Y. S., Kim, J. J., Kim, S. K.

- Electrochemical CO₂ reduction to CO on dendritic Ag-Cu electrocatalysts prepared by electrodeposition. *Chem. Eng. J.* **299**, 37–44 (2016).
76. Deng, Y., Handoko, A. D., Du, Y., Xi, S., Yeo, B. S. In Situ Raman Spectroscopy of Copper and Copper Oxide Surfaces during Electrochemical Oxygen Evolution Reaction: Identification of Cu^{III} Oxides as Catalytically Active Species. *ACS Catal.* **6**, 2473–2481 (2016).
 77. Ivanda, M., Waasmaier, D., Endriss, A., Ihringer, J., Kirfel, A., Kiefer, W. Low-temperature anomalies of cuprite observed by raman spectroscopy and X-ray powder diffraction. *J. Raman Spectrosc.* **28**, 487–493 (1997).
 78. Liu, R., Sen, A. Unified synthetic approach to silver nanostructures by galvanic displacement reaction on copper: From nanobelts to nanoshells. *Chem. Mater.* **24**, 48–54 (2012).
 79. Shiratsuchi, R., Aikoh, Y., Nogami, G. Pulsed Electroreduction of CO₂ on Copper Electrodes. *J. Electrochem. Soc.* **140**, 3479–3482 (1993).
 80. Electrical Resistivity of Pure Metals, in CRC Handbook of Chemistry and Physics. <http://hbcponline.com/faces/contents/InteractiveTable.xhtml> (2020).
 81. Jeon, Y., Choe, S., Kim, H. C., Kim, M. J., Kim, J. J. Electrodeposition of Cu-Ag films in ammonia-based electrolyte. *J. Alloys Compd.* **775**, 639–646 (2019).
 82. Montante, G., Paglianti, A. Gas hold-up distribution and mixing time in gas-liquid stirred tanks. *Chem. Eng. J.* **279**, 648–658 (2015).
 83. Velasco-Vélez, J. J., Skorupska, K., Frei, E., Huang, Y. C., Dong, C. L., Su, B. J., Hsu, C. J., Chou, H. Y., Chen, J. M., Strasser, P., Schlögl, R., Knop-Gericke, A., Chuang, C. H. The Electro-Deposition/Dissolution of CuSO₄ Aqueous Electrolyte Investigated by in Situ Soft X-ray Absorption Spectroscopy. *J. Phys. Chem. B* **122**, 780–787 (2018).
 84. Durante, C., Perazzolo, V., Perini, L., Favaro, M., Granozzi, G., Gennaro, A. Electrochemical activation of carbon-halogen bonds: Electrocatalysis at silver/copper nanoparticles. *Appl. Catal. B Environ.* **158–159**, 286–295 (2014).
 85. Campbell, F. W., Compton, R. G. Contrasting underpotential depositions of lead and cadmium on silver macroelectrodes and silver nanoparticle electrode arrays. *Int. J. Electrochem. Sci.* **5**, 407–413 (2010).
 86. Oviedo, O. A., Reinaudi, L., Leiva, E. P. M. The limits of underpotential deposition in the nanoscale. *Electrochem. commun.* **21**, 14–17 (2012).
 87. Orazem, M. E., Tribollet, B. *Electrochemical Impedance Spectroscopy*. (Wiley).
 88. Sacco, A. Electrochemical impedance spectroscopy: Fundamentals and application in dye-sensitized solar cells. *Renew. Sustain. Energy Rev.* **79**, 814–829 (2017).
 89. Hernández, S., Tortello, M., Sacco, A., Quaglio, M., Meyer, T., Bianco, S., Saracco, G., Pirri,

- C. F., Tresso, E. New Transparent Laser-Drilled Fluorine-doped Tin Oxide covered Quartz Electrodes for Photo-Electrochemical Water Splitting. *Electrochim. Acta* **131**, 184–194 (2014).
90. Lopez-Ruiz, J. A., Sanyal, U., Egbert, J., Gutiérrez, O. Y., Holladay, J. Kinetic Investigation of the Sustainable Electrocatalytic Hydrogenation of Benzaldehyde on Pd/C: Effect of Electrolyte Composition and Half-Cell Potentials. *ACS Sustain. Chem. Eng.* **6**, 16073–16085 (2018).
91. De Luna, P., Quintero-Bermudez, R., Dinh, C. T., Ross, M. B., Bushuyev, O. S., Todorović, P., Regier, T., Kelley, S. O., Yang, P., Sargent, E. H. Catalyst electro-redeposition controls morphology and oxidation state for selective carbon dioxide reduction. *Nat. Catal.* **1**, 103–110 (2018).
92. Lee, S., Park, G., Lee, J. Importance of Ag-Cu Biphasic Boundaries for Selective Electrochemical Reduction of CO₂ to Ethanol. *ACS Catal.* **7**, 8594–8604 (2017).
93. Gao, J., Zhang, H., Guo, X., Luo, J., Zakeeruddin, S. M., Ren, D., Grätzel, M. Selective C-C Coupling in Carbon Dioxide Electroreduction via Efficient Spillover of Intermediates As Supported by Operando Raman Spectroscopy. *J. Am. Chem. Soc.* **141**, 18704–18714 (2019).
94. Clark, E. L., Hahn, C., Jaramillo, T. F., Bell, A. T. Electrochemical CO₂ Reduction over Compressively Strained CuAg Surface Alloys with Enhanced Multi-Carbon Oxygenate Selectivity. *J. Am. Chem. Soc.* **139**, 15848–15857 (2017).
95. Hwang, D. W., Lee, S., Seo, M., Chung, T. D. Recent advances in electrochemical non-enzymatic glucose sensors – A review. *Anal. Chim. Acta* **1033**, 1–34 (2018).
96. Yan, Y., Jiang, G. Recent advances in catalytic conversion of cellulose into variable chemicals and bio-fuels. *J. Biobased Mater. Bioenergy* **8**, 553–569 (2014).
97. Kwon, Y., Koper, M. T. M. Electrocatalytic hydrogenation and deoxygenation of glucose on solid metal electrodes. *ChemSusChem* **6**, 455–462 (2013).
98. Vedovato, V., Vanbroekhoven, K., Pant, D., Helsen, J. Electrosynthesis of biobased chemicals using carbohydrates as a feedstock. *Molecules* **25**, 3712 (2020).
99. Bin Kassim, A., Rice, C. L., Kuhn, A. T. Formation of sorbitol by cathodic reduction of glucose. *J. Appl. Electrochem.* **11**, 261–267 (1981).
100. Pal, P., Kumar, R., Banerjee, S. Manufacture of gluconic acid: A review towards process intensification for green production. *Chem. Eng. Process. Process Intensif.* **104**, 160–171 (2016).
101. Mika, L. T., Cséfalvay, E., Németh, Á. Catalytic Conversion of Carbohydrates to Initial Platform Chemicals: Chemistry and Sustainability. *Chem. Rev.* **118**, 505–613 (2018).

102. Boussie, T.R., Dias, E.L., Fresco, Z.M., Murphy, V.J., Shoemaker, J., Archer, R., Jiang, H. US 2014/0275622 A1. (2010).
103. Smith, T. N., Hash, K., Davey, C. L., Mills, H., Williams, H., Kiely, D. E. Modifications in the nitric acid oxidation of d-glucose. *Carbohydr. Res.* **350**, 6–13 (2012).
104. Donen, S., Jensen, K. US 2014/0275622 A1. (2014).
105. Zhang, Z., Huber, G. W. Catalytic oxidation of carbohydrates into organic acids and furan chemicals. *Chem. Soc. Rev.* **47**, 1351–1390 (2018).
106. Saeed, K., Priecel, P., Lopez-Sanchez, J. A. Catalytic routes towards bio-renewable glucaric acid. *Chim. Oggi/Chemistry Today* **35**, 7–11 (2017).
107. Brouzgou, A., Tsiakaras, P. Electrocatalysts for Glucose Electrooxidation Reaction: A Review. *Top. Catal.* **58**, 1311–1327 (2015).
108. Sehit, E., Altintas, Z. Significance of nanomaterials in electrochemical glucose sensors: An updated review (2016-2020). *Biosens. Bioelectron.* **159**, 112165 (2020).
109. Toghill, K. E., Compton, R. G. Electrochemical non-enzymatic glucose sensors: A perspective and an evaluation. *Int. J. Electrochem. Sci.* **5**, 1246–1301 (2010).
110. Torigoe, K., Takahashi, M., Tsuchiya, K., Iwabata, K., Ichihashi, T., Sakaguchi, K., Sugawara, F., Abe, M. High-Power Abiotic Direct Glucose Fuel Cell Using a Gold-Platinum Bimetallic Anode Catalyst. *ACS Omega* **3**, 18323–18333 (2018).
111. de Sá, M. H., Brandão, L. Non-enzymatic direct glucose fuel cells (DGFC): A novel principle towards autonomous electrochemical biosensors. *Int. J. Hydrogen Energy* **45**, 29749–29762 (2020).
112. Santiago, Ó., Navarro, E., Raso, M. A., Leo, T. J. Review of implantable and external abiotically catalysed glucose fuel cells and the differences between their membranes and catalysts. *Appl. Energy* **179**, 497–522 (2016).
113. Chen, J., Zheng, H., Kang, J., Yang, F., Cao, Y., Xiang, M. An alkaline direct oxidation glucose fuel cell using three-dimensional structural Au/Ni-foam as catalytic electrodes. *RSC Adv.* **7**, 3035–3042 (2017).
114. Abbadì, A., Makkee, M., van Bekkum, H., Visscher, W., van Veen, J. A. R. Effect of pH in the Pd-catalyzed oxidation of d-glucose to d-gluconic acid. *J. Carbohydr. Chem.* **12**, 573–587 (1993).
115. Vassilyev, Y. B., Khazova, O. A., Nikolaeva, N. N. Kinetics and mechanism of glucose electrooxidation on different electrode-catalysts. Part I. Adsorption and oxidation on platinum. *J. Electroanal. Chem.* **196**, 105–125 (1985).
116. Bamford, C. H., Collins, J. R. Kinetic Studies on Carbohydrates in Alkaline Conditions. III.

- Interconversion of D-Glucose, D-Fructose and D-Mannose in Feebly Alkaline Solution. *Proc. R. Soc. Lond. A. Math. Phys. Sci.* **228**, 100–119 (1955).
117. Knill, C. J., Kennedy, J. F. Degradation of cellulose under alkaline conditions. *Carbohydr. Polym.* **51**, 281–300 (2002).
 118. Corbett, W. M., Liddle, A. M. The alkaline degradation of glucose and of some of its acetyl derivatives. *J. Chem. Soc.* 531–538 (1961).
 119. Yun Yang, B., Montgomery, R. Alkaline degradation of glucose: Effect of initial concentration of reactants. *Carbohydr. Res.* **280**, 27–45 (1996).
 120. Ibert, M., Fuerts, P., Merbouh, N., Feasson, C., Marsais, F. Evidence of benzilic rearrangement during the electrochemical oxidation of D-glucose to D-glucaric acid. *Carbohydr. Res.* **346**, 512–518 (2011).
 121. Kokoh, K. B., Leger, J. M., Beden, B., Huser, H., Lamy, C. ‘On line’ chromatographic analysis of the products resulting from the electrocatalytic oxidation of D-glucose on pure and adatoms modified Pt and Au electrodes - Par II Alkaline medium. *Electrochim. Acta* **37**, 1909–1918 (1992).
 122. Ibert, M., Fuertès, P., Merbouh, N., Fiol-Petit, C., Feasson, C., Marsais, F. Improved preparative electrochemical oxidation of d-glucose to d-glucaric acid. *Electrochim. Acta* **55**, 3589–3594 (2010).
 123. Gao, M., Sheng, W., Zhuang, Z., Fang, Q., Gu, S., Jiang, J., Yan, Y. Efficient water oxidation using nanostructured α -nickel-hydroxide as an electrocatalyst. *J. Am. Chem. Soc.* **136**, 7077–7084 (2014).
 124. Bott-Neto, J. L., Martins, T. S., Machado, S. A. S., Ticianelli, E. A. Electrocatalytic Oxidation of Methanol, Ethanol, and Glycerol on Ni(OH)₂ Nanoparticles Encapsulated with Poly[Ni(salen)] Film. *ACS Appl. Mater. Interfaces* **11**, 30810–30818 (2019).
 125. Almomani, F., Bhosale, R., Khraisheh, M., Kumar, A., Tawalbeh, M. Electrochemical oxidation of ammonia on nickel oxide nanoparticles. *Int. J. Hydrogen Energy* **45**, 10398–10408 (2020).
 126. Coutanceau, C., Baranton, S., Kouamé, R. S. B. Selective electrooxidation of glycerol into value-added chemicals: A short overview. *Front. Chem.* **7**, 1–15 (2019).
 127. Houache, M. S. E., Hughes, K., Baranova, E. A. Study on catalyst selection for electrochemical valorization of glycerol. *Sustain. Energy Fuels* **3**, 1892–1915 (2019).
 128. Habibi, B., Delnavaz, N. Electrooxidation of glycerol on nickel and nickel alloy (Ni-Cu and Ni-Co) nanoparticles in alkaline media. *RSC Adv.* **6**, 31797–31806 (2016).
 129. Van Drunen, J., Napporn, T. W., Kokoh, B., Jerkiewicz, G. Electrochemical oxidation of

- isopropanol using a nickel foam electrode. *J. Electroanal. Chem.* **716**, 120–128 (2014).
130. Bidault, F., Brett, D. J. L., Middleton, P. H., Abson, N., Brandon, N. P. A new application for nickel foam in alkaline fuel cells. *Int. J. Hydrogen Energy* **34**, 6799–6808 (2009).
131. Zhao, L., Kuang, X., Sun, X., Zhang, Y., Wei, Q. Synchronously Achieving Highly Efficient Hydrogen Evolution and High-Yield Synthesis of Glucaric Acid by MOF Nanorod Arrays. *J. Electrochem. Soc.* **166**, H534–H540 (2019).
132. Kowal, A., Port, S. N., Nichols, R. J. Nickel hydroxide electrocatalysts for alcohol oxidation reactions: An evaluation by infrared spectroscopy and electrochemical methods. *Catal. Today* **38**, 483–492 (1997).
133. Miao, Y., Ouyang, L., Zhou, S., Xu, L., Yang, Z., Xiao, M., Ouyang, R. Electrocatalysis and electroanalysis of nickel, its oxides, hydroxides and oxyhydroxides toward small molecules. *Biosens. Bioelectron.* **53**, 428–439 (2014).
134. Toghill, K. E., Xiao, L., Stradiotto, N. R., Compton, R. G. The determination of methanol using an electrolytically fabricated nickel microparticle modified boron doped diamond electrode. *Electroanalysis* **22**, 491–500 (2010).
135. Jung, H. J., Choi, M. Y. Specific solvent produces specific phase Ni nanoparticles: A pulsed laser ablation in solvents. *J. Phys. Chem. C* **118**, 14647–14654 (2014).
136. Ravikumar, P., Kisan, B., Perumal, A. Enhanced room temperature ferromagnetism in antiferromagnetic NiO nanoparticles. *AIP Adv.* **5**, (2015).
137. George, G., Anandhan, S. Synthesis and characterisation of nickel oxide nanofibre webs with alcohol sensing characteristics. *RSC Adv.* **4**, 62009–62020 (2014).
138. Hall, D. S., Lockwood, D. J., Bock, C., MacDougall, B. R. Nickel hydroxides and related materials: A review of their structures, synthesis and properties. *Proc. R. Soc. A Math. Phys. Eng. Sci.* **471**, (2015).
139. Johnston, C., Graves, P. R. In situ Raman spectroscopy study of the nickel oxyhydroxide electrode (NOE) system. *Appl. Spectrosc.* **44**, 105–115 (1990).
140. Ho, P. H., Scavetta, E., Ospitali, F., Tonelli, D., Fornasari, G., Vaccari, A., Benito, P. Effect of metal nitrate concentration on the electrodeposition of hydrotalcite-like compounds on open-cell foams. *Appl. Clay Sci.* **151**, 109–117 (2018).
141. Jin, X., Zhao, M., Vora, M., Shen, J., Zeng, C., Yan, W., Thapa, P. S., Subramaniam, B., Chaudhari, R. V. Synergistic Effects of Bimetallic PtPd/TiO₂ Nanocatalysts in Oxidation of Glucose to Glucaric Acid: Structure Dependent Activity and Selectivity. *Ind. Eng. Chem. Res.* **55**, 2932–2945 (2016).
142. Diaz-Morales, O., Ferrus-Suspedra, D., Koper, M. T. M. The importance of nickel

oxyhydroxide deprotonation on its activity towards electrochemical water oxidation. *Chem. Sci.* **7**, 2639–2645 (2016).

143. Godwin, I. J., Lyons, M. E. G. Enhanced oxygen evolution at hydrous nickel oxide electrodes via electrochemical ageing in alkaline solution. *Electrochem. commun.* **32**, 39–42 (2013).